Studies of TGS/P(VDF-TrFE) and MMT/P(VDF-TrFE) 0-3 Composites

Submitted by

Yang Yan

A thesis submitted in partial fulfilment of the requirements for
the Degree of Master of Philosophy in Applied Physics

At

Department of Applied Physics
The Hong Kong Polytechnic University

October 2004

Certificate of Originality

I hereby declare that this thesis is my own work and that, to the best of my knowledge and belief, it reproduces no material previously published or written nor material which has been accepted for the award of any other degree or diploma, expect where due acknowledgement has been made in the text.

____________________ (Signed)

YANG YAN (Name of Student)

Abstract

Ferroelectric ceramic/polymer composites have been widely studied in recent years due to the combination of good mechanical performance and high electroactive capabilities. In this project, triglycine sulfate (TGS)/poly(vinylidene fluoride-trifluoroethylene) (P(VDF-TrFE), 70/30 mol%) 0-3 composites with various volume percents of TGS were fabricated by compression moulding. Three series of composites were prepared: (I) unpoled composites, (II) composites with only the TGS phase poled and (III) composites with both phases poled. The structure, phase transitions and dielectric, piezoelectric and pyroelectric properties of the composites were investigated.

Scanning electron microscope (SEM) studies of the composites showed that the TGS particles were uniformly dispersed in the copolymer matrix. The reflection peaks of both the TGS and P(VDF-TrFE) phase appeared in the X-ray diffraction (XRD) patterns of the composites and the phase transitions of the two phases were observed in the differential scanning calorimetry (DSC) thermograms of the composites. The relative permittivity and pyroelectric coefficient of the composites were found to increase with increasing TGS content. The relative permittivity and pyroelectric coefficient were compared with the theoretical predictions of the Bruggeman model and the effective medium model, respectively, and good agreement was obtained. It was also found that if the two phases were poled in the same direction, the pyroelectric contributions from TGS and P(VDF-TrFE) reinforced while piezoelectric contributions partially canceled. Thus the composite with 43 vol% of TGS exhibited a high pyroelectric coefficient and high pyroelectric figures of merit together with a low piezoelectric coefficient. The low piezoelectric activity is a significant advantage in pyroelectric sensor application since it will give rise to a low vibration induced noise.

Montmorillonite (MMT)/P(VDF-TrFE) (80/20 mol%) 0-3 nanocomposites with 1 wt% and 4 wt% of MMT were also fabricated. Na^+-MMT was first modified with cetyltrimethylammonium bromide (CTAB) before being incorporated into the copolymer matrix. The nanocomposites were characterized by means of XRD and DSC. The dielectric permittivity, polarization hysteresis, piezoelectric coefficient and pyroelectric coefficient were also measured. The XRD patterns showed that P(VDF-TrFE) copolymer chains had been intercalated into the layered nanostructures of the CTAB treated MMT. The DSC thermograms indicated that the Curie temperature of the nanocomposites were higher than that of the pure copolymer. The relative permittivity and remnant polarization of the nanocomposites were found to increase with MMT content. The piezoelectric coefficient and pyroelectric coefficient were also enhanced in the MMT/P(VDF-TrFE) nanocomposites.

Publications

Y. Yang, H. L. W. Chan and C. L. Choy, "Properties of intercalated montmorillonite /poly(vinylidene fluoride-trifluoroethylene) nanocomposites", Integrated Ferroelectrics, to be published (2004).

Y. Yang, H. L. W. Chan and C. L. Choy, "Properties of triglycine sulfate/poly (vinylidene fluoride-trifluoroethylene) 0-3 composites" Journal of Materials Science, Submitted (2004).

Acknowledgements

I would like to express my gratitude to my chief supervisor Prof. C. L. Choy for his guidance and valuable comments on my work and my co-supervisor Prof. H. L. W. Chan for her guidance, continuous support and encouragement in the whole period of my study. Their rich experience and valuable suggestions have helped me overcome many difficulties in my study.

I would like to thank Dr. J. Wang for his useful comments and help on the use of experimental techniques and Mr. M. N. Yeung of the Materials Research Centre for his kind assistance.

I give my appreciation for the help from the colleagues in our group, namely Mr. S. S. Guo, Ms. S. T. Lau, Mr. D. Y. Wang, Ms. M. K. Cheung and Mr. S. H. Choy. I also greatly appreciate the heartfelt support from my roommates, namely Ms. K. Y. Chan, Ms. C. Y. Lam and Ms. H. K. Lam.

Financial support from the Hong Kong Polytechnic University and the Hong Kong Research Grants Council are gratefully acknowledged.

Table of Contents

Chapter 1 *Introduction*

Chapter 2 Preparation of TGS/P(VDF-TrFE) 0-3 Composites

Chapter 3 Structures and Phase Transitions of TGS/P(VDF-TrFE) 0-3 Composites

Chapter 4 Dielectric, Piezoelectric and Pyroelectric Properties of TGS/P(VDF-TrFE) 0-3 Composites

Chapter 5 Studies of MMT/P(VDF-TrFE) 0-3 Nanocomposites

Chapter 6 Conclusions and Suggestions for Future Work

List of Figures

List of Tables

Chapter 1 Introduction

1.1 Ferroelectric Ceramic/Polymer 0-3 Composites

Ferroelectric ceramic/polymer composites consisting of a ceramic filler and a polymer matrix have been widely investigated in recent years. These materials combine the advantages of polymers, e.g. mechanical flexibility, good formability and low cost, with the advantages of ceramics, e.g. high electroactive properties, and have become potential candidates in many applications including electromechanical transducers, microphones, hydrophones and pyroelectric sensors. [Mazur, 1995]

Conventional ferroelectric ceramic materials such as barium titanate and lead zirconate titanate (PZT) have good piezoelectric and pyroelectric properties. In addition, these materials exhibit high electromechanical coupling (k_t~0.4-0.5), a wide range of relative permittivity (ε_r'~100-2400) and low dielectric loss. However, their brittle nature and inflexibility limit their use in some applications. Ferroelectric polymers such as poly(vinylidene fluoride), PVDF, and vinylidene trifluoroethylene copolymers, P(VDF-TrFE), have good mechanical properties and low relative permittivity. Therefore, a ceramic/polymer composite is considered as an alternative material exhibiting high electroactive properties and good mechanical properties. [Dias et al., 1994]

1.1.1 Connectivities

The properties of composites depend not only on the properties of individual phases but also on the way they are interconnected and the process of fabrication. The concept of connectivity was first proposed by Newham (1978) to describe the interfacial spatial relationship in multiphase materials. According to his idea, each phase in a composite may be self-connected in zero, one, two or three dimensions. In the case of diphasic composites, there are 10 connectivities, designated as 0-0, 0-1, 0-2, 0-3, 1-1, 1-2, 1-3, 2-2, 2-3 and 3-3 (the first number denotes the connectivity of the filler and the second one denotes the connectivity of the matrix). Figure 1.1 describes the connectivities using a cube as the basic building block. As an example, the commonly used composite of dispersed particles embedded in a matrix should be denoted as a 0-3 composite.

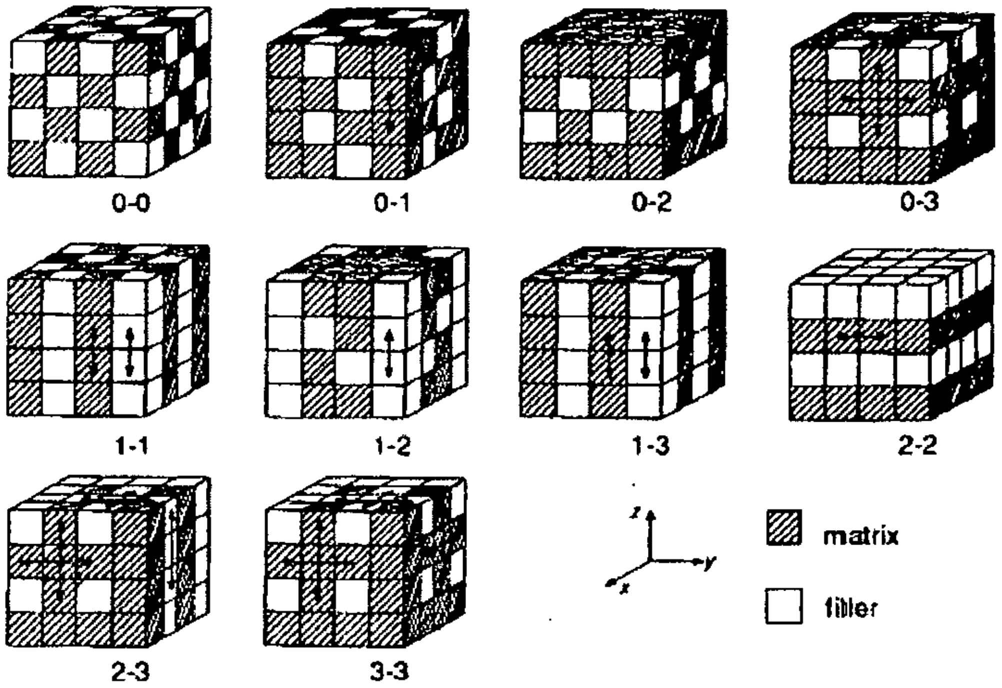

Figure 1.1 Connectivity patterns in a diphasic composite system. [Newnham, 1978]

The connectivity of the phases is a very important parameter because it controls the mechanical, electrical and thermal fluxes between the phases. This finding prompted research on composites consisting of embedding rods of a piezoelectric material in a polymer host to form a 1-3 network [Savakus et al., 1980] which should exhibit better properties than the simple powder dispersed composites. Other ceramic-polymer configurations have been investigated such as using ceramic fibres and coral ceramic templates to make a self connected 3-3 composite [Skinner et al., 1978]. Nevertheless, the 0-3 composite is still the most popular configuration because the composite can be fabricated into various forms in a relatively simple way and the low cost makes it possible for mass production.

1.1.2 Mixing Rules for Permittivity

The dielectric properties of composites have been modelled through the so-called mixing rules. As shown in Figure 1.2, in the simplest case, the permittivity can be calculated from a capacitor model consisting of two different dielectrics connected in

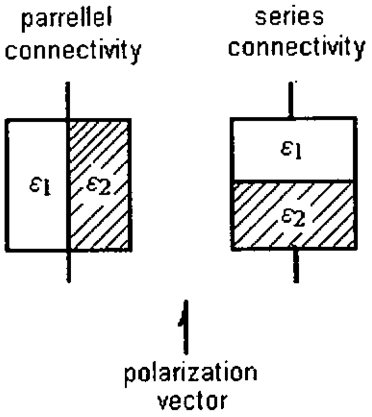

Figure 1.2 Parallel and series connectivities. [Newnham, 1978]

parallel (corresponding to the 1-3 connectivity) or in series (corresponding to the 2-2 connectivity). The permittivity ε of the composite consisting of two phases with permittivities ε_1 and ε_2 is given by [Newnham et al., 1978]:

$$\varepsilon = \phi \cdot \varepsilon_1 + (1-\phi) \cdot \varepsilon_2 \quad \text{(in parallel)} \tag{1.1}$$

$$\frac{1}{\varepsilon} = \frac{\phi}{\varepsilon_1} + \frac{1-\phi}{\varepsilon_2} \quad \text{(in series)} \tag{1.2}$$

where ϕ is the volume fraction of phase 1. In the case of 0-3 composites, the calculation becomes much more complicated. However, a number of formulae have been suggested for the calculation of the permittivity of 0-3 composites. These formulae have been derived on the basis of various assumptions. Table 1.1 shows the most popular mixing rules which have been used to describe the permittivity of 0-3 systems. The subscript *i* and *m* represent the properties of the inclusion and the matrix, respectively.

Table 1.1 Formulae of mixing rules for the permittivity of diphasic 0-3 composites.

Mixing Rule	*Formula*	*Reference*
Maxwell-Wagner	$\varepsilon = \varepsilon_m \cdot \frac{2\varepsilon_m + \varepsilon_i + 2\phi(\varepsilon_i - \varepsilon_m)}{2\varepsilon_m + \varepsilon_i - \phi(\varepsilon_i - \varepsilon_m)}$	(Wagner, 1914)
Bruggeman	$\left(\frac{\varepsilon_m}{\varepsilon}\right)^{1/3} = (1-\phi) \cdot \frac{\varepsilon_i - \varepsilon_m}{\varepsilon_i - \varepsilon}$	(Bruggeman, 1935)
Lichtenecker	$\log \varepsilon = \phi \cdot \log \varepsilon_i + (1-\phi) \cdot \log \varepsilon_m$	(Hippel, 1959)
Yamada	$\varepsilon = \varepsilon_m \cdot \left(1 + \frac{n\phi(\varepsilon_i - \varepsilon_m)}{n\varepsilon_m + (1-\phi)(\varepsilon_i - \varepsilon_m)}\right)$ n is the shape parameter of particles	(Yamada et al., 1982)

1.1.3 Fabrication of Ferroelectric 0-3 Composites

Before the preparation of 0-3 composites, the ceramic has to be transformed into powder form from its usual block shape after the pressing, firing and sintering stages. The powder form can be achieved either by the conventional method where the ceramic is mechanically ground until the desired dimension is obtained or by heating the ceramic block and then quenching it in a water bath kept at room temperature, fracturing the ceramic along the cleavage planes arising from the thermal stresses. It is clear that the grinding method provides a better control of the size of the ceramic grains than the quenching process where a wider distribution of grain sizes is obtained. The powder may need to be further sieved to separate the grains into a narrow size range. A more recent approach for producing ceramic powder is to use a sol-gel method where a fine grain size is obtained through the direct calcination of the gel powder [Xu et al., 1992].

The polymer to be used determines the way in which the materials will be mixed. If it is a thermoset polymer e.g. an epoxy, the blending process can be performed in a simple way where the right proportions of the resin, hardener and ceramic powder are mixed together by hand at room temperature. In the case of a thermoplastic polymer the blending process can be done in two ways. In the first method the polymer is first heated in a hot rolling machine to a temperature between its softening and melting temperature, then the ceramic powder is gradually added until a desired blend is obtained. In the second method the polymer is dissolved in a suitable solvent and then the ceramic powder is added into the solution. This solution is then deposited onto a plate and the solvent is allowed to evaporate at a suitable temperature. The composite thus obtained sometimes needs further processing in order to obtain the desired thickness. This is achieved by hot pressing above the softening temperature of the polymer or by means of polishing and grinding operations.

1.2 Pyroelectric Applications of Ferroelectric 0-3 Composites

The main aim of this project is to fabricate ferroelectric 0-3 composites with high pyroelectric activity and high pyroelectric figures of merit. Hence the pyroelectric properties of ferroelectric ceramic/polymer 0-3 composites that have been studied will be reviewed in this section.

1.2.1 Pyroelectric Materials

The pyroelectric effect refers to the phenomenon in which the degree of polarization changes with the variation of temperature. The magnitude of pyroelectric effect is characterized by the pyroelectric coefficient p which is defined as:

$$p = \frac{\partial P}{\partial T} \tag{1.3}$$

In practical applications, to optimize the efficiency of a pyroelectric sensor, the heat capacity per unit volume $C_p^{vol.}$, relative permittivity ε, dielectric loss $tan\delta$ and pyroelectric coefficient p must be also considered. Then the pyroelectric figures of merit F_i (for high current responsivity), F_V (for high voltage responsivity) and F_D (for high detectivity) are given as:

$$F_i = \frac{p}{C_p^{vol.}}; \quad F_V = \frac{p}{C_p^{vol.}\varepsilon\varepsilon_o}; \quad F_D = \frac{p}{C_p^{vol.}(\varepsilon\varepsilon_o \tan\delta)^{1/2}} \tag{1.4}$$

In addition, $F_p = p/\varepsilon$ is also a commonly used figure of merit. To date, several materials have been developed and used as the pyroelectric sensing elements in infrared detectors. Their properties are shown in Table 1.2.

Table 1.2 Properties of some pyroelectric materials. [Moulson et al., 2003]

Material and form	*-p* $\mu C/m^2K$	ε	*tanδ*	$C_p^{vol.}$ MJ/m^3K	F_P $\mu C/m^2K$	F_i $10^{-12}m/V$	F_V m^2/C	F_D $10^{-6}Pa^{-1/2}$
TGS (single crystal);	280	38	0.01	2.3	7.4	122	0.36	66
$LiTaO_3$ (single crystal)	230	47	0.001	3.2	4.9	72	0.17	110
$(SrBa)Nb_2O_6$ (single crystal)	550	400	0.001	2.3	1.4	239	0.07	70
Modified $PbTiO_3$ (polycrystalline)	350	220	0.01	2.5	1.6	140	0.07	32
$P(25Zr,75Ti)O_3$ (sol-gel film)	220	350	0.008	2.7	0.6	81	0.03	17
P(70VDF-30TrFE)(film)	33	7.4	0.017	2.3	4.5	14	0.22	13.6

The usefulness of a material for pyroelectric sensor applications does not necessarily depend on its figures of merit alone. Other properties such as mechanical strength, chemical stability, matching to amplifiers etc. may be important considerations. For example, TGS crystals have high pyroelectric activity, but are fragile and water-soluble. Ferroelectric ceramic/polymer 0-3 composites with good mechanical properties and high pyroelectric activity may be good candidates to replace conventional materials.

1.2.2 Pyroelectric 0-3 Composites

Various pyroelectric 0-3 composites have been studied. These composites can be divided into two groups: composites with only the inclusion phase pyroelectrically active and composites with two phases pyroelectrically active. The commonly used non-pyroelectric matrices include epoxy [Bhalla et al., 1981], rubber [Amin et al., 1988], poly(methyl methacrylate) (PMMA) [Mazur, 1994] and PVDF [Yamada et al., 1982; Yamazaki et al., 1981]. It was well known that PVDF in a polar phase (the β phase) can possess pyroelectric properties, but it needs to be mechanically stretched prior to poling to give pyroelectric activity. Thus in 0-3 composites PVDF serves only as a non-pyroelectric matrix with relatively high permittivity to facilitate poling.

Until now, the only pyroelectrically active matrix used is P(VDF-TrFE) with TrFE content >20 mol%. Chan's research group has studied a series of ceramic/P(VDF-TrFE) 0-3 composites [Chan et al., 1998;1999]. It should be noted that the composites must be poled at an electric field higher than the coercive field of P(VDF-TrFE) (~50V/μm) to elicit the pyroelectric activity in the copolymers.

On the other hand, the commonly used ceramic materials include the conventional pyroelectric materials e.g. $PbTiO_3$ [Yamazaki et al., 1981; Dias et al., 1992], PZT [Mazur, 1994; Dias et al., 1993], and $PbTiO_3$ and PZT modified with Ca [Zhang et al., 1999; Dias et al., 1996] and La [Varaprasad et al., 1987]. Triglycine sulfate (TGS) has also been used in pyroelectric 0-3 composites and the related work will be described in the next section. Table 1.3 summarizes the pyroelectric properties of some typical pyroelectric 0-3 composites.

Table 1.3 Pyroelectric properties of some 0-3 composites.

0-3 composite (volume fraction of ceramic)	p $\mu C/m^2K$	ε	p/ε $\mu C/m^2K$	*Reference*
PZT/Epoxy (0.4)	40	114	0.35	Bhalla et al., 1981
PTCa/PVDF (0.5)	50	56	0.90	Dias et al., 1993
$PbTiO_3$*/PVDF (0.42)*	45.9	27	1.70	Yamazaki et al., 1981
$PbTiO_3$*/P(VDF-TrFE) (0.39)*	53.4	29.5	1.81	Chan et al., 1998

It should be noted that, for ferroelectric ceramic/P(VDF-TrFE) composites, the pyroelectric coefficient of the ceramic and copolymer phases have like signs while the piezoelectric coefficients have opposite signs. Therefore, when the two phases are poled in the same direction, the pyroelectric contributions from the two phases reinforce while piezoelectric contributions partially cancel each other. The low piezoelectric activity will lead to a reduction of the vibration-induced electrical noise.

1.2.3 TGS/Polymer 0-3 Composites

Studies on the pyroelectric properties of TGS/PVDF 0-3 composites have been reported. In the work of Fang et al. [1991], TGS crystals particles of size 45 to 75 μm were mixed with PVDF which had previously been dissolved in an organic solvent and then the composite solution was poured onto a glass plate to obtain 50~100 μm thick films. Poling was performed at 70~80 °C for 2~3h at a field of 0.4~0.6 MV/m. The results shown in Figure 1.3 indicated that the pyroelectric coefficient and figure of merit increased with increasing TGS content. Wang et al. [1993] have also studied TGS/PVDF composites with various vol% of TGS. The pyroelectric properties increased with TGS content and at 80 vol% of TGS the pyroelectric coefficient obtained was ~90 $\mu C/m^2K$ (as shown in Figure 1.4). Petty et al. [1993] have reported the pyroelectric properties of a TGS/P(VDF-TrFE) composite with 10 wt% TGS powder (size ~5 μm). The material possessed a pyroelectric coefficient of 60 $\mu C/m^2K$ and a figure of merit $(p/(\varepsilon tan\delta)^{1/2})$ of 150 $\mu C/m^2K$.

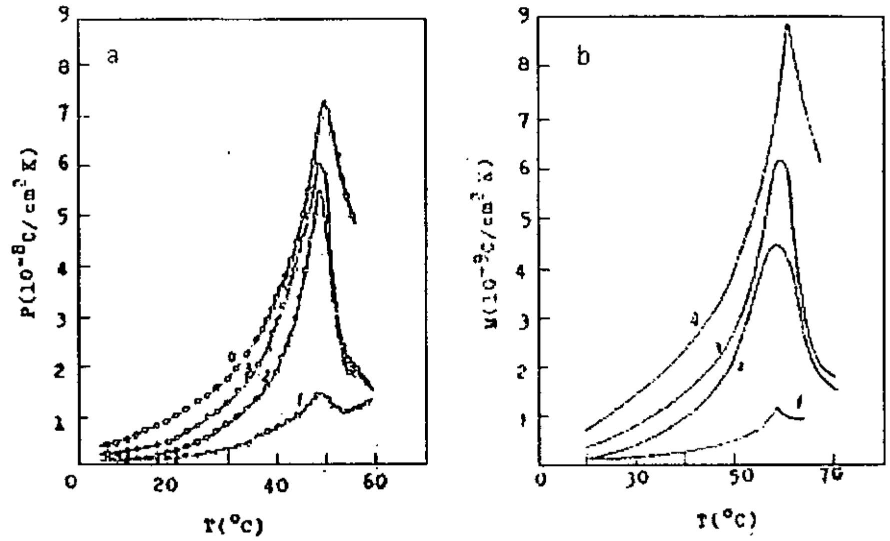

Figure 1.3 Pyroelectric coefficient p (a) and figure of merit p/ε (b) as a function of temperature for TGS/PVDF composites. W_{PVDF}/W_{TGS}: 2/1 (curve 1), 1/2 (curve 2), 1/4 (curve 3), 1/1 (curve 4). W is the weight%. [Fang et al., 1991]

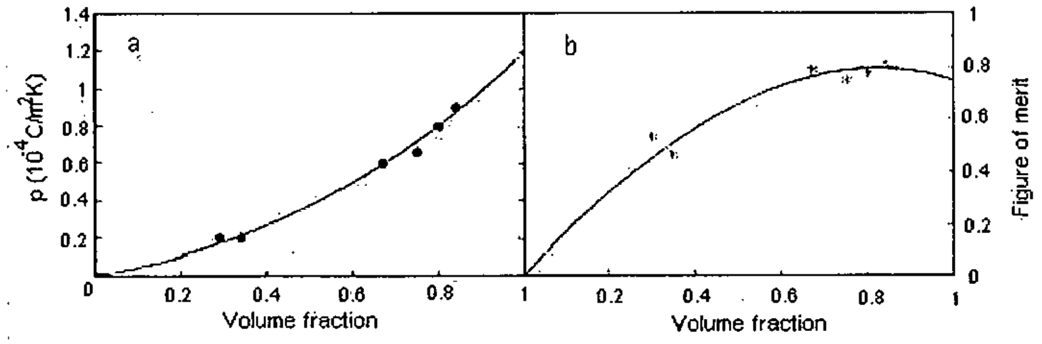

Figure 1.4 Pyroelectric coefficient p (a) and figure of merit p/ε (b) as a function of TGS volume fraction for TGS/PVDF composites. [Wang et al., 1993]

1.3 Ferroelectric Polymers: PVDF and P(VDF-TrFE)

As mentioned in the last section, of all the polymers which have been used as the matrix of ceramic/polymer 0-3 composites, only P(VDF-TrFE) exhibits pyroelectric activity. Therefore, in order to obtain high pyroelectric activity in a 0-3 composites, P(VDF-TrFE) is a good choice as the matrix. The structure and properties of P(VDF-TrFE) copolymer will be introduced in this section.

1.3.1 Structures of PVDF and P(VDF-TrFE) Copolymers

Poly(vinylidene fluoride) (PVDF), discovered by Kawai [1969] to be piezoelectric, is a well-known semicrystalline polymer with approximately equal proportions of random stacks of amorphous and crystalline lamellae [Murayama et al., 1976]. A PVDF molecule consists of a repeated monomer unit (CH_2CF_2) which exhibits a dipole moment due to the positive hydrogen and negative fluorine atoms. The crystal structure of PVDF is dependent on the molecular conformation and packing mode. Four types of crystal structures designated as forms α, β, γ and δ (or forms I, II, III and IV) were found and are shown in Figure 1.5, where T and G denote the *trans* planar isomer and gauche non-planar isomer, respectively. Melt-crystallization of PVDF produces the most stable structure: nonpolar α phase which consists of TGTG' molecules packed in an antiparallel mode. α-PVDF can be converted into other phases, for example, the polar β-PVDF (with all-*trans* conformation) which can be induced by mechanical stretching. β-PVDF was found to exhibit ferroelectric behavior.

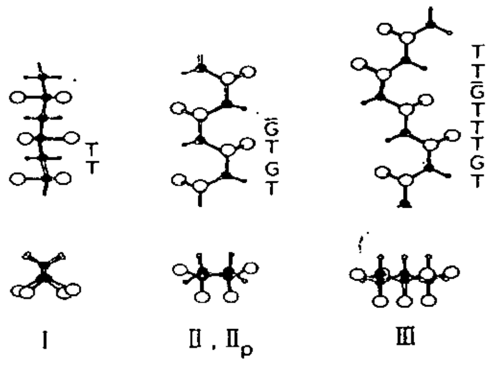

Figure 1.5 Molecular structures in PVDF. [Tashiro et al., 1981]

Lando et al. [1968] reported in their early work that the introduction of 93 mol% TrFE in PVDF can induce direct crystallization with a somewhat expanded β cell. Later on, Yagi et al. [1980] synthesized P(VDF-TrFE) copolymers over the entire range of compositions. Because of similarity in the size of hydrogen and fluorine atoms, VDF and TrFE units are randomly distributed along the molecular chain to form a random copolymer and cocrystallized into a single crystalline phase analogous to β-PVDF. A ferroelectric to paraelectric phase transition exists in copolymers containing 50-85 mol% VDF. The structural and electrical behaviors of these copolymers are strongly influenced by the mol% of VDF.

1.3.2 Properties of P(VDF-TrFE) Copolymers

The physical properties of P(VDF-TrFE) copolymers, e.g. permittivity, polarization reversal, piezoelectric and pyroelectric properties, have been extensively studied in the past 25 years. The relative permittivity of copolymers with 13-82 mol% VDF has been reported by Higashihata et al. [1981]. As shown in Figure 1.6, the copolymers exhibit a peak in a temperature range between 60 and 150 °C, which is considered to be the manifestation of a ferroelectric phase transition (Curie point). The peak shifts to higher temperature with increasing VDF content.

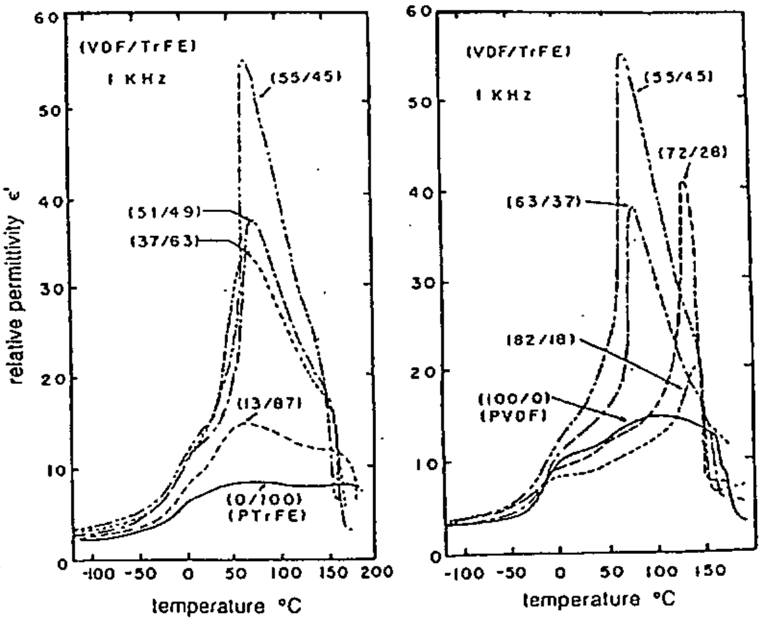

(a) (b)

Figure 1.6 Relative permittivity for P(VDF-TrFE) copolymers in the composition ranges of (a) 0-55 mol% VDF and (b) 55-100 mol% VDF as a function of temperature. [Higashihata et al., 1981]

The polarization reversal in ferroelectric P(VDF-TrFE) copolymers can be demonstrated by the appearance of hysteresis loops. Figure 1.7 shows the hysteresis loops of the copolymer with 65 mol% VDF under different amplitudes of electric field and a well-defined loop appears when the amplitude exceeds 55 MV/m. Because of the semicrystalline nature of the copolymer, the values of coercive field E_c and remanent polarization P_r are particularly sensitive to the crystallinity. Tajitsu et al. [1987] found that annealing the copolymer sample between the Curie and melting point may induce dramatic increase in crystallinity. For copolymers containing 60-80 mol% VDF, the crystallinity may go up to 80%, resulting in high values of E_c (55-60 MV/m) and P_r (70-90 mC/m^2). To elicit pyroelectric properties, the copolymer should be poled under a field several times higher than E_c, which is sometimes difficult to achieve without an electrical breakdown due to the relative high E_c of P(VDF-TrFE) copolymers.

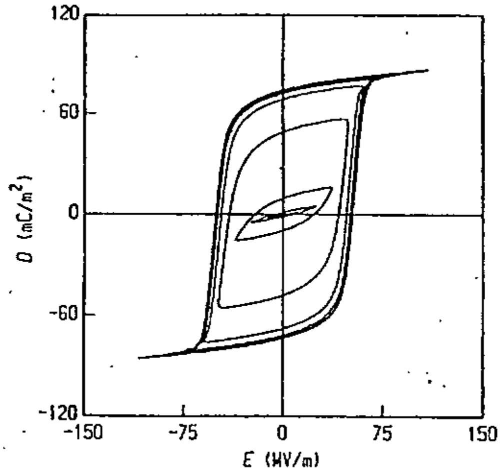

Figure 1.7 Hysteresis loops for P(VDF-TrFE) copolymer with 65 mol% VDF at 20 °C and 10 Hz. [Furukawa, 1989]

The pyroelectric properties of a polarized P(VDF-TrFE) film is shown in Table 1.2, and it can be seen that the pyroelectric coefficient of P(VDF-TrFE) is somewhat smaller than that of some other pyroelectric materials used in the pyroelectric infrared detectors. However, P(VDF-TrFE) copolymers have additional advantages as pyroelectric devices, such as easy formation of large area thin film, low thermal diffusion, flexible configuration and low cost.

1.4 Motivation and Objectives of Research

Various ceramic/polymer 0-3 composites have been prepared with the purpose of maximizing the piezoelectric and pyroelectric properties. In this project, the main aim is to produce 0-3 composites with high pyroelectric activity and high pyroelectric figures of merit. Based on the above discussion, the composite with two phases pyroelectricly active may be a good choice to obtain high pyroelectric activity, and P(VDF-TrFE) copolymer is hence employed as the matrix phase. On the other hand, two kinds of materials are selected as the inclusion phase and the related considerations are given below.

Based on the model proposed by Chew et al. [2003], the pyroelectric coefficient p of a 0-3 composite is given by:

$$p = \left(\frac{\varepsilon - \varepsilon_m}{\varepsilon_i - \varepsilon_m} \right) \cdot p_i + \left(\frac{\varepsilon_i - \varepsilon}{\varepsilon_i - \varepsilon_m} \right) \cdot p_m \tag{1.5}$$

where ε, ε_i and ε_m are the relative permittivities of the composite, inclusion and matrix, respectively and p_i and p_m are the pyroelectric coefficients of the inclusion and matrix, respectively. If we use the Maxwell-Wagner mixing rule (as shown in Table 1.1) to calculate the relative permittivity of the composite ε, the pyroelectric coefficient can be rewritten as:

$$p = \phi \cdot \left(\frac{3\varepsilon_m}{(\varepsilon_i + 2\varepsilon_m) - \phi(\varepsilon_i - \varepsilon_m)} \right) \cdot p_i + (1 - \phi) \cdot \left(\frac{\varepsilon_i + 2\varepsilon_m}{(\varepsilon_i + 2\varepsilon_m) - \phi(\varepsilon_i - \varepsilon_m)} \right) \cdot p_m \tag{1.6}$$

It can be seen that the pyroelectric coefficient of the composite is also related with the relative permittivity of the individual phases. Using this equation, we find the relationship between the pyroelectric coefficient of the composite p and the relative permittivity of the inclusion ε_i. As shown in Figure 1.8 (where the relative permittivity of the matrix ε_m, the pyroelectric coefficient of the inclusion p_i and the matrix p_m, and the volume fraction of the inclusion ϕ are assumed to be 10, 300 μC/m^{2}K and 30 μC/m^{2}K, and 0.3, respectively), when the relative permittivity of the inclusion varies from 15 to 2000, p of the composite decreases dramatically. It can be concluded that high relative permittivity of the inclusion will inhibit the improvement of pyroelectric properties in 0-3 composites.

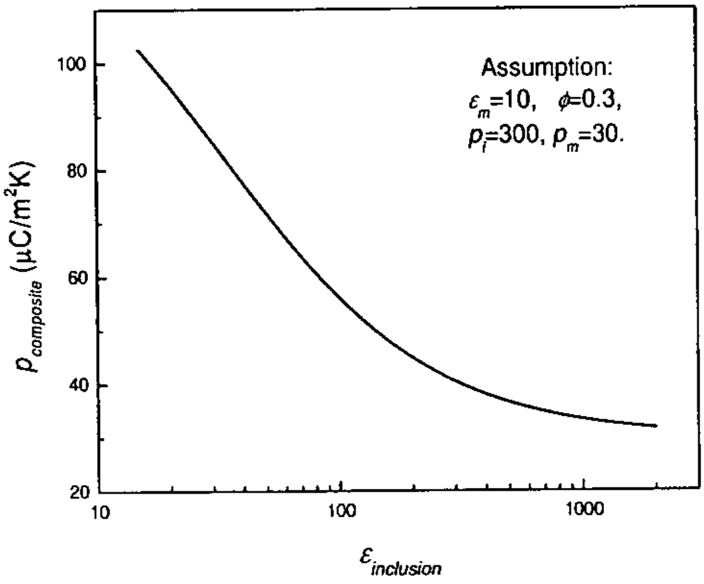

Figure 1.8 Dependence of pyroelectric coefficient of 0-3 composites on the relative permittivity of the inclusion phase.

Based on the above considerations the relative permittivity of the inclusion should be low in order to obtain good pyroelectric properties, hence triglycine sulfate (TGS) which has a high pyroelectric coefficient and a low relative permittivity would be an ideal material to be used as the inclusion phase. In previous publications, studies on TGS/PVDF 0-3 composites have been reported (as shown in Section 1.2.3). However, there is no systemic study on TGS/P(VDF-TrFE) 0-3 composites. In this thesis, the dielectric, piezoelectric and pyroelectric properties of TGS/P(VDF-TrFE) 0-3 composites are studied in detail.

Nonferroelectric fillers, such as tartaric acid [Krug, 1985], have also been used in 0-3 composites. In this work, we attempt to use a nonferroelectric filler montmorillonite (MMT) which is a kind of layered silicate. MMT has been widely used in layered silicate/polymer nanocomposites to improve the mechanical and chemical properties of common polymers or the conductivities of conductive polymers. However, MMT has not been incorporated in a ferroelectric polymer in order to improve the poling efficiency or to enhance the polarization. In this work, MMT powder is embedded in P(VDF-TrFE) matrix to form MMT/P(VDF-TrFE) 0-3 composites. The dielectric, piezoelectric and pyroelectric properties of MMT/P(VDF-TrFE) are investigated.

1.5 Outline of Thesis

Following this introduction, there are five Chapters entitled:

- Preparation of TGS/P(VDF-TrFE) 0-3 Composites;
- Structures and Phase Transitions of TGS/P(VDF-TrFE) 0-3 Composites;
- Dielectric, Piezoelectric and Pyroelectric Properties of TGS/P(VDF-TrFE) 0-3 Composites;
- Studies of MMT/P(VDF-TrFE) 0-3 Nanocomposites;
- Conclusions and Suggestions for Future Work.

In Chapter 2, the structural and ferroelectric properties of TGS crystals are first introduced. The fabrication process of TGS/P(VDF-TrFE) (70/30 mol%) 0-3 composites with various weight percents of TGS is then described. The densities of TGS powder and the P(VDF-TrFE) film are measured in order to determine the volume percent of TGS in the composites.

In Chapter 3, field emission scanning electron microscopy (FE-SEM) is employed to study the cross-sectional microstructures of the 0-3 composites in order to ensure that the TGS particles have been well dispersed in the copolymer matrix. X-ray diffraction (XRD) technique is used to confirm the compositions and crystalline phases of the composites. The phase transition behavior in the composites is studied by differential scanning calorimetry (DSC) and some thermodynamic parameters are obtained from the DSC thermograms.

The dielectric, piezoelectric and pyroelectric properties of TGS/P(VDF-TrFE) 0-3 composites are measured and discussed in Chapter 4. The experimental techniques and procedures are briefly explained. Results of the relative permittivity and pyroelectric coefficient are compared with the Bruggeman model and the effective-medium (EM) model, respectively. The pyroelectric figures of merit (FOM) of the composites are also calculated and presented in Chapter 4.

In Chapter 5, MMT/P(VDF-TrFE) 0-3 nanocomposites with various weight percents of MMT embedded in a P(VDF-TrFE) 80/20 mol% matrix are fabricated using a polymer intercalation method. The composites are characterized by XRD and DSC. The dielectric permittivity, polarization hysteresis, piezoelectric coefficient and pyroelectric coefficient are also measured.

Conclusions and suggestions for future work are given in Chapter 6.

Chapter 2

Preparation of TGS/P(VDF-TrFE) 0-3 Composites

In this Chapter, the structural and ferroelectric properties of triglycine sulfate (TGS) crystals were introduced. Fabrication of TGS/P(VDF-TrFE) (70/30 mol%) 0-3 composites with various weight percents of TGS were described. The densities of TGS powder and the P(VDF-TrFE) film were measured and the volume percent of TGS in the composite was then determined.

2.1 Introduction to TGS Crystals

The ferroelectric activity of triglycine sulfate, $(NH_2CH_2COOH)_3 \cdot H_2SO_4$ (abbreviated as TGS) was discovered by Matthias et al. in 1956 [Matthias et al., 1956]. It has immediately attracted the attention of many researchers because it exhibits ferroelectric properties at room temperature, and it can be easily grown into large sample from a water solution. In addition, TGS is one of the best pyroelectric materials for infrared detectors.

The Curie temperature of TGS lies at 49°C and the transition is of second order. The phase above the transition has monoclinic symmetry and belongs to the centrosymmetrical class 2/m. Below the transition temperature, the mirror plane disappears and the crystal belongs to the polar point group 2 of the monoclinic system.

In the ferroelectric phase, the spontaneous polarization is found along the direction of the b-axis of the monoclinic cell. Details of the crystal structure have been clarified by X-ray diffraction [Hoshino et al., 1959], as shown in Figure 2.1. There are two different kinds of glycine group NH_2CH_2COOH in the crystal structure of the TGS molecule. The glycine group I is a 'nonplanar type' with the two carbon atoms and the two oxygen atoms all lying roughly in one plane, while the nitrogen atom is apparently displaced out of the plane. Both glycine groups II and III are 'quasi-planar type', i.e., all the carbon, oxygen and the nitrogen atoms of one group lie in the same plane. The glycine groups II and III are mirror images of each other and are almost perpendicular to the b-axis. The oxygen atoms in group II and group III are connected by a hydrogen bond with a distance of 2.5Å. This hydrogen bond connecting glycine groups II and III plays an important role in the ferroelectric phase transition.

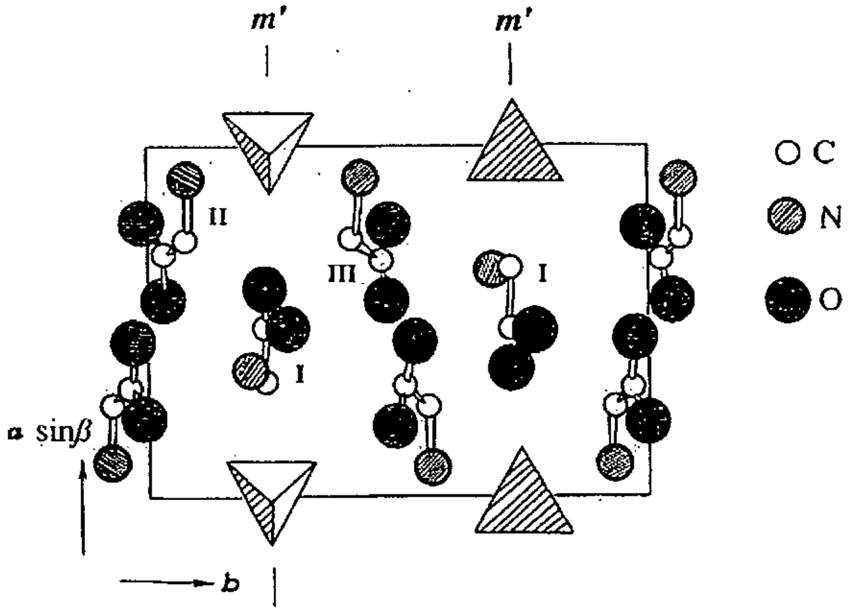

Figure 2.1 Structure of TGS: I, II and III are glycine groups and m' is a mirror symmetry plane. [Hoshino et al., 1959]

The crystallographic structure of TGS is more complex than some other ferroelectric crystals, however, its physical properties, especially ferroelectricity, are very prominent and rather simple to understand. The temperature dependence of the relative permittivity along the polar axis is shown in Figure 2.2 and there is a peak in the vicinity of the transition temperature T_c.

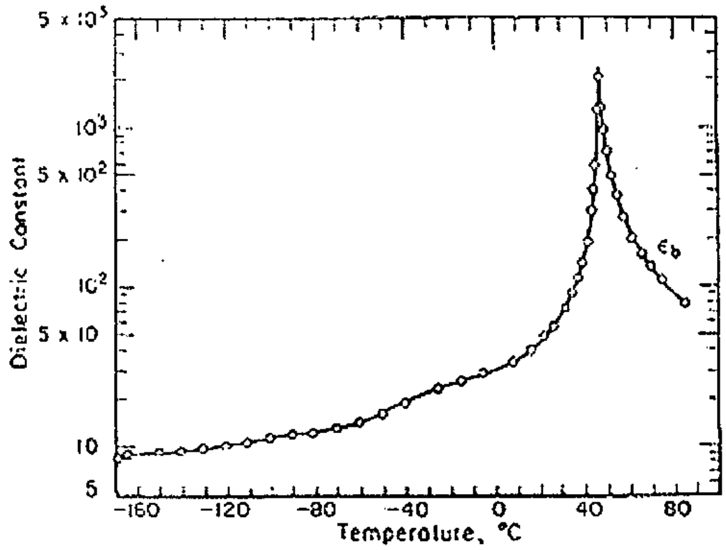

Figure 2.2 Relative permittivity of TGS as a function of temperature. [Hoshino et al., 1959]

The temperature dependence of the spontaneous polarization P_s is described in Figure 2.3 [Chynoweth, 1960], and it is a typical second order transition. The value of P_s at room temperature is about 2.3~2.8 $\mu C/cm^2$. Below 0°C, the spontaneous polarization increases slowly with decreased temperature and reaches a value of approximately 4.3 $\mu C/cm^2$ at -140°C. The coercive field E_c of TGS had been measured by a number of researchers, and it is strongly dependent on the amplitude and frequency of the applied field. The temperature dependence of E_c measured with a 50 Hz, 1500 V/cm field is depicted in Figure 2.4 [Domanski, 1958]. The value of E_c is about 430 V/cm at room temperature. Below -10°C, E_c increases sharply because the relaxation time of the reversal process increases rapidly with decreasing temperature.

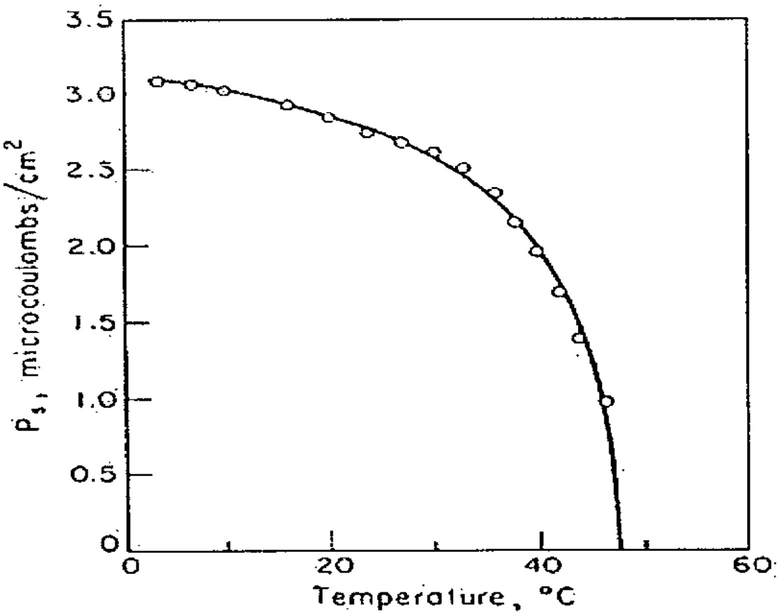

Figure 2.3 Spontaneous polarization of TGS as a function of temperature. [Chynoweth, 1960]

TGS crystal is widely used as a pyroelectric material in infrared detectors. It has a large pyroelectric coefficient of 200~350 μC/m^{2}K at room temperature, and it has the largest sensitivity D^* among the known pyroelectric materials. TGS has high figures of merit but is a rather fragile, water-soluble single-crystal material. It can be modified to withstand temperatures in excess of its Curie point without depoling, but it cannot be heated in a vacuum to the temperature necessary for outgassing without decomposition. It is difficult to handle and cannot be used in devices where it would be subjected to

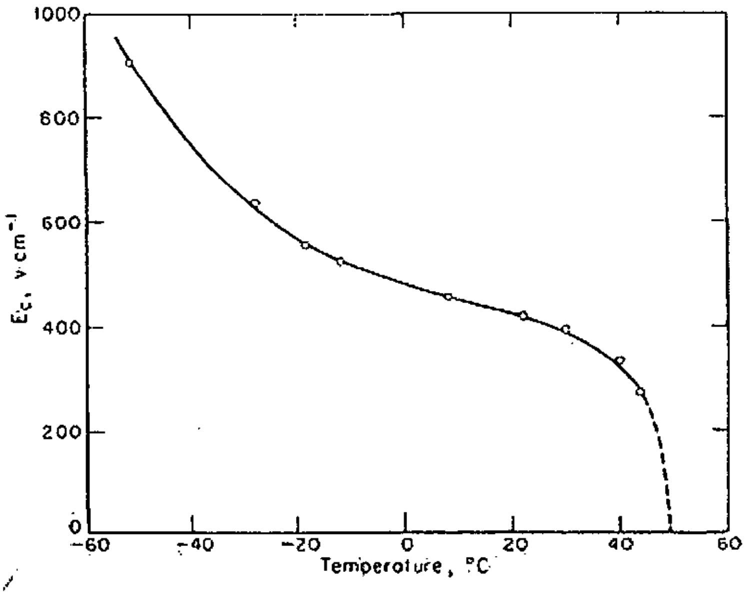

Figure 2.4 Coercive field of TGS as a function of temperature. [Damanski, 1958]

either a high vacuum or high humidity. In contrast, P(VDF-TrFE) has lower figures of merit but can be easily fabricated into large area thin film and is mechanically robust. It has relatively higher resistance to heat, vacuum and moisture than TGS. It also has lower heat conductivity and lower permittivity so that both thermal and electrical couplings between neighboring elements on the same piece of material are minimized. Based on the complementary characteristics of TGS and P(VDF-TrFE), we fabricated TGS/P(VDF-TrFE) 0-3 composites in order to combine their advantages and also minimize the disadvantages.

2.2 Fabrication of TGS/P(VDF-TrFE) 0-3 Composites

2.2.1 Materials Used

The P(VDF-TrFE) 70/30 mol% copolymer used as the matrix was supplied by Piezotech, France. The TGS single crystal and powder were supplied by the Institute of Crystal Materials, Shandong University, China.

To minimize the particle size of the TGS powder obtained from crashed TGS single crystals, we firstly ground them by hand. After that, the powder was dispersed in ethanol and ball-milled at 250 rpm for 10h in a ball miller (Nanjing University Instrument QM-13P). After evaporation of ethanol, the TGS powder was ready for the fabrication of 0-3 composites.

The mean particle size of the powder was measured by a centrifugal automatic particle size distribution analyzer (Horiba CPCA-700) using a noncontact measuring method based on liquid-phase sedimentation (measuring the change in particle concentrations on the basis of light transmission). Figure 2.5 shows the TGS particle size distribution and the medium value is about 5.7 μm. At the same time, the TGS particles were also measured by a scanning electron microscope (JEOL JSM-6335F FE-SEM), as shown in Figure 2.6.

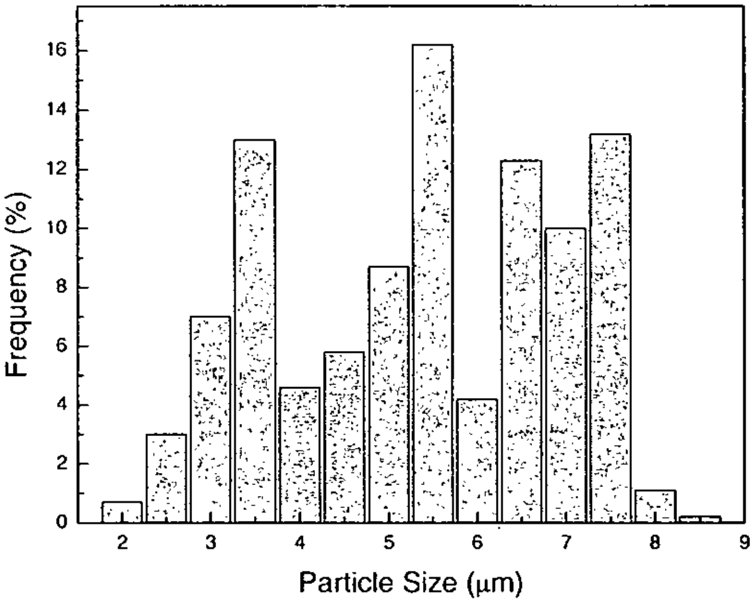

Figure 2.5 TGS powder particle size distribution.

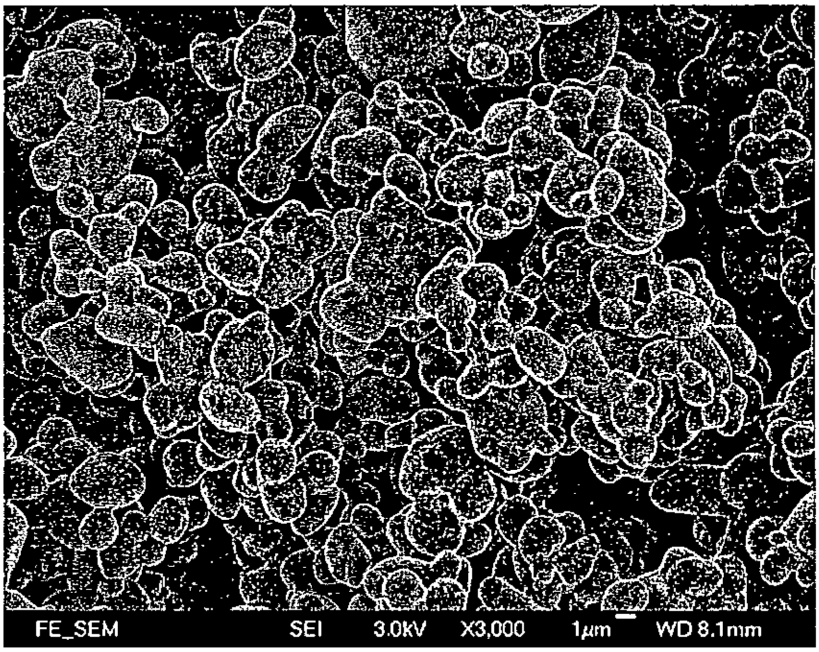

Figure 2.6 SEM micrograph of TGS powder.

2.2.2 Fabrication Process

Powder of P(VDF-TrFE) 70/30 mol% copolymer was dissolved in dimethylformamide (DMF) and then a predetermined amount of TGS powder was dispersed into the solution. After 20 minutes of ultrasonic agitation, the solution was then stirred magnetically at 60 °C until a gel-form composite was obtained. In order to remove the solvent completely, the thick composite film was dried at 80°C in a vacuum oven for 12 h.

A hot compression moulding method was employed to fabricate 0-3 composite films. The thick composite film was cut into small pieces and placed on a circular steel mould (Constant Thickness Film Maker, SPECAC P/N 15620). Between the sample and the steel mould, two pieces of polyimide films were used to prevent the composite film from sticking onto the mould after a hot pressing process and also to produce a smoother surface. The mould was then placed on a hot-press machine (CARVER 2699-127) with a temperature of 160°C. After 10 minutes of preheating, about 15 MPa pressure was applied on the mould for 15 minutes. Higher temperature or pressure should not be used to prevent the TGS from decomposing. The mould was then removed and cooled to room temperature in air. In order to enhance the crystallinity, the composite films were annealed at 130°C for 2 h. The TGS/P(VDF-TrFE) 0-3 composites with 4, 10, 20, 25, 30, 40wt% of TGS were finally obtained. The final thickness of the composite film was about 70 μm. Cr-Au electrodes were deposited on both sides of the film for subsequent property measurements.

2.2.3 Sample Density

A flotation method was used to determine the density of the TGS single crystal and the pure copolymer film. In this method, a small piece of sample was immersed in a mixture of two different liquids, which were dibromomethane (DBM) with a higher density of 2488 kg/m^3 and ethanol with a lower density of 788 kg/m^3 at room temperature. We can vary the proportion of DBM and ethanol until the sample is neutrally buoyant in the mixture. The density of this mixture was measured by using a density bottle (E-MIL BRE002). The density of TGS single crystal and P(VDF-TrFE) 70/30 mol% copolymer film is found to be ρ_{TGS} =1690 kg/m^3 and $\rho_{copolymer}$ =1902 kg/m^3, respectively. Using these values, the volume percent ϕ of TGS in the 0-3 composites can be calculated and the results are tabulated in Table 2.1.

Table 2.1 Volume percentages of TGS in TGS/P(VDF-TrFE) 0-3 composites.

wt %	4	10	20	25	30	40
vol %	4.5	11.1	22.0	27.3	32.6	42.9

Chapter 3

Structures and Phase Transitions of TGS/P(VDF-TrFE) 0-3 Composites

In this Chapter, the structural properties of TGS/P(VDF-TrFE) 0-3 composites were investigated by scanning electron microscopy (SEM), X-ray diffraction (XRD) and differential scanning calorimetry (DSC). A field emission SEM was employed to study the cross-sectional microstructures of the 0-3 composites in order to make sure that the TGS particles were well dispersed in the copolymer matrix. XRD was used to confirm the compositions and crystalline phases of the composites. The transition behavior of the composites was studied by DSC and some thermodynamic parameters were obtained from the DSC thermograms.

3.1 Microstructures

The fractured surfaces of the composites were examined by a field emission scanning electron microscope (JEOL JSM-6335F FE-SEM) in order to observe how the TGS particles disperse in the copolymer matrix. To obtain a fractured surface, the film was dipped into liquid nitrogen for 1 minute, then it was taken out and fractured in air. The fractured surface was coated with gold before imaging in order to improve the quality of images. The cross-sectional micrographs of the composites with various volume percentages of TGS are shown in Figure 3.1: (a) 4.5 vol%, (b) 11.1 vol%, (c) 22.0 vol%,

(d) 27.3 vol%, (e) 32.6 vol% and (f) 42.9 vol%. It is seen that the TGS particles are dispersed rather uniformly in the copolymer matrix.

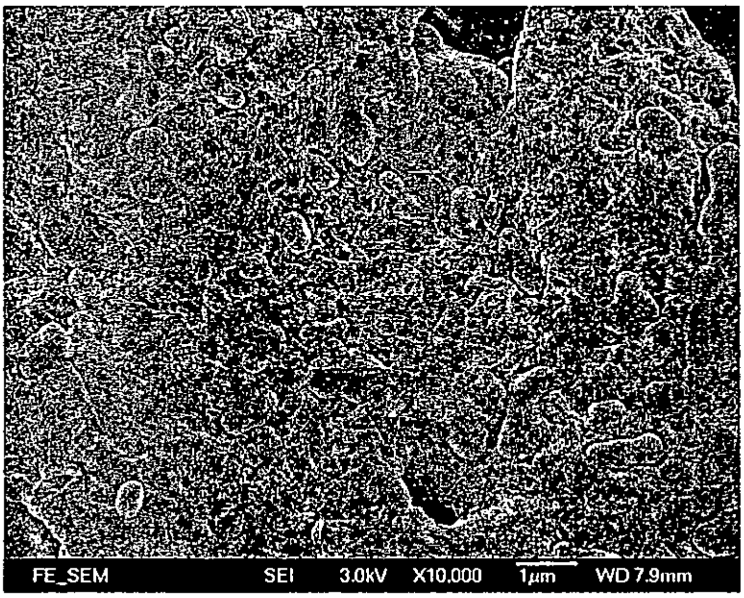

(a)

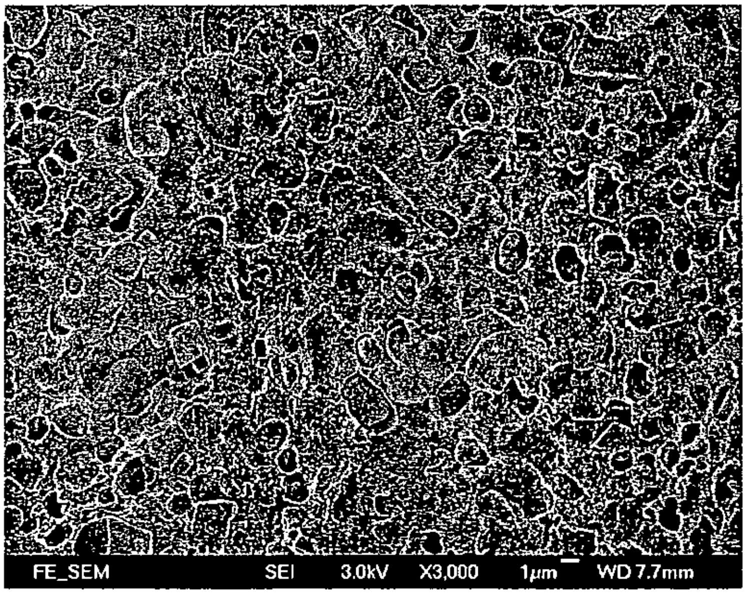

(b)

Figure 3.1 SEM micrographs of the fracture surface for TGS/P(VDF-TrFE) 0-3 composites with (a) 4.5 vol%, (b) 11.1 vol%, (c) 22.0 vol%, (d) 27.3 vol%, (e) 32.6 vol% and (f) 42.9 vol% of TGS.

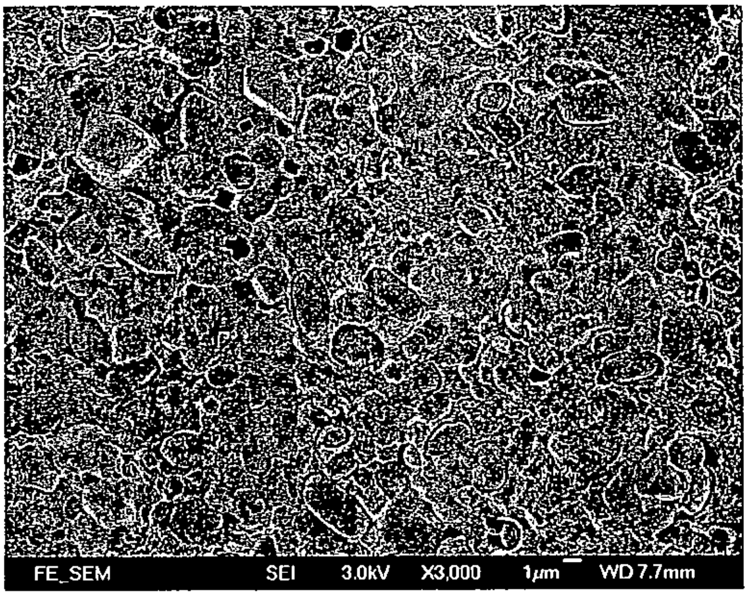

(c)

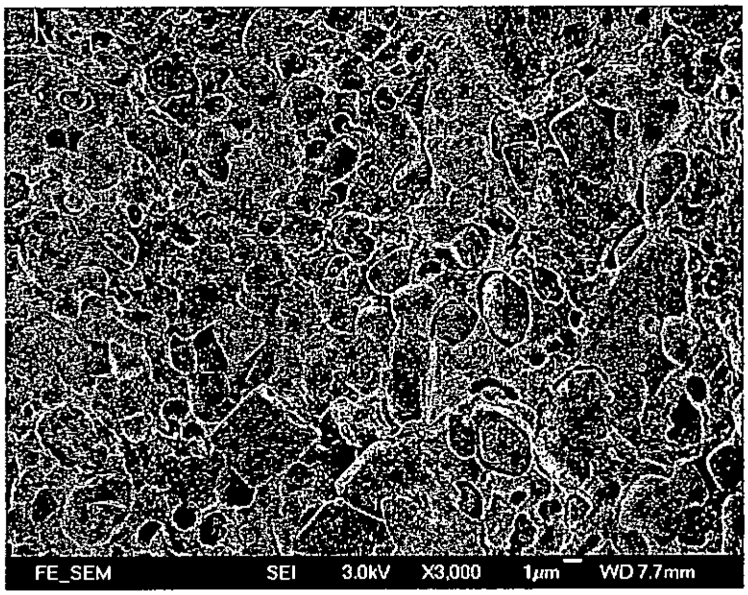

(d)

Figure 3.1 Continued

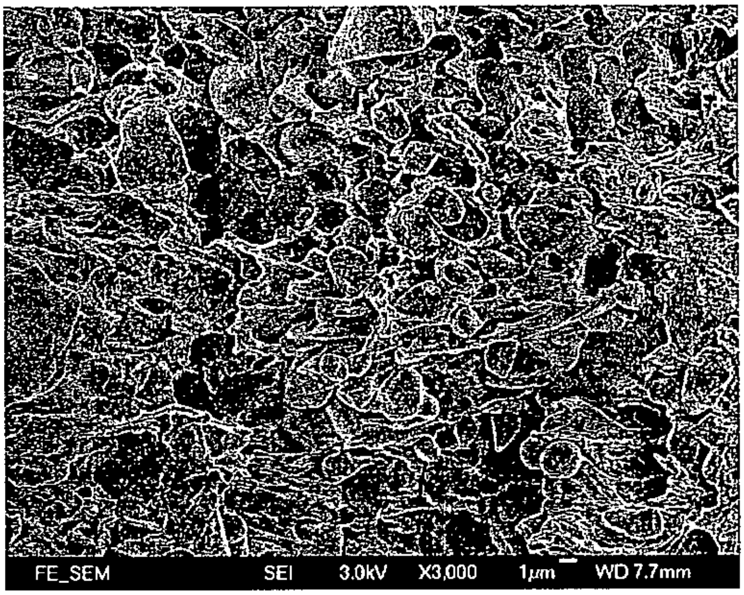

(e)

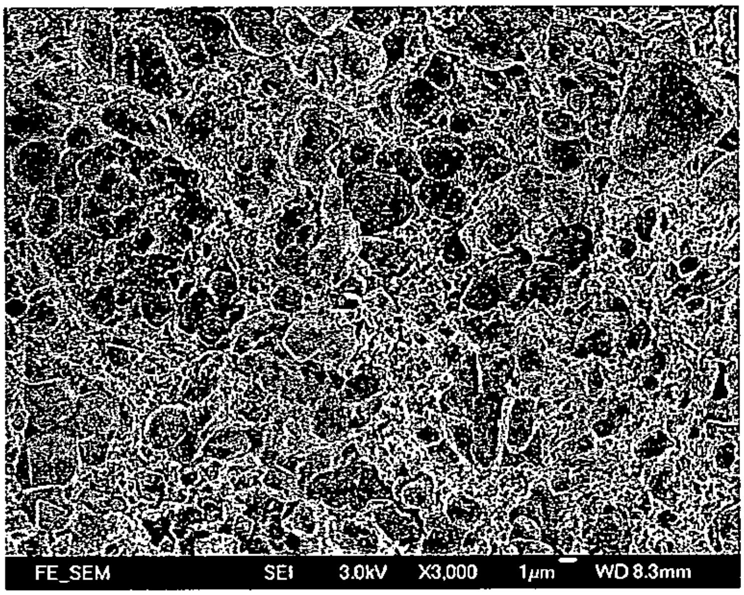

(f)

Figure 3.1 Continued

3.2 XRD Characterization

X-ray diffractometry (XRD) is a versatile method to reveal detailed information about the physical structure of various materials. As it can be applied to all kinds of materials and is non-destructive, XRD becomes an indispensable method for materials characterization and quality control. In our experiment, an X-ray diffractometer (D8 Advanced Bruker Analytical XRD) equipped with Ni-filtered Cu-K_α radiation (λ=1.541Å) was used and operated in the θ-2θ scanning mode. The scanning speed was 0.04°/s.

The XRD patterns of the 0-3 composites are shown in Figure 3.2 and for comparison, the patterns of P(VDF-TrFE) copolymer and TGS powder are also presented. For the pure copolymer (Figure 3.2 (a)), the peak at 2θ~19° corresponds to the composite peak of the (200,110) reflections of the β phase (polar phase) composed of all *trans* chains [Lovinger et al., 1982]. In the XRD patterns of TGS powder (Figure 3.2 (h)), random orientation diffraction peaks associated with the TGS reflections are observed. In the composites, the copolymer reflections and the TGS reflections are both observed. With the increase in the amount of TGS in the composites, the diffraction peak intensities corresponding to the TGS reflections are gradually enhanced, which confirms that TGS powder has been embedded into the copolymer matrix effectively without decomposition.

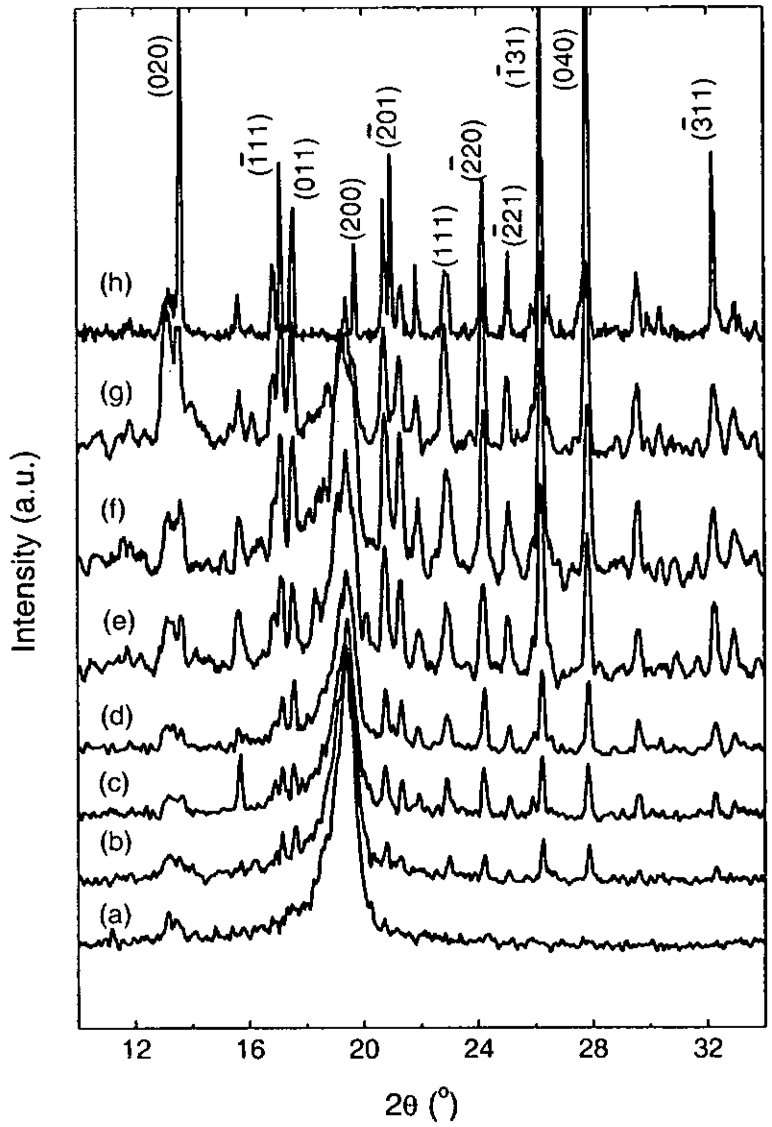

Figure 3.2 XRD patterns for (a) P(VDF-TrFE), TGS/P(VDF-TrFE) 0-3 composites with (b) 4.5 vol%, (c) 11.1 vol%, (d) 22.0 vol%, (e) 27.3 vol%, (f) 32.6 vol% and (g) 42.9 vol% of TGS, and (h) TGS powder.

3.3 DSC Thermal Analysis

3.3.1 Experimental Techniques

Differential scanning calorimetry (DSC) is a technique widely used to study the transitions in the sample material such as melting, glass transitions, solid-state transitions or crystallization. To study the endothermic and exothermic reactions, DSC is usually programmed to scan a temperature range at a linear rate. The energy absorbed or evolved by the sample is compensated by a heater, which is located in the sample holder, to keep the sample holder temperature identical to that of the reference holder. The continuous adjustment of the heater power (energy per unit time) provides a varying electrical signal (in milliwatts) equivalent to the varying thermal behavior of the sample. The heat capacity under constant pressure per unit mass C_p^{mass} and the transition enthalpy ΔH can be determined by:

$$Power = \frac{dQ}{dt} = m \cdot C_p^{mass} \cdot \frac{dT}{dt} \tag{3.1}$$

$$\Delta H = \frac{1}{m} \cdot \int_{t_1}^{t_2} \frac{dQ}{dt} \cdot dt = \int_{T_1}^{T_2} C_p^{mass} \cdot dT \tag{3.2}$$

where m is the sample mass, dQ/dt the value of the heater power which is obtained from the experiment and dT/dt is the heating rate. In our experiment, the instrument DSC 7 (The Perkin-Elmer Co. USA) was used for the thermal analysis. About 10 mg sample was encapsulated in an aluminum pan and another empty pan served as a reference. The heating rate was set at 10°C/min in the temperature range of -20°C to 180°C.

3.3.2 Results and Discussion

Figure 3.3 shows the DSC thermogram of P(VDF-TrFE) 70/30 mol% copolymer. During the heating process, there is a broad endothermic peak near 101°C which corresponds to the ferroelectric to paraelectric (F-P) phase transition T_c and a sharp endothermic peak at 150.5°C associated with the melting temperature T_m. During the cooling process, the crystallization temperature lies at 135.5°C and the Curie temperature exhibits a strong thermal hysteresis which appears at around 60°C. The phase transition of the copolymer (70/30 mol%) is a first-order transition [Tashiro et al., 1984] in which thermal hysteresis is usually observed [Lines et al., 1977]. Figure 3.4 shows the DSC thermogram of the TGS powder. During the heating and cooling process, the Curie transition of TGS appears at 49°C.

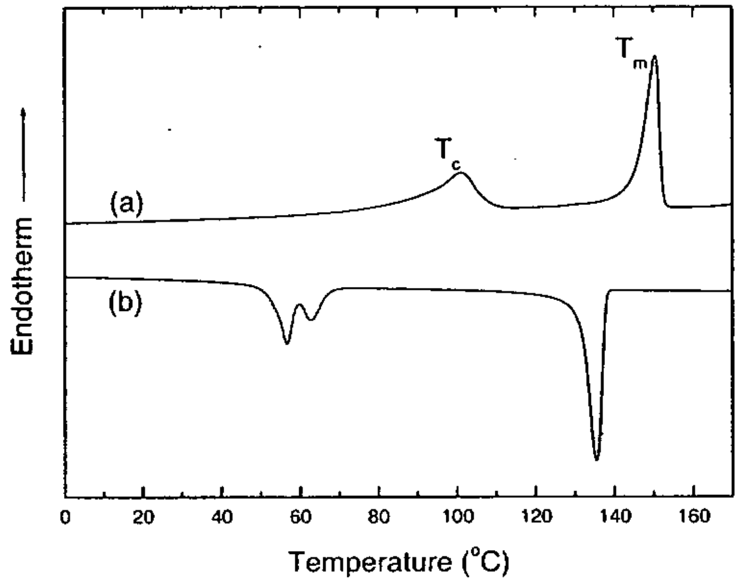

Figure 3.3 DSC thermograms of P(VDF-TrFE) during (a) heating and (b) cooling.

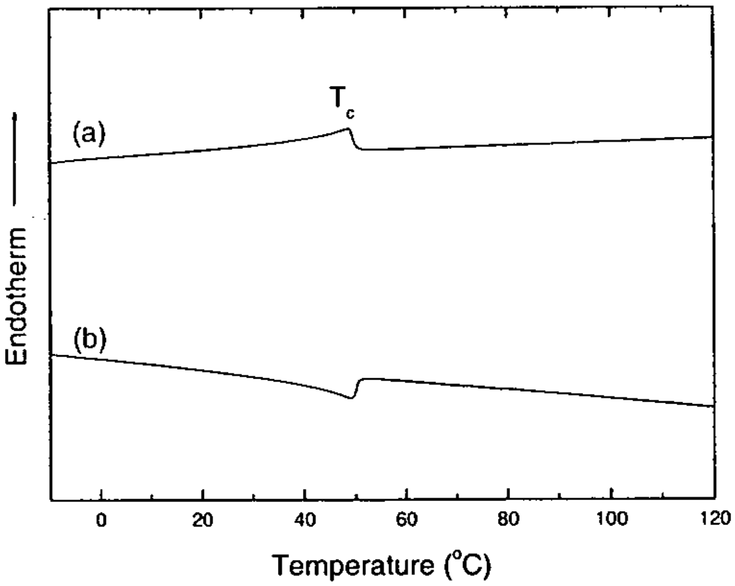

Figure 3.4 DSC thermograms of TGS powder during (a) heating and (b) cooling.

Figure 3.5 presents the DSC thermograms of the 0-3 composites during the heating process and for comparison, the DSC curves of the pure copolymer and TGS powder are also plotted. The phase transition heat ΔH of TGS is much smaller than that of P(VDF-TrFE). However, we can still observe the endothermic peak at around 49°C associated with the Curie temperature of TGS in the composites and the intensity increases with increasing volume percent of TGS ϕ. The composites also exhibit the endothermic peak in the vicinity of the Curie temperature of the copolymer and the intensity decreases gradually with increasing ϕ. The DSC thermograms during the cooling process are also plotted in Figure 3.6. The exothermic peak of TGS in the composites cannot be clearly identified because it overlaps with the phase transition of the P(VDF-TrFE) matrix.

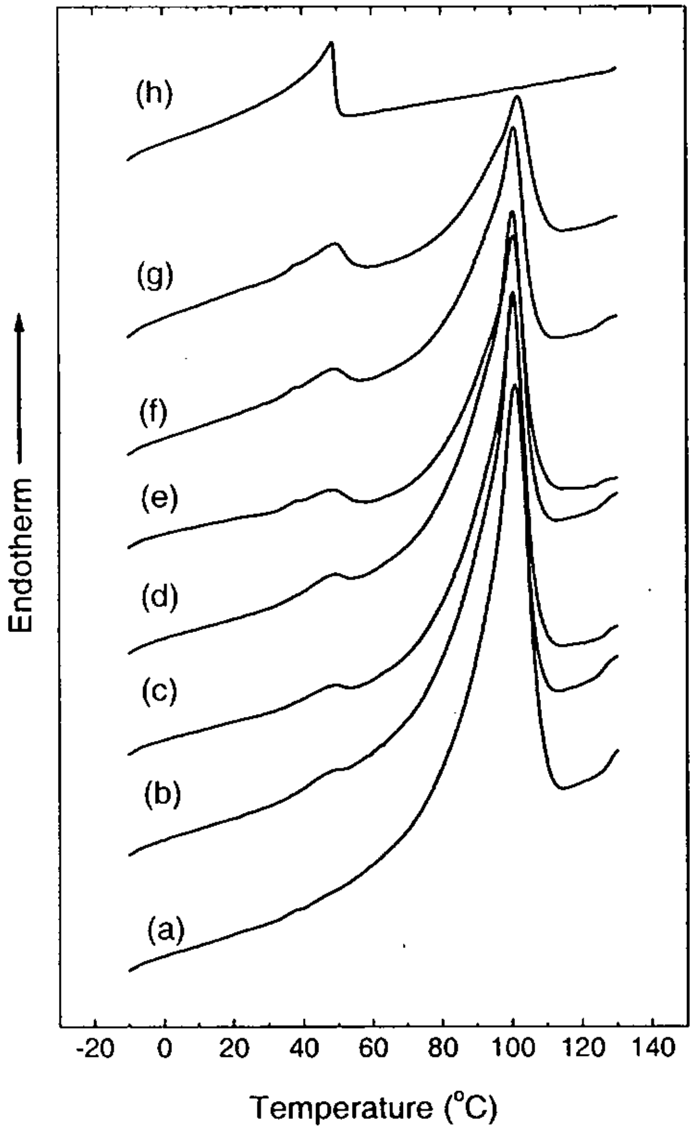

Figure 3.5 DSC thermograms for (a) P(VDF-TrFE), TGS/P(VDF-TrFE) 0-3 composites with (b) 4.5 vol%, (c) 11.1 vol%, (d) 22.0 vol%, (e) 27.3 vol%, (f) 32.6 vol% and (g) 42.9 vol% of TGS, and (h) TGS powder during the heating process.

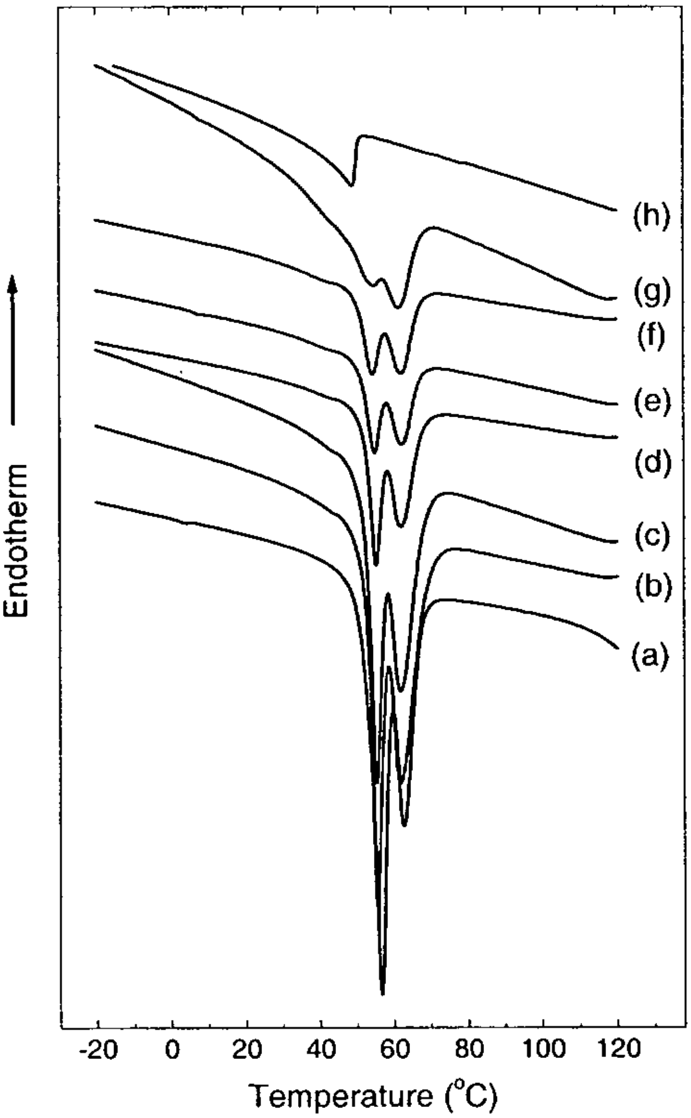

Figure 3.6 DSC thermograms for (a) P(VDF-TrFE), TGS/P(VDF-TrFE) 0-3 composites with (b) 4.5 vol%, (c) 11.1 vol%, (d) 22.0 vol%, (e) 27.3 vol%, (f) 32.6 vol% and (g) 42.9 vol% of TGS, and (h) TGS powder during the cooling process.

Table 3.1 summarizes the heat capacities C_p^{mass} and $C_p^{vol.}$ and the phase transition heat ΔH of P(VDF-TrFE) copolymer, TGS and the 0-3 composites determined during the heating process. The heat capacity per unit mass C_p^{mass} is calculated by using Equation 3.1 and the heat capacity per unit volume $C_p^{vol.}$ is calculated by using:

$$C_p^{vol.} = \rho_{composite} \cdot C_p^{mass} \tag{3.3}$$

$$\rho_{composite} = \phi \cdot \rho_{TGS} + (1-\phi) \cdot \rho_{copolymer} \tag{3.4}$$

where ρ_{TGS} (=1690 kg/m^3) and $\rho_{copolymer}$ (=1902 kg/m^3) have been measured in Chapter 2. The phase transition heat ΔH is calculated by using Equation 3.2. The heat capacities of TGS and P(VDF-TrFE) are similar to each other, so $C_p^{vol.}$ varies very little with ϕ. The phase transition heat of TGS ΔH_{TGS} increases and the phase transition heat of the copolymer $\Delta H_{copolymer}$ decreases with increasing ϕ.

Table 3.1 Specific heat C_p and phase transition heat ΔH for P(VDF-TrFE), TGS and TGS/P(VDF-TrFE) 0-3 composites during the heating process.

TGS Volume Percent, ϕ	$\rho_{composite}$ (kg/m^3)	C_p^{mass} $(J/g\cdot K)$		$C_p^{vol.}$ $(MJ/m^3\cdot K)$		ΔH_{TGS} (J/g)	$\Delta H_{copolymer}$ (J/g)
		25°C	*40°C*	*25°C*	*40°C*		
P(VDF-TrFE)	1902	1.10	1.16	2.09	2.21	---	15.137
4.5 vol%	1892	1.10	1.17	2.08	2.21	0.057	14.903
11.1 vol%	1878	1.12	1.19	2.10	2.23	0.162	13.087
22.0 vol%	1855	1.13	1.21	2.10	2.24	0.306	11.839
27.3 vol%	1844	1.15	1.22	2.12	2.25	0.429	10.265
32.6 vol%	1833	1.16	1.24	2.13	2.27	0.561	9.622
42.9 vol%	1811	1.18	1.27	2.14	2.29	0.808	8.362
TGS	1690	1.29	1.38	2.18	2.33	1.809	---

3.4 Summary

The cross-sectional microstructures of the TGS/P(VDF-TrFE) 0-3 composites were observed by a FE-SEM and a good dispersion of TGS particles in the copolymer matrix was confirmed. The crystalline structures of the two phases in the 0-3 composites were studied by XRD. The X-ray reflections of TGS and copolymer both appeared in the composites. With an increase in the volume percent of TGS ϕ, the intensity of the copolymer reflection at $2\theta \sim 19°$ was suppressed gradually and at the same time the reflections of TGS became more and more obvious. The DSC technique was employed to investigate the phase transitions in the 0-3 composites, and the specific heat C_p and the phase transition heat ΔH were also calculated from the thermograms. Both the Curie temperature of TGS at 49 °C and that of P(VDF-TrFE) at about 101 °C (during heating) and 60 °C (during cooling) appeared in the DSC thermogram of the composites and the changes of ΔH and the intensity of the endothermic/exothermic peaks followed the change in ϕ. From the investigations described above, we can draw the conclusion that TGS/P(VDF-TrFE) 0-3 composites have been successfully fabricated and the structural properties of the composites show systematic variations with different volume percents of TGS.

Chapter 4

Dielectric, Piezoelectric and Pyroelectric Properties of TGS/P(VDF-TrFE) 0-3 Composites

The hysteresis behavior and the dielectric, piezoelectric and pyroelectric properties of TGS/P(VDF-TrFE) 0-3 composites were studied and discussed in this Chapter. The hysteresis loops of the composites were obtained and a poling process was then selected based on these results. The relative permittivity and dielectric loss of the composites were measured as a function of temperature and frequency. The piezoelectric and pyroelectric coefficients were also measured. The pyroelectric coefficient of the composites was modeled using an effective-medium model. Finally, the pyroelectric figures of merit of the poled 0-3 composites were calculated.

4.1 Hysteresis Measurement

4.1.1 Experimental Techniques

The behavior of polarization reversal can be described by a hysteresis loop. In this project, the hysteresis loops were obtained by a modified Sawyer-Tower circuit (Sawyer and Tower, 1930) as shown in Figure 4.1. A sinusoidal electric voltage at a frequency of

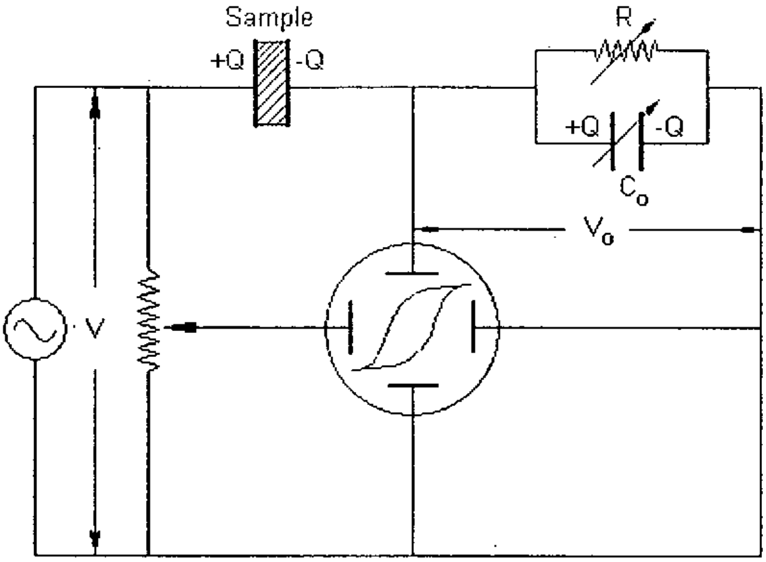

Figure 4.1 Schematic diagram of a modified Sawyer-Tower circuit. [Lines et al., 1977]

10 Hz was applied to the sample and the voltage *V* across the sample was connected to the horizontal plate of an oscilloscope. A reference capacitor C_o was connected in series with the sample and the voltage across the reference capacitor V_o was connected to the vertical plate of the oscilloscope. Thus, the electric polarization *P* of the sample is given by:

$$P \cong D = \frac{Q}{A} = \frac{C_o \cdot V_o}{A} \tag{4.1}$$

where D is the electric displacement and A is the area of the electrode. To ensure the full application of *V* across the sample, a reference capacitor with a capacitance of 1 μF, which is much larger than the capacitance of the sample, has been used in the measurement.

4.1.2 Results and Discussion

Figure 4.2 shows the hysteresis loop of a TGS single crystal measured under an a.c. electric field of 0.1 V/μm at room temperature. It is found that the remanent polarization P_r and the coercive field E_c are equal to 3.33 μC/cm^2 and 0.029 V/μm, respectively. Figure 4.3 shows the hysteresis loop of P(VDF-TrFE) copolymer measured under an a.c. electric field of 100 V/μm at room temperature. The remanent polarization P_r and the coercive field E_c are found to be 6.50 μC/cm^2 and 56.5 V/μm, respectively. The hysteresis loops of 0-3 composites with various volume fractions of TGS measured at room temperature are presented in Figure 4.4. Values of the P_r and E_c in composites with different volume percent of TGS ϕ are tabulated in Table 4.1. The remanent polarization decreases with an increase in ϕ and the coercive field also shows a slight decrease with increasing ϕ.

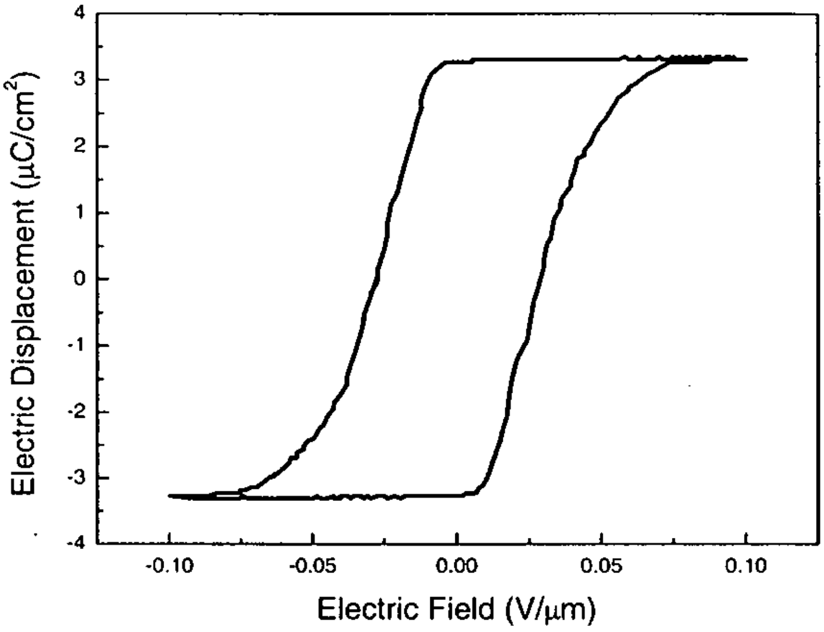

Figure 4.2 Hysteresis loop of TGS single crystal measured at room temperature.

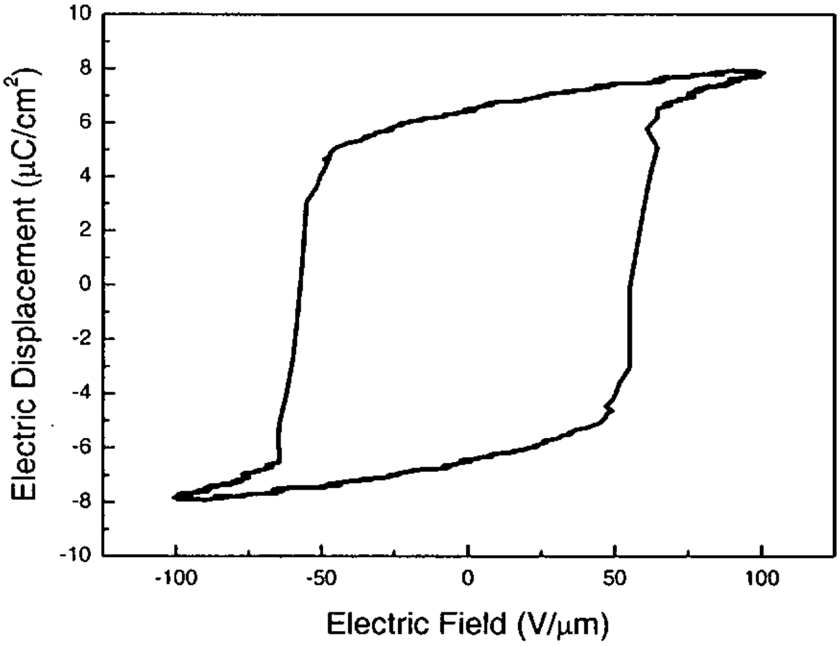

Figure 4.3 Hysteresis loop of P(VDF-TrFE) measured at room temperature.

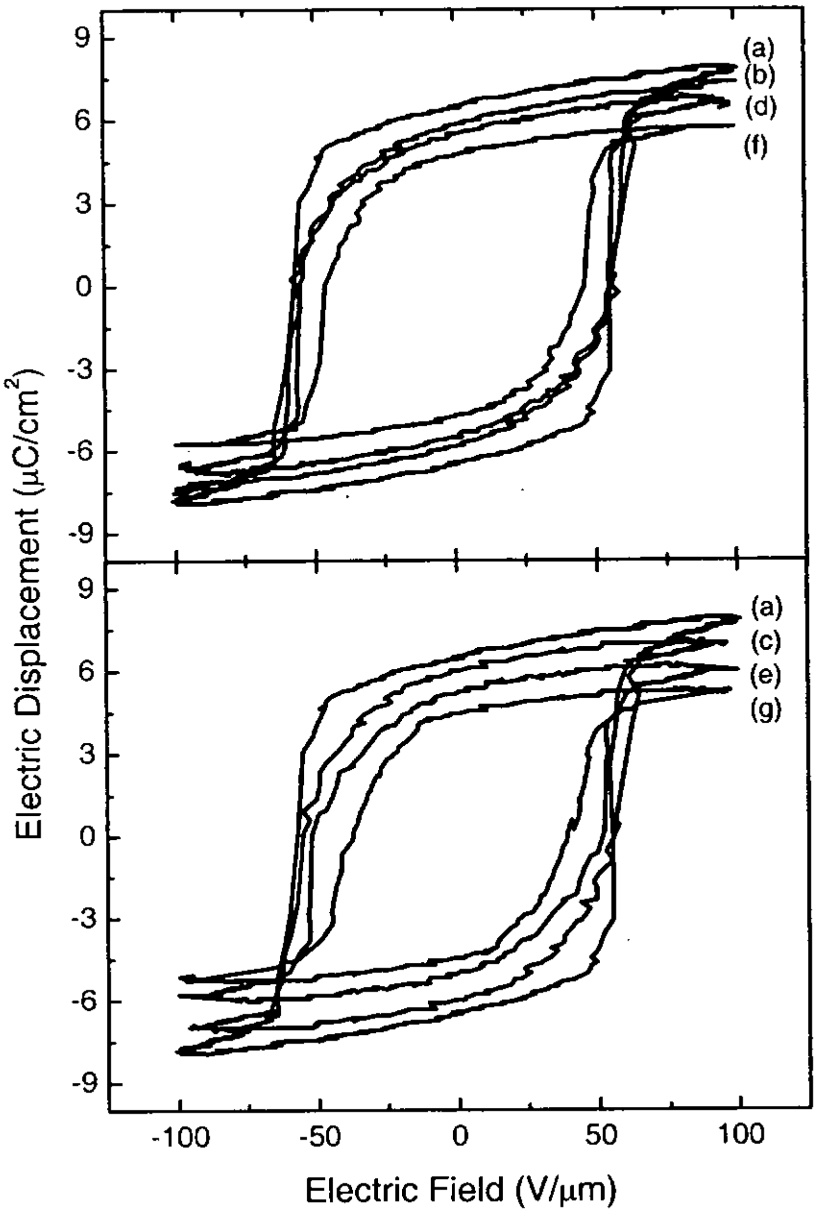

Figure 4.4 Hysteresis loops for (a) P(VDF-TrFE) and TGS/P(VDF-TrFE) 0-3 composites with (b) 4.5 vol%, (c) 11.1 vol%, (d) 22.0 vol%, (e) 27.3 vol%, (f) 32.6 vol% and (g) 42.9 vol% of TGS measured at room temperature.

Table 4.1 Remanent polarization and coercive field for P(VDF-TrFE), TGS single crystal and TGS/P(VDF-TrFE) 0-3 composites at room temperature.

Materials	P_r ($\mu C/cm^2$)	E_c ($V/\mu m$)
P(VDF-TrFE)	6.50	56.5
4.5 vol%	5.96	55.4
11.1 vol%	5.85	54.9
22.0 vol%	5.51	54.3
27.3 vol%	5.25	51.6
32.6 vol%	4.78	45.9
42.9 vol%	4.46	38.6
TGS	3.33	0.029

4.2 Poling Process

Ferroelectric ceramic/polymer composites do not exhibit piezoelectric or pyroelectric activity in the original state due to their randomly oriented domains and dipoles. To induce piezoelectric and pyroelectric activity, a strong electric field is applied to the material to align the randomly oriented dipoles along the applied field. This process is known as poling. After poling, a remanent polarization exists in the material, and so the material is piezoelectricly and pyroelectricly active.

4.2.1 Experimental Setup and Procedure for the Poling Process

In this project, a thermal poling method (a poling process conducted at an elevated temperature) was used and the experimental setup is shown in Figure 4.5. The sample was immersed in a silicone oil bath which served as a good insulating medium and also as a uniform heat bath. A temperature controller was used to control the current in the heater. A d.c. voltage was magnified 3000 times by an amplifier before being applied to the sample. A 1 MΩ resistor was connected in series with the sample to monitor the leakage current and another 100 MΩ resistor was also connected in series to ensure that the large current would not damage the amplifier in case of an electric breakdown.

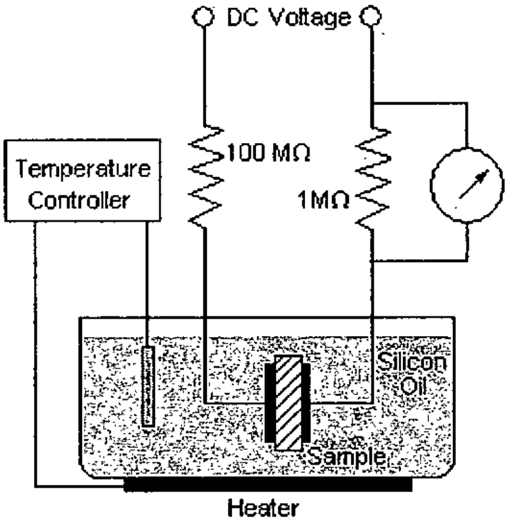

Figure 4.5 Schematic diagram of the experimental setup for d.c. poling.

The poling process for TGS/P(VDF-TrFE) 0-3 composites can be divided into two steps. Firstly, the sample was poled at 70 °C with a field of 60 V/μm for 30 min. At this temperature, only the copolymer phase was poled since TGS was in the paraelectric phase (the Curie temperature of TGS is 49 °C). Secondly, the field was decreased to 10 V/μm and the sample was cooled from 70 °C to ambient temperature in a period of about 1h with the electric field applied. During the cooling process, TGS underwent a transition from the paraelectric phase to the ferroelectric phase with the field applied. The field of 10 V/μm was high enough to pole the TGS phase (see later discussion). Samples with only the TGS phase poled were prepared using the second step. It is difficult to produce samples with only the copolymer phase poled as even if the field was switched off at 70 °C and the sample cooled through the Curie point of TGS, the TGS becomes partially poled due to space charges trapped in the copolymer matrix.

4.2.2 Poling Consideration

The major consideration in the poling of composites is the magnitude of the electric field experienced by the inclusion and the matrix phase. In this project, a two-layer capacitor (in series) model based on the Maxwell-Wagner interfacial polarization

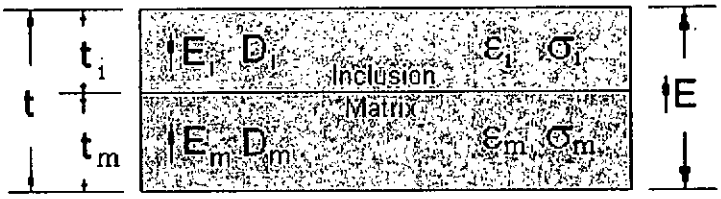

Figure 4.6 A two-layer capacitor model for 0-3 composites.

approach [Hippel, 1959] was used to estimate the poling efficiency. As shown in Figure 4.6, the inclusion phase (i) and the matrix (m) phase in the 0-3 composites can be approximated as two layers with individual permittivity ε and conductivity σ. The relationship between the total electric field E and the respective field E_i, E_m can be described as:

$$t \cdot E = t_i \cdot E_i + t_m \cdot E_m \quad \Rightarrow \quad E = \phi \cdot E_i + (1-\phi) \cdot E_m \tag{4.2}$$

where ϕ is the volume fraction of the inclusion and t is the thickness. If we assume that there is no interfacial charge, the relationship between the electric displacement of the inclusion and of the matrix is given by:

$$D_i = D_m \quad \Rightarrow \quad \varepsilon_i \cdot E_i = \varepsilon_m \cdot E_m \tag{4.3}$$

From Equations 4.2 and 4.3, the electric field applied on each phase can be calculated, respectively, as:

$$E_i = \frac{\varepsilon_m}{(1-\phi) \cdot \varepsilon_i + \phi \cdot \varepsilon_m} E \tag{4.4}$$

$$E_m = \frac{\varepsilon_i}{(1-\phi) \cdot \varepsilon_i + \phi \cdot \varepsilon_m} E \tag{4.5}$$

For poling the TGS/P(VDF-TrFE) 0-3 composites at 70 °C, ε_m is about 19, ε_i is about 170 (see Section 4.3.2) and E is 60 V/μm. If we take the composite with 4.5 and 42.9 vol% TGS as examples, the electric fields E_m experienced by the copolymer phase (calculated from Equation 4.5) are about 62.5 and 97 V/μm, respectively. The coercive field of P(VDF-TrFE) at room temperature is about 60 V/μm. However, with the increase of poling temperature the coercive field will decrease [Dias et al., 1997], presumably due to the higher mobility of ferroelectric domains at high temperature. Therefore at 70 °C, an electric field of 60 V/μm is sufficient to pole the copolymer phase to a highly polarized state [Chan et al., 1999]. It should be noted that the values of the electric field calculated from Equation 4.5 should be regarded as approximate, because an idealized model has been used. In the poling process on the TGS phase in the second step, the electric field applied on the composites is only 10 V/μm. We also take the composite with 4.5 and 42.9 vol% TGS as examples (where ε_i =23.3, ε_m=11.70 at room temperature), the electric fields E_i experienced by the TGS phase (calculated from Equation 4.4) are about 5.1 and 6.4 V/μm, respectively, which are already much higher than the coercive field of TGS at room temperature (E_c=0.03 V/μm). In addition, the composites are cooled through the Curie temperature of TGS where quite small field should be sufficient to cause the TGS phase to be polarized. For the preparation of samples with only the TGS phase poled, only the poling process in the second step needs to be applied.

4.3 Dielectric Properties of TGS/P(VDF-TrFE) 0-3 Composites

4.3.1 Introduction

For most applications of ferroelectric materials the relative permittivity and dielectric loss are important practical parameters, and studies of the dielectric properties provide information on the structure and phase transition of ferroelectric materials [Xu, 1991].

The permittivity ε describes the ability of a material to resist the formation of an electric field within it. When an electric field is applied, the total current flowing in the material is in general made of two parts: conduction current and displacement current. The permittivity ε is defined as the ratio of the electric displacement in the medium and the electric field strength (D/E). In the common case of an isotropic medium, **D** and **E** are parallel and ε is a scalar, but in more general anisotropic media ε is a second-rank tensor.

In engineering applications, permittivity is often expressed in relative term, a dimensionless relative permittivity or dielectric constant ε_r, normalized to the absolute vacuum permittivity $\varepsilon_o = 8.854*10^{-12}$ F/m. For a parallel plate capacitor containing a dielectric medium, the relative permittivity ε_r is given by:

$$\varepsilon_r = \frac{C \cdot d}{A \cdot \varepsilon_o} \tag{4.6}$$

where C is the capacitance of the sample, d the thickness of the sample and A is the area of the electrode. For a perfect dielectric, when an electric field is applied, only the displacement current appears. However the dielectric loss (related to the conduction current) always exists in realistic materials, and ε_r should be written in a complex form:

$$\varepsilon_r(\omega) = \varepsilon_r^{'}(\omega) + i\varepsilon_r^{''}(\omega) \tag{4.7}$$

where $\varepsilon_r^{'}(\omega)$ is the real part of the relative permittivity and $\varepsilon_r^{''}(\omega)$ is the imaginary part which represents dielectric loss. Instead of $\varepsilon_r^{''}$, the loss factor *tanδ* is frequently used by engineers to express dielectric loss and its definition is:

$$\tan\delta = \varepsilon_r^{''} / \varepsilon_r^{'} \tag{4.8}$$

The dielectric loss can also be described by the electric conductivity σ which is given by:

$$\sigma(\omega) = \omega\varepsilon_o\varepsilon_r^{''}(\omega) \tag{4.9}$$

Therefore, using $\varepsilon_r^{'}$ together with one of the three parameters: $\varepsilon_r^{''}$, *tanδ* or σ, we can completely describe the behavior of a dielectric material in an electric field.

4.3.2 Experimental Techniques

In this study, the relative permittivity and dielectric loss of TGS/P(VDF-TrFE) 0-3 composites as a function of temperature from -20 °C to 120 °C at 10 kHz were determined using an impedance analyzer (HP4194A) equipped with a temperature chamber (ESPEC SU-240). The experimental setup is shown in Figure 4.7.

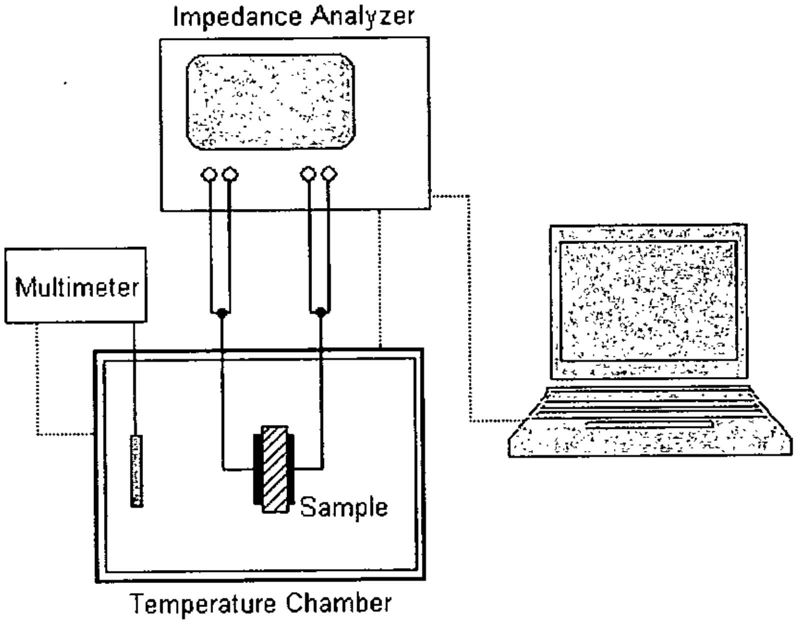

Figure 4.7 Schematic diagram of the experimental setup for dielectric permittivity measurement.

The dielectric properties of materials may change after poling. Therefore, the relative permittivity and dielectric loss of TGS/P(VDF-TrFE) 0-3 composites before and after the poling process (described in Section 4.2.1) were studied as a function of frequency from 1 kHz to 10 MHz at room temperature using an impedance analyzer (HP4294A).

4.3.3 Results and Discussion

4.3.3.1 Dielectric Properties as a Function of Temperature

Figure 4.8 shows the temperature dependence of the relative permittivity $\varepsilon_r^{'}$ and dielectric loss factor *tanδ* along the polar axis (b-axis) of the unpoled TGS single crystal from -20 °C to 120 °C. The relative permittivity shows a peak in the vicinity of 50 °C which is associated with the ferroelectric-paraelectric phase transition of TGS (at 49 °C). The $\varepsilon_r^{'}$ of TGS does not vary with frequency above the transition, but shows a slight frequency dependence below the Curie temperature. The dielectric loss factor of TGS also shows a peak near the Curie point and displays a relaxation process in the vicinity of 0 °C.

The relative permittivity $\varepsilon_r^{'}$ and dielectric loss *tanδ* of P(VDF-TrFE) copolymer as a function of temperature from -20 °C to 120 °C were measured upon heating and cooling as shown in Figure 4.9. In the $\varepsilon_r^{'}$ curves, a thermal hysteresis is observed: the ferroelectric-paraelectric phase transition of P(VDF-TrFE) appears at about 105 °C and 70 °C upon heating and cooling, respectively. In the *tanδ* curves, a non-crystalline β relaxation is observed around -20 °C at 1 kHz and it shifts to higher temperature with increasing frequency.

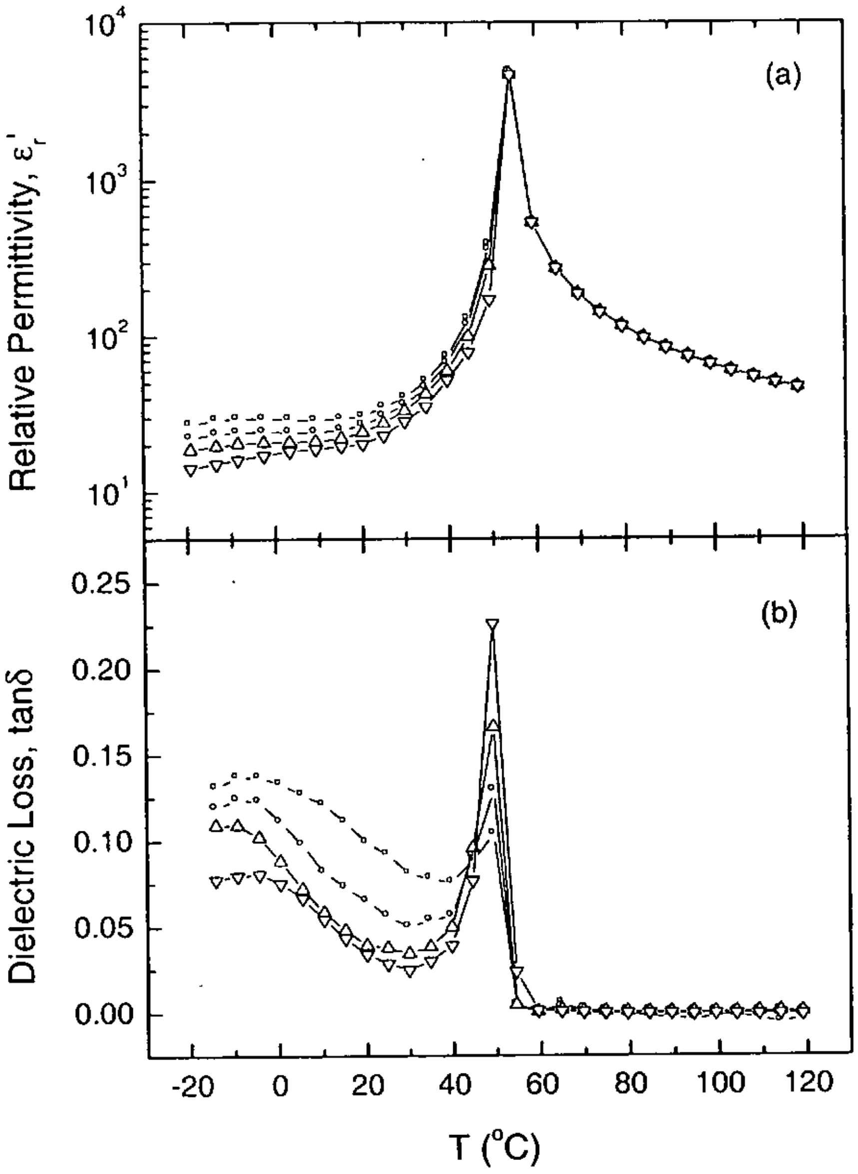

Figure 4.8 Relative permittivity (a) and dielectric loss factor (b) as a function of temperature for TGS single crystal measured at 1 kHz (square), 10 kHz (circle), 100 kHz (triangle) and 1 MHz (inverted triangle).

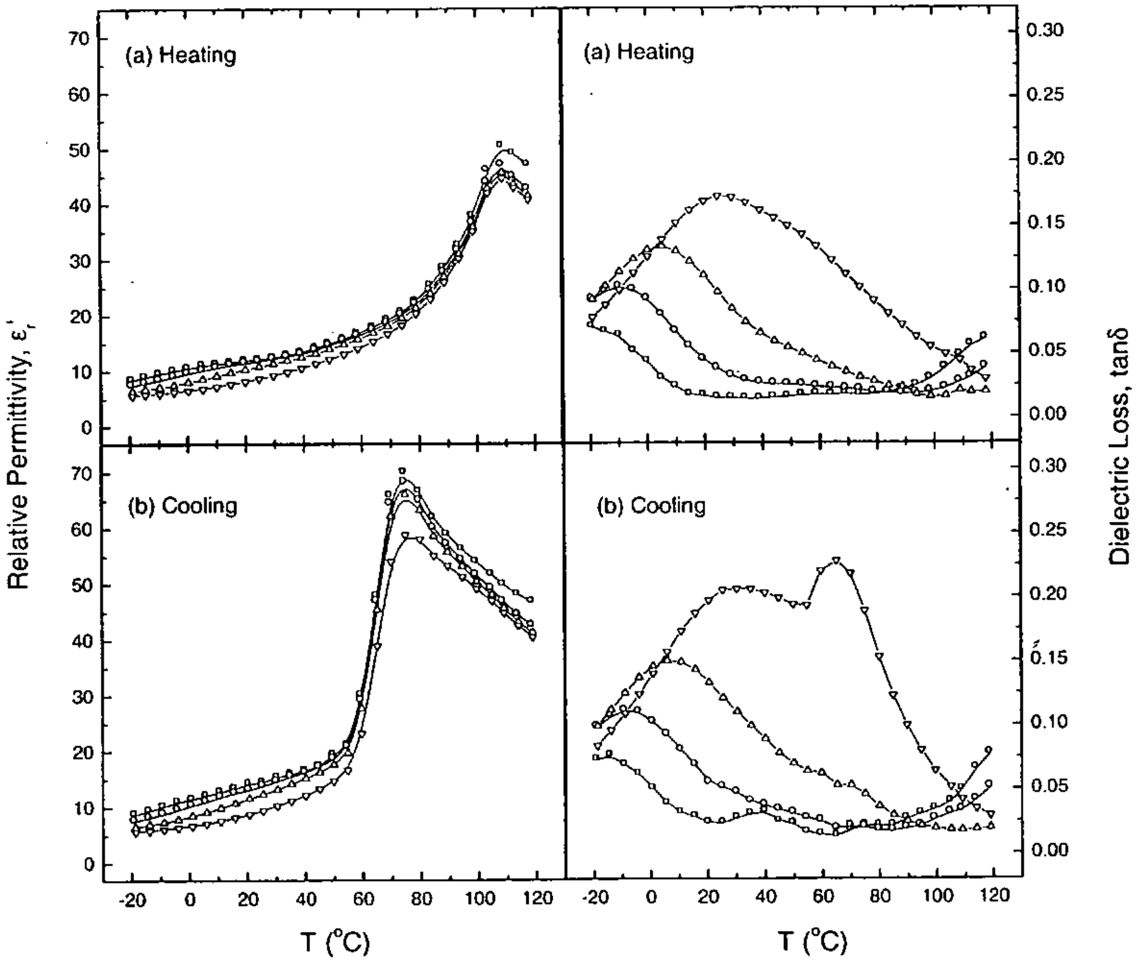

Figure 4.9 Relative permittivity and dielectric loss factor as a function of temperature for P(VDF-TrFE) copolymer measured at 1 kHz (square), 10 kHz (circle), 100 kHz (triangle) and 1 MHz (inverted triangle) during (a) heating and (b) cooling process.

Figure 4.10 presents the relative permittivity of the 0-3 composites with various volume percent of TGS ϕ as a function of temperature from -20 °C to 120 °C during the heating run measured at 10 kHz. As comparison, the curves of pure P(VDF-TrFE) copolymer are also plotted in Figure 4.10. The phase transitions of TGS and P(VDF-TrFE) are both observed in the $\varepsilon_r^{'}$ curves of the composites. The transition peak of TGS becomes more and more obvious as the volume percent of TGS increases. At the same time, the peak intensity corresponding to the phase transition of P(VDF-TrFE) copolymer decreases with increasing ϕ . It should be noted that the transition temperatures for TGS and P(VDF-TrFE) determined in the dielectric behavior are close to the values obtained in the DSC thermograms presented in Chapter 3.

The temperature dependence of the dielectric loss *tanδ* of the composites is presented in Figure 4.11. A prominent β relaxation is observed in the *tanδ* data of the pure copolymer around -10 °C, which may be ascribed to the micro-Brownian motion of noncrystalline chain segments [Furukawa et al., 1981]. This non-crystalline β relaxation of the copolymer is also found in the *tanδ* data of the composites and the magnitude of the peak decreases gradually with increasing volume fraction of TGS. In addition, there is a sharp rise of *tanδ* above 90 °C in all samples. It is considered to be due to the Curie transition of the copolymer.

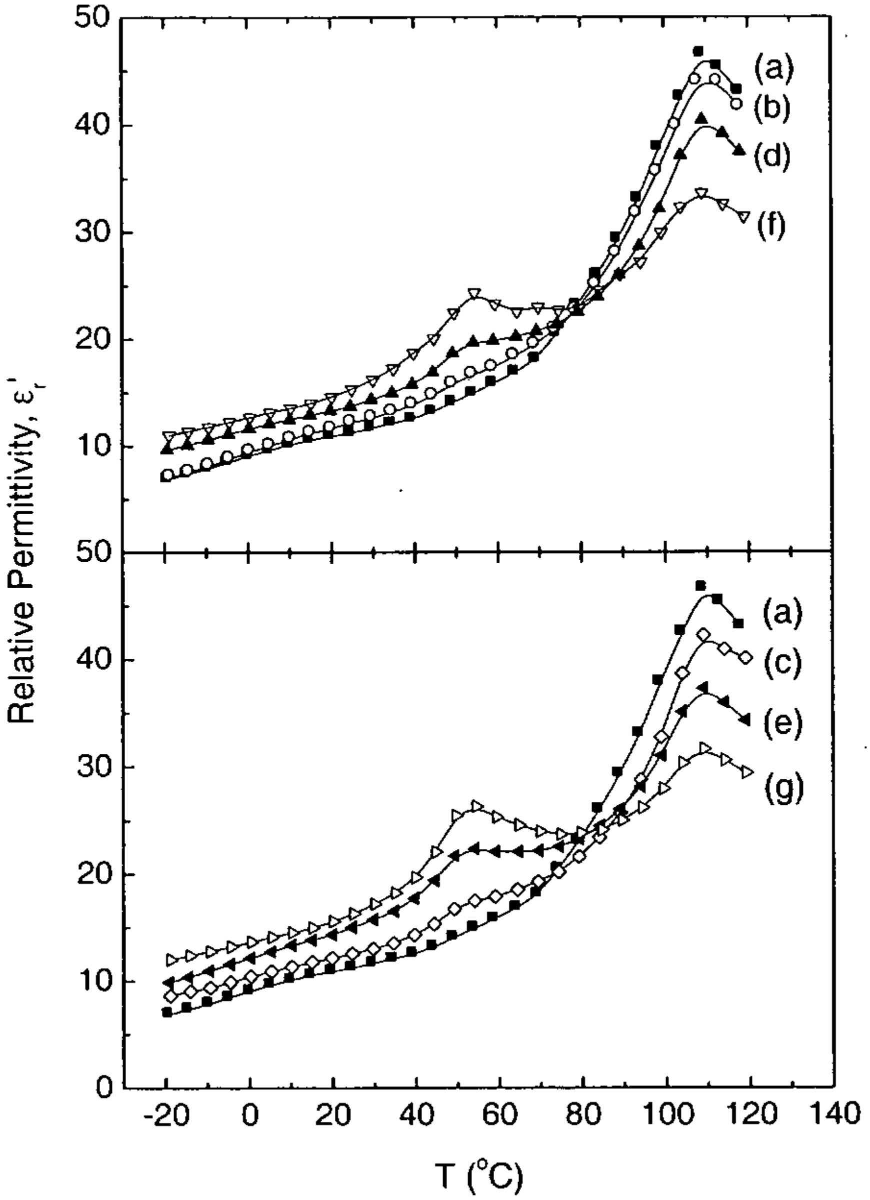

Figure 4.10 Relative permittivity as a function of temperature for TGS/P(VDF-TrFE) 0-3 composites with (a) 0 vol%, (b) 4.5 vol%, (c) 11.1 vol%, (d) 22.0 vol%, (e) 27.3 vol%, (f) 32.6 vol% and (g) 42.9 vol% of TGS measured at 10 kHz.

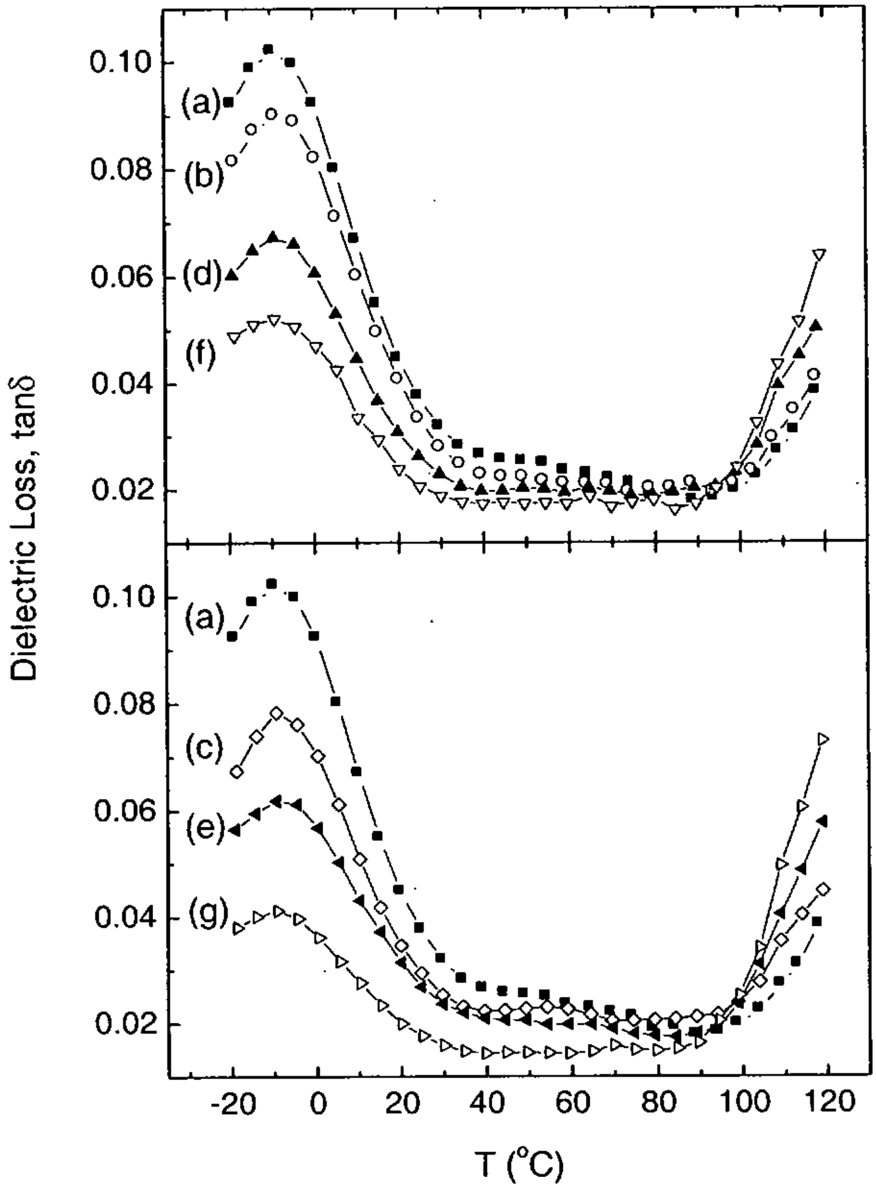

Figure 4.11 Dielectric loss factor as a function of temperature for TGS/P(VDF-TrFE) 0-3 composites with (a) 0 vol%, (b) 4.5 vol%, (c) 11.1 vol%, (d) 22.0 vol%, (e) 27.3 vol%, (f) 32.6 vol% and (g) 42.9 vol% of TGS measured at 10 kHz.

4.3.3.2 Dielectric Properties as a Function of Frequency

Figure 4.12 shows the relative permittivity $\varepsilon_r^{'}$ and dielectric loss $tan\delta$ of TGS single crystal before and after d.c. poling as a function of frequency from 1 kHz to 10 MHz at room temperature. Before poling, $\varepsilon_r^{'}$ and $tan\delta$ decrease significantly with increasing frequency (Figure 4.12 (a)). The frequency dependence of $\varepsilon_r^{'}$ and $tan\delta$ become much weaker after the poling process and the values are smaller (Figure 4.12 (b)) due to the dipole alignment.

The frequency dependence of $\varepsilon_r^{'}$ and $tan\delta$ of P(VDF-TrFE) copolymer before and after d.c. poling are presented in Figure 4.13. As the measuring frequency increases, $\varepsilon_r^{'}$ of the copolymer decreases and $tan\delta$ increases. The loss factor $tan\delta$ exhibits a relaxation peak at about 2 MHz, which is related to the β relaxation [Furukawa et al., 1984]. After poling, the frequency dependence of $\varepsilon_r^{'}$ and $tan\delta$ are similar to that before poling, but $\varepsilon_r^{'}$ and $tan\delta$ have lower values due to the dipole alignment (Figure 4.13 (b)).

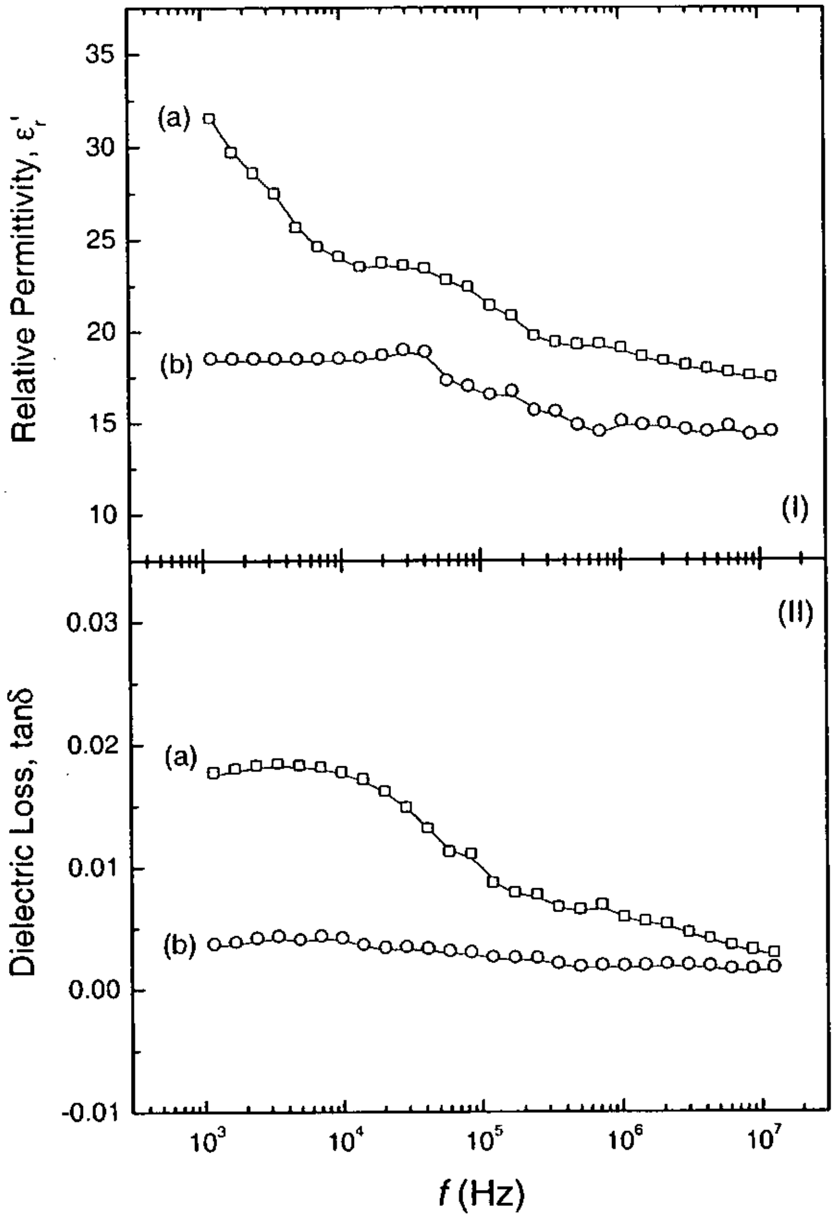

Figure 4.12 Relative permittivity (I) and dielectric loss factor (II) as a function of frequency for TGS single crystal (a) before and (b) after poling measured at room temperature.

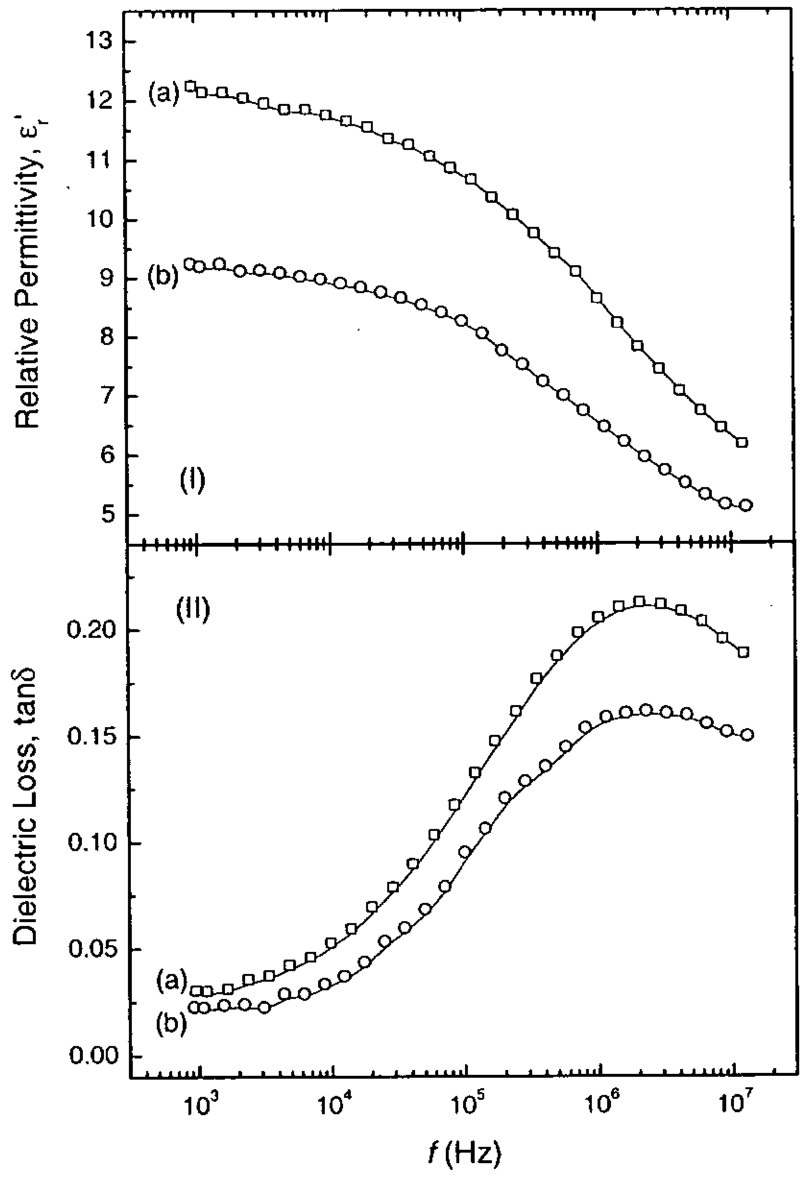

Figure 4.13 Relative permittivity (I) and dielectric loss factor (II) as a function of frequency for P(VDF-TrFE) copolymer (a) before and (b) after poling measured at room temperature.

Figure 4.14 shows the relative permittivity ε_r' and dielectric loss *tanδ* of the 0-3 composites as a function of frequency at room temperature. It is found that the dielectric behavior of the 0-3 composites is dominated by the behavior of the copolymer (ϕ = 0 vol%). In the composites, the TGS phase possesses higher relative permittivity than the P(VDF-TrFE) phase, therefore ε_r' increases with increasing ϕ. In the case of dielectric loss, the peak related to the β relaxation of the copolymer is suppressed as the volume fraction of TGS increases.

Figure 4.15 and Figure 4.16 show the dielectric properties of the 0-3 composites as a function of frequency with only the TGS phase poled and with both two phases poled, respectively. The variation of ε_r' and *tanδ* in the poled composites with ϕ is similar to that for the unpoled samples. The values of ε_r' and *tanδ* for the samples with two phases poled are lower than those for the samples with only TGS poled, which are in turn lower than those for the unpoled samples. The values of ε_r' and *tanδ* at 10 kHz for all the samples are tabulated in Table 4.2.

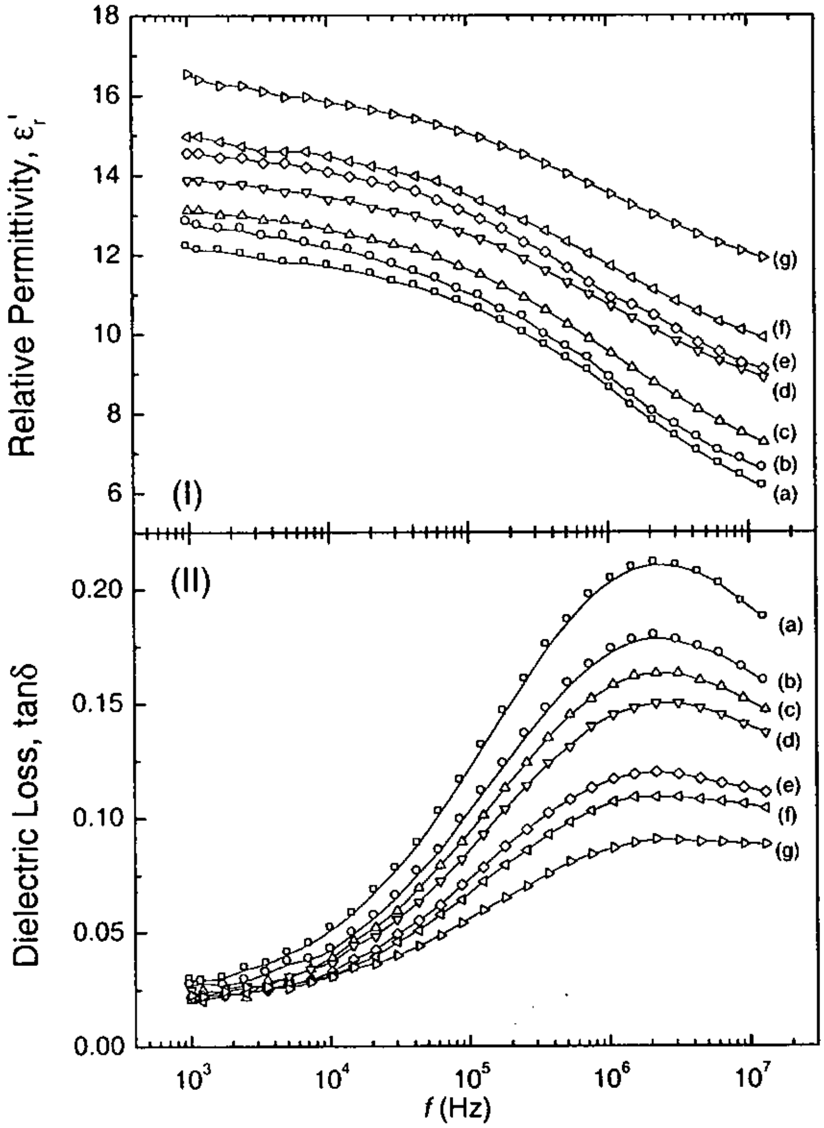

Figure 4.14 Relative permittivity (I) and dielectric loss factor (II) as a function of frequency for TGS/P(VDF-TrFE) 0-3 composites (unpoled) with (a) 0 vol%, (b) 4.5 vol%, (c) 11.1 vol%, (d) 22.0 vol%, (e) 27.3 vol%, (f) 32.6 vol% and (g) 42.9 vol% of TGS measured at room temperature.

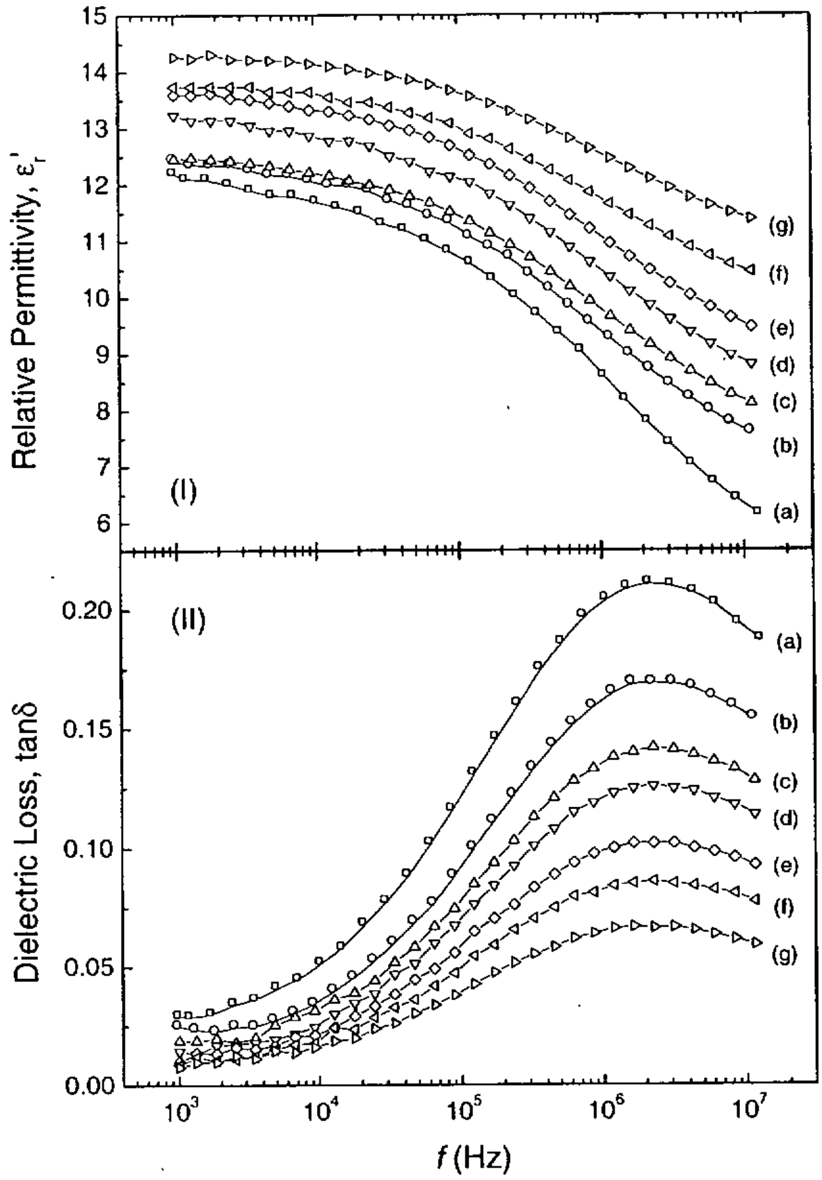

Figure 4.15 Relative permittivity (I) and dielectric loss factor (II) as a function of frequency for TGS/P(VDF-TrFE) 0-3 composites (only the TGS phase poled) with (a) 0 vol%, (b) 4.5 vol%, (c) 11.1 vol%, (d) 22.0 vol%, (e) 27.3 vol%, (f) 32.6 vol% and (g) 42.9 vol% of TGS measured at room temperature.

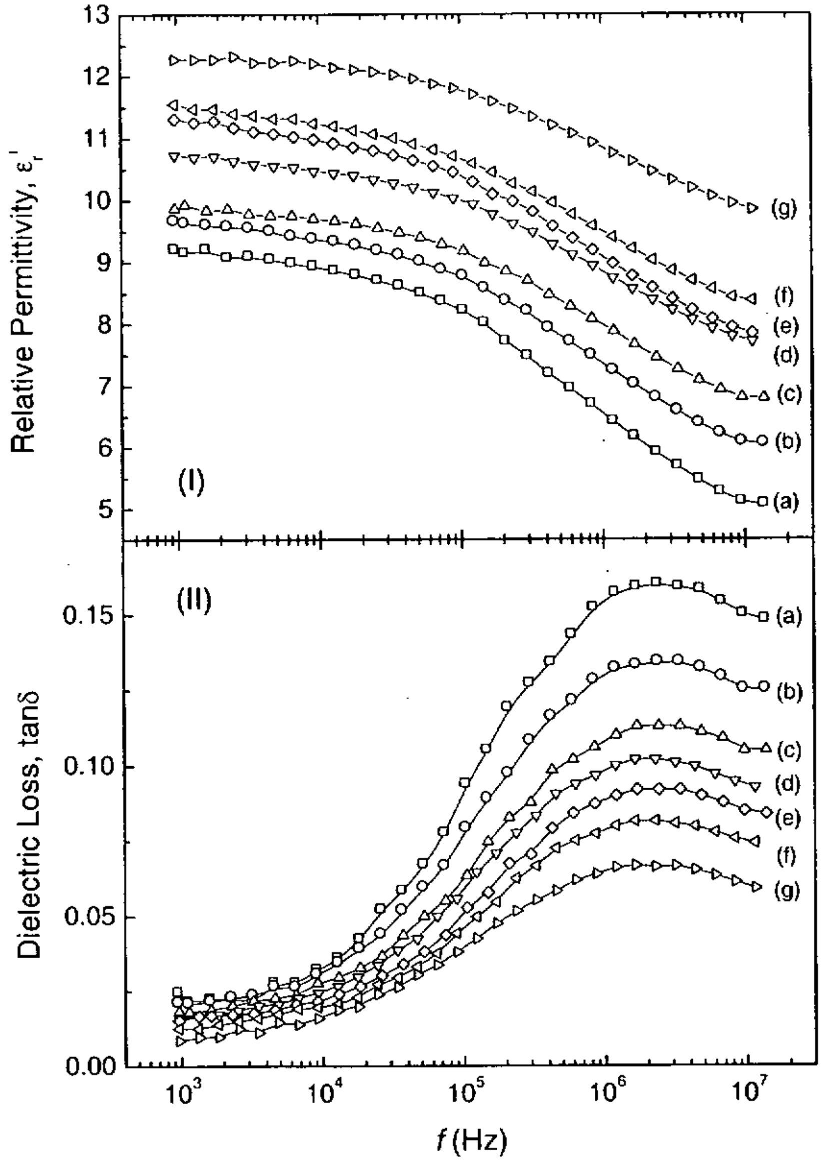

Figure 4.16 Relative permittivity (I) and dielectric loss factor (II) as a function of frequency for TGS/P(VDF-TrFE) 0-3 composites (two phases poled) with (a) 0 vol%, (b) 4.5 vol%, (c) 11.1 vol%, (d) 22.0 vol%, (e) 27.3 vol%, (f) 32.6 vol% and (g) 42.9 vol% of TGS measured at room temperature.

Table 4.2 Relative permittivity and dielectric loss factor at 10 kHz for P(VDF-TrFE), TGS single crystal and TGS/P(VDF-TrFE) 0-3 composites measured at room temperature.

Materials	*Unpoled*		*TGS Phase Poled*		*Two Phases Poled*	
	ε_r'	*tanδ*	ε_r'	*tanδ*	ε_r'	*tanδ*
P(VDF-TrFE)	12.1	0.051	12.1	0.051	8.98	0.032
4.5 vol%	12.22	0.042	12.23	0.034	9.12	0.030
11.1 vol%	12.63	0.039	12.41	0.032	9.48	0.028
22.0 vol%	13.39	0.037	12.70	0.025	10.05	0.024
27.3 vol%	14.08	0.033	13.04	0.021	10.43	0.021
32.6 vol%	14.47	0.031	13.22	0.018	10.75	0.018
42.9 vol%	15.27	0.031	13.51	0.016	11.44	0.015
TGS	23.30	0.013	18.56	0.004	18.56	0.004

4.3.3.3 Modelling of the Relative Permittivity of 0-3 Composites

Several models have been developed to analyze the dielectric permittivity of a binary system. The Maxwell-Wagner model [Wagner, 1914] is one of the best known models. In this model, spheres with permittivity ε_r' are assumed to be sparsely distributed in a continuous medium with permittivity ε_m'. In such a system, the radius of each sphere is much smaller than the distance between two spheres, hence each sphere may be assumed to be situated in an infinite matrix. The permittivity of the composites ε' is then given by:

$$\varepsilon' = \varepsilon_m' \cdot \frac{2\varepsilon_m' + \varepsilon_i' + 2\phi(\varepsilon_i' - \varepsilon_m')}{2\varepsilon_m' + \varepsilon_i' - \phi(\varepsilon_i' - \varepsilon_m')} \tag{4.10}$$

The Maxwell-Wagner model is only valid for low concentration of inclusions, because the interaction between the spheres has been neglected.

Another well-known model is the Bruggeman model which takes the effect of the immediate neighborhood of each sphere into account by the use of an integration scheme [Bruggeman, 1935]. In this scheme, the initially low concentration is gradually increased by infinitesimal addition of the dispersed inclusions. The permittivity of the medium around a sphere slowly changes from ε_m' to ε', the final permittivity of the system. The relative permittivity ε of the composites is then given by:

$$\left(\frac{\varepsilon_m'}{\varepsilon'}\right)^{1/3} = (1-\phi)\cdot\frac{\varepsilon_i' - \varepsilon_m'}{\varepsilon_i' - \varepsilon'} \tag{4.11}$$

The studies of 0-3 composites such as PZT/P(VDF-TrFE) [Chan et al., 1997], PT/P(VDF-TrFE) [Chen et al., 1998] and PCLT/P(VDF-TrFE) [Zhang et al., 1999] have shown that the Bruggeman model agrees quite well with the experimental results even for high concentration of inclusions.

In this project, the Bruggeman model was employed to analyze the ε_r' results (as shown in Table 4.2) of the TGS/P(VDF-TrFE) 0-3 composites. It should be noted that the observed relative permittivity of TGS single crystal cannot be used as the value for the relative permittivity of the inclusion ε_i', because it is measured along the b-axis while the TGS crystallites in the composites are randomly oriented. Therefore the data for the copolymer and composites were least squares fitted to the Bruggeman model. Figures 4.17 and 4.18 show the theoretical curves and experimental data for the unpoled samples (ε_i'=20.2), samples with only the TGS phase poled (ε_i'=15.5) and samples with both phases poled (ε_i'=15.3), respectively. The measured values of ε_b' for unpoled and poled TGS are 23.3 and 18.56 (see Table 4.2), respectively, which are slightly higher than the ε_i' values obtained from least squares fitting. From Figures 4.17 and 4.18, it can be seen that the theoretical values predicted by the Bruggeman model agree well with the experimental results.

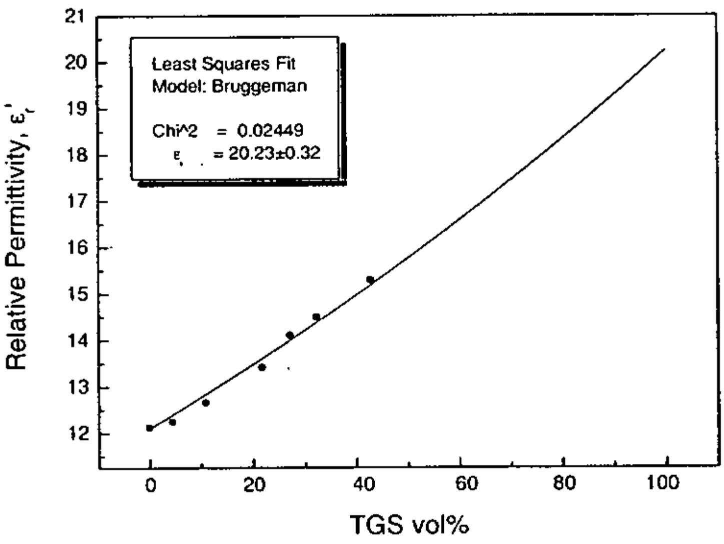

Figure 4.17 Relative permittivity as a function of ϕ for unpoled TGS/P(VDF-TrFE) 0-3 composites measured at room temperature and 10 kHz. The solid circles and the line represent the experimental data and Bruggeman model predictions, respectively.

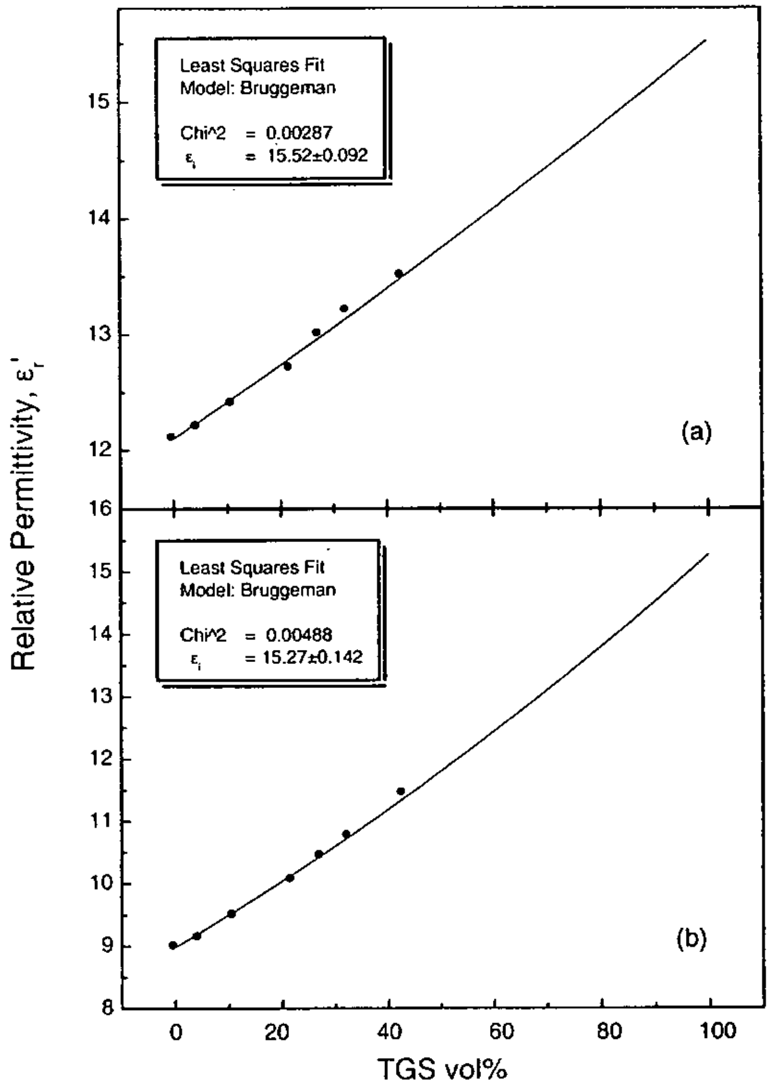

Figure 4.18 Relative permittivity as a function of ϕ for TGS/P(VDF-TrFE) 0-3 composites with (a) only the TGS phase poled and (b) two phases poled measured at room temperature and 10 kHz. The solid circles and lines represent the experimental data and Bruggeman model predictions, respectively.

4.4 Piezoelectric Properties of TGS/P(VDF-TrFE) 0-3 Composites

As mentioned before, piezoelectric activities will be elicited in TGS/P(VDF-TrFE) 0-3 composites after the poling process. The direct piezoelectric effect is the generation of electric displacement in a dielectric when the dielectric is subjected to a mechanical stress. The piezoelectric coefficient d is given by:

$$d = \left(\frac{\partial D}{\partial X} \right)_{T,E} \tag{4.12}$$

The converse piezoelectric effect is the generation of strain in a dielectric when the dielectric is subjected to an applied electric field. The piezoelectric coefficient $\bar{d}$ is given by:

$$\bar{d} = \left(\frac{\partial x}{\partial E} \right)_{T,X} \tag{4.13}$$

where D, E, X, x and T denote electric displacement, electric field, stress, strain and temperature, respectively. It is noted that $d = \bar{d}$, The piezoelectric coefficient is usually expressed in units of coulomb/newton (C/N) or meter/volt (m/V).

In the present work,.the d_{33} value was measured using a piezo d_{33} meter (Model ZJ-3D, Institute of Acoustics, Academia Sinica). The schematic diagram is shown in Figure 4.19 and the measurement is based on the following principle. A force of 0.25 N and oscillating at a frequency of 110 Hz is applied on the electroded surfaces of the sample by two vertical probes which also serve as electrical connections. A standard piezoelectric ceramic element (lead zirconate titanate, PZT) is connected in series with

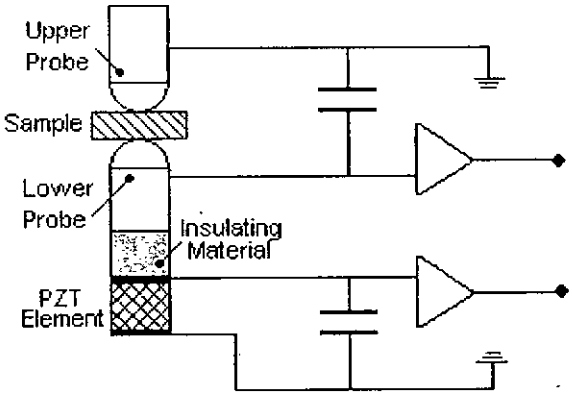

Figure 4.19 Schematic diagram of a piezo d_{33} meter.

the sample. The sample and the standard PZT element are subjected to the same force and the piezoelectric charge induced in each of them is collected on a parallel plate capacitor. The output voltages from the two capacitors are measured and then used to provide a direct readout of the d_{33} value of the sample.

Figure 4.20 and Table 4.3 show the piezoelectric coefficient d_{33} of the composites with only the TGS phase poled and the composites with two phases poled measured at room temperature. For the composites with only the TGS phase poled, the value of d_{33} is relatively low at 4.5 vol% of TGS and it increases with increasing ϕ. It should be noted that piezoelectric coefficients of P(VDF-TrFE) and TGS single crystal (along the b-axis) are -26.3 pC/N and 40 pC/N, respectively, i.e. they have opposite sign. For the composites with two phases poled, d_{33} has large and negative values at low volume percent of TGS. As ϕ increases, d_{33} is reduced in magnitude and becomes nearly zero at 42.9 vol% of TGS.

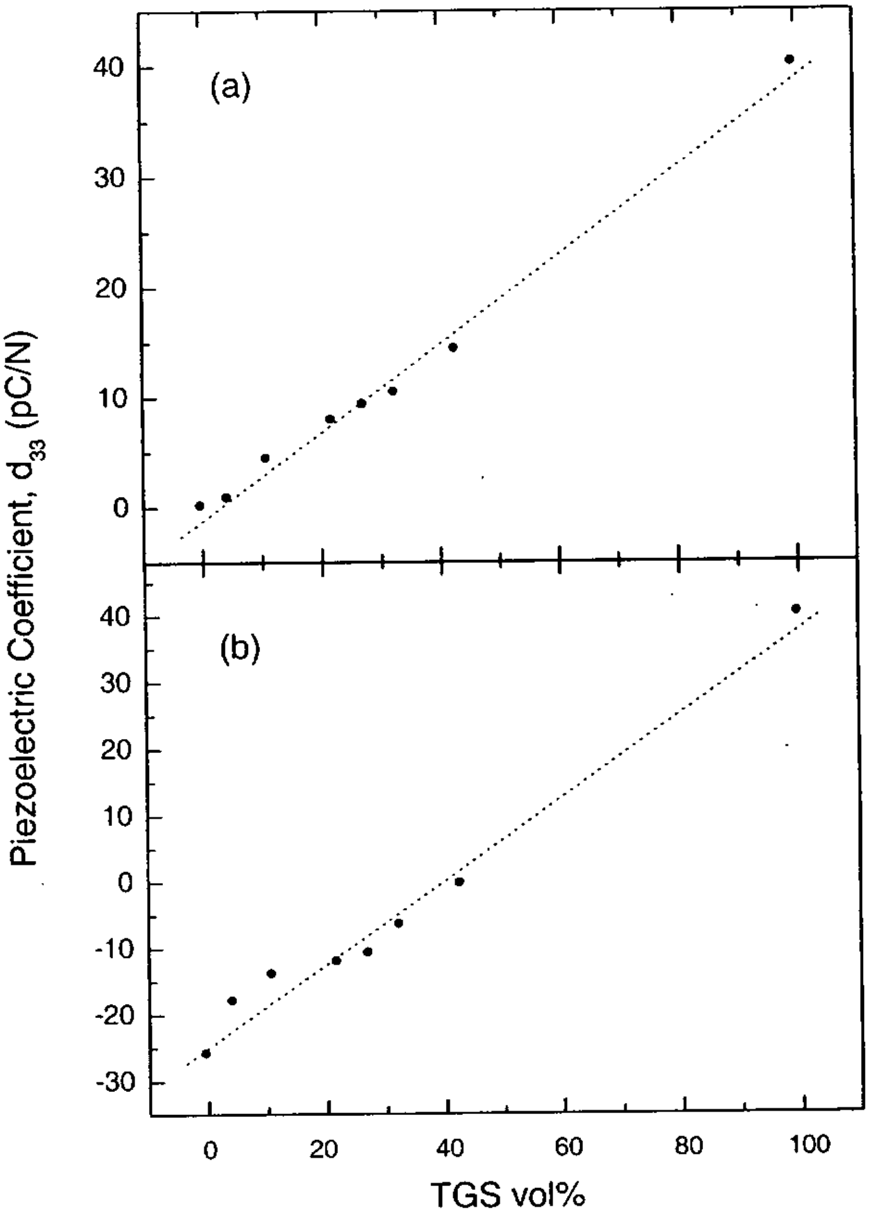

Figure 4.20 Piezoelectric coefficient as a function of ϕ for TGS/P(VDF-TrFE) 0-3 composites with (a) only the TGS phase poled and (b) two phases poled measured at room temperature.

Table 4.3 Piezoelectric coefficients for P(VDF-TrFE), TGS single crystal and TGS/P(VDF-TrFE) 0-3 composites measured at room temperature.

Materials	d_{33} *(pC/N)* *(TGS poled only)*	d_{33} *(pC/N)* *(Two phases poled)*
P(VDF-TrFE)	0	-26.2
4.5 vol%	0.7	-18.2
11.1 vol%	4.3	-14.2
22.0 vol%	7.8	-12.3
27.3 vol%	9.2	-11.0
32.6 vol%	10.3	-6.7
42.9 vol%	14.2	-0.5
TGS	40.0	40.0

4.5 Pyroelectric Properties of TGS/P(VDF-TrFE) 0-3 Composites

4.5.1 Introduction

The pyroelectric effect refers to the phenomenon in which the degree of polarization changes with the variation of temperature. At equilibrium the depolarization field due to the polarization discontinuity at the surfaces of a pyroelectric crystal is neutralized by free charges [Lines et al., 1977]. When the temperature is changed, the spontaneous polarization changes so that an excess of free charge appears on one of the polar faces of the crystal. Connected with an external circuit, there will be a current flow in the crystal and the circuit. The sign of the current depends on the direction of the polarization change. In most ferroelectrics, the pyroelectric coefficient is negative since the polarization generally decreases with increasing temperature. The magnitude of pyroelectric effect is characterized by the pyroelectric coefficient p which is defined as:

$$p = \frac{\partial P}{\partial T} \tag{4.14}$$

If the stress and electric field applied on the pyroelectric crystal are constant (or zero), the pyroelectric coefficient is given by:

$$p = \left(\frac{\partial D}{\partial T} \right)_{X,E} \tag{4.15}$$

In fact, the pyroelectric coefficient can be divided into clamped coefficient and unclamped coefficient. When the crystal is clamped (strain is constant), the pyroelectric effect directly comes from the change of polarization caused by the variation of temperature and is called the primary pyroelectric effect. When the crystal is unclamped (stress is constant), thermal expansion can also lead to a change of the degree of polarization through the piezoelectric effect. The pyroelectric effect caused by thermal expansion is called the secondary pyroelectric effect. Practically, the measured effective pyroelectric coefficient is the sum of the primary coefficient and a fraction of the secondary coefficient, since complete clamping is quite difficult.

4.5.2 Experimental Techniques

Several methods have been developed to measure the pyroelectric coefficient, such as the charge integration method [Glass, 1969], quasi-static direct method [Byer et al., 1972] and a series of dynamic methods [Chynoweth, 1960; Hartley et al., 1972; Garn et al., 1982; Dias et al., 1992]. The dynamic method, based on a sinusoidal modulation of temperature [Dias et al., 1992; Ploss B et al., 2000], was employed to measure the pyroelectric coefficient of the 0-3 composites. In this method the irreversible current due to space charge relaxation can be removed from the true reversible pyroelectric current, therefore it is especially suitable for the measurement of the pyroelectric coefficient of polymeric materials. The measurement principle is described in detail as follows. Based on Equation 4.15, the pyroelectric coefficient can be written as:

$$p = \frac{\partial D}{\partial T} = \frac{1}{A} \cdot \frac{\partial Q}{\partial T} = \frac{1}{A} \cdot \frac{\partial Q}{\partial t} \cdot \frac{\partial t}{\partial T} \qquad (4.16)$$

where $\partial Q / \partial t$ is the pyroelectric current and $\partial T / \partial t$ represents the heating rate. In the dynamic method, the sample temperature is sinusoidally modulated as $T(t)=\mathrm{Re}(T_{\sim}e^{i\omega t})$ and hence the pyroelectric current is also modulated as $I(t)=\mathrm{Re}(I_{\sim}e^{i\omega t})$, where $\omega = 2\pi f$. Then the pyroelectric coefficient is given by:

$$p=\frac{1}{A}\cdot I_{\sim}e^{i\omega t}\cdot\frac{dt}{d(T_{\sim}e^{i\omega t})}=\frac{1}{A}\cdot\frac{I_{\sim}}{i\omega T_{\sim}} \tag{4.17}$$

The appearance of i implies that the pyroelectric current signal is 90° out of phase with respect to the temperature modulation. In our experiment, the sample temperature was modulated at a frequency f = 5 mHz and with an amplitude $T_{\sim}$=1K using a Peltier element [Sharp et al., 1982]. The current signal was amplified with an electrometer and then the 90° out of phase signal was measured with a lock-in amplifier. The schematic diagram of the experimental setup is shown in Figure 4.21.

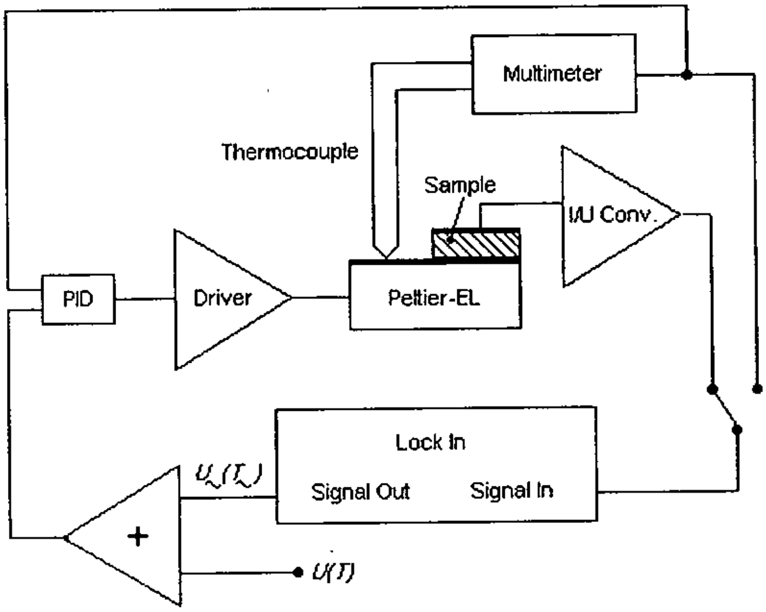

Figure 4.21 Experimental setup for the dynamic measurement of pyroelectric coefficient.

4.5.3 Results and Discussion

4.5.3.1 Pyroelectric Coefficients of the 0-3 Composites

Figure 4.22 shows the pyroelectric coefficients of the 0-3 composites with only the TGS phase poled as a function of temperature from room temperature to 60 °C (above T_c of TGS). As comparison, the results of pure copolymer and TGS single crystal are also plotted in Figure 4.22. The pyroelectric coefficient of the copolymer is nearly zero since the copolymer is not poled. The pyroelectric coefficient of the composites increases in magnitude with increasing volume percent of TGS. At any volume percent of TGS, the pyroelectric coefficient of the composites increases in magnitude with increasing temperature and reaches a maximum at about 50 °C. Above the Curie transition (T_c ~50 °C) of TGS, the magnitude of $-p$ decreases drastically because of the depolarization of TGS. Figure 4.23 shows the results for the composites with both phases poled. The pyroelectric coefficient shows a similar temperature dependence as that of the samples with only the TGS phase poled. However, the magnitude is enhanced due to the contribution of the poled copolymer phase.

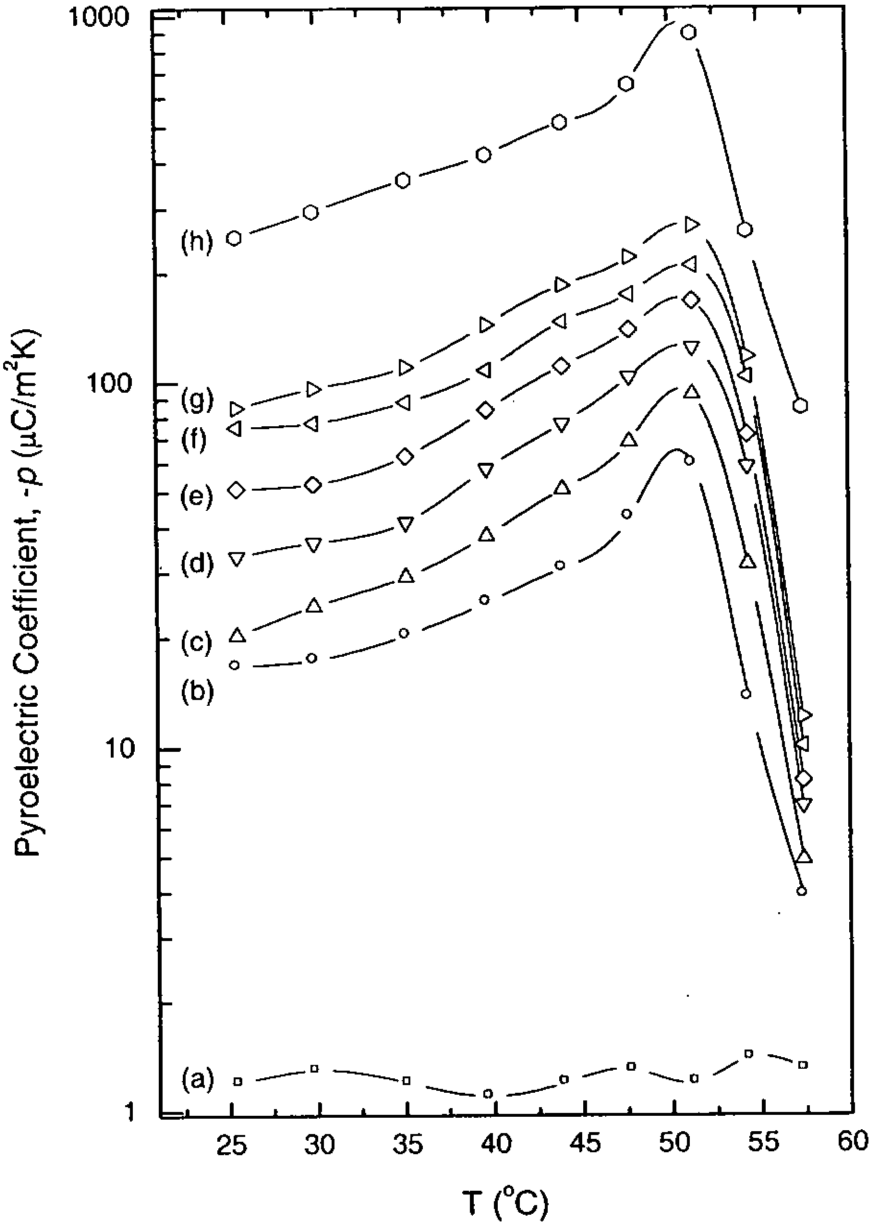

Figure 4.22 Pyroelectric coefficient as a function of temperature for TGS/P(VDF-TrFE) 0-3 composites (only the TGS phase poled) with (a) 0 vol%, (b) 4.5 vol%, (c) 11.1 vol%, (d) 22.0 vol%, (e) 27.3 vol%, (f) 32.6 vol% and (g) 42.9 vol% of TGS, and (h) TGS single crystal.

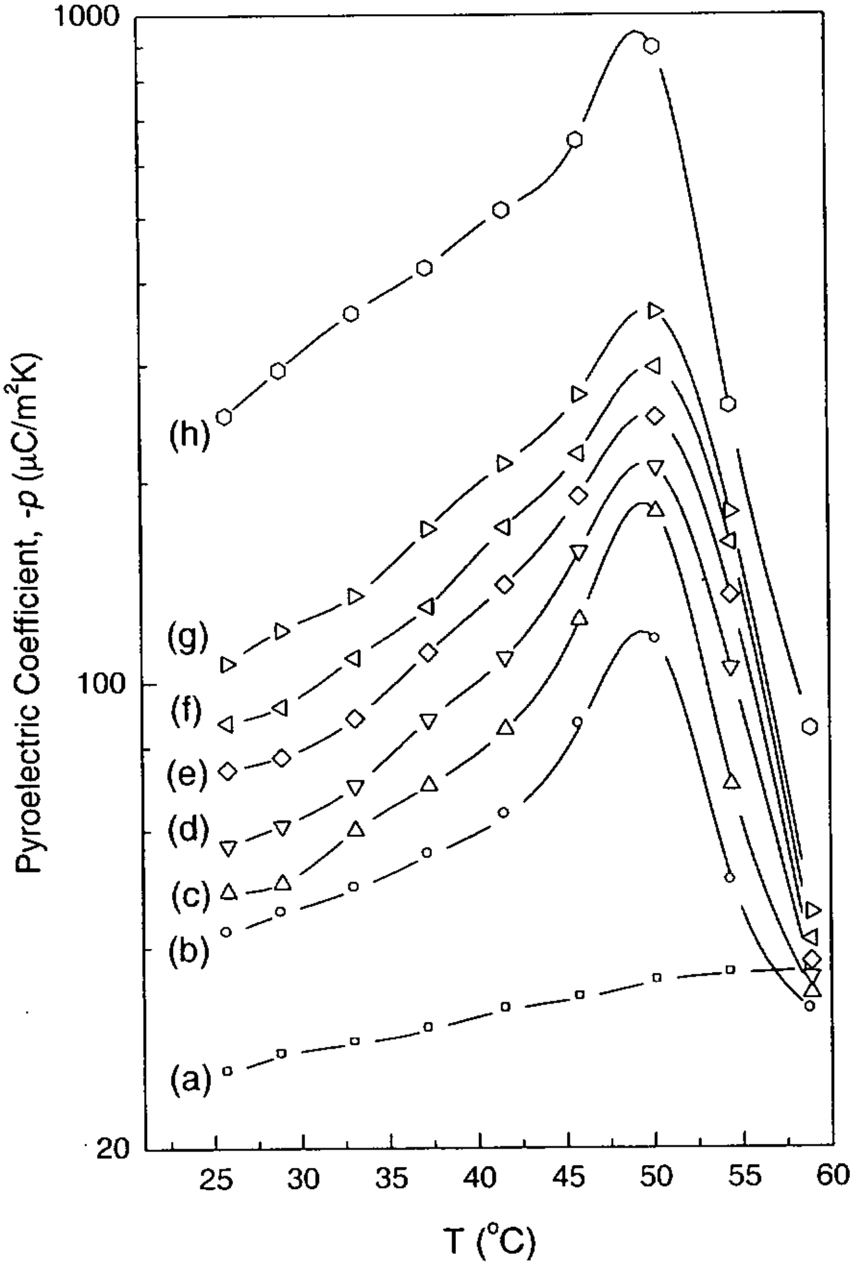

Figure 4.23 Pyroelectric coefficient as a function of temperature for TGS/P(VDF-TrFE) 0-3 composites (two phases poled) with (a) 0 vol%, (b) 4.5 vol%, (c) 11.1 vol%, (d) 22.0 vol%, (e) 27.3 vol%, (f) 32.6 vol% and (g) 42.9 vol% of TGS, and (h) TGS single crystal.

4.5.3.2 Modelling of the Pyroelectric Coefficients

There are several models describing the pyroelectric coefficient of composites consisting of pyroelectric inclusions in a pyroelectric matrix. Yamazaki et al. [1981] derived the pyroelectric coefficient of 0-3 composites with identical spherical ferroelectric particles. Based on a modified Clausius-Mossotti relation, Wang et al. [1993] calculated the pyroelectric coefficient of ferroelectric composites by taking into account the depolarization coefficient. For composites containing high volume fractions of inclusions or inclusions with size large compared to the sample thickness, 1-3 connectivity is expected to come into play, to complicate the original 0-3 geometry associated with low inclusion fractions. A cube model was proposed by Dias et al. [1996] to treat this case of mixed connectivity. Recently, Levin et al. [2001] have derived expressions for the effective pyroelectric constants of composite materials with spherical inclusions by means of effective field theory.

Considering the case that the difference in the polarizations of the two phases is completely compensated by charges at the matrix-inclusion interfaces, an effective-medium (EM) approach has been developed to treat 0-3 pyroelectric composites in the concentrated suspension limit [Ploss et al., 2000; Chew et al., 2003]. The effective pyroelectric coefficient p of the composites is given by:

$$p = \left(\frac{\varepsilon' - \varepsilon_m'}{\varepsilon_i' - \varepsilon_m'} \right) \cdot p_i + \left(\frac{\varepsilon_i' - \varepsilon'}{\varepsilon_i' - \varepsilon_m'} \right) \cdot p_m \qquad (4.18)$$

where the subscripts i and m represent inclusions and the matrix, respectively. We will use this equation to obtain theoretical values for comparison with our measurements.

Figure 4.24 shows the experimental results of the pyroelectric coefficients for composites with only the TGS phase poled and composites with two phases poled as a function of ϕ measured at room temperature. The theoretical curves are obtained by least squares fitting of the data for the copolymer and composite samples to Equation 4.18. In the calculation, ε_m' and p_m' are measured values and ε' and ε_i' have been obtained previously in Section 4.3.3.3 using the Bruggeman model. It is seen that the experimental data and the theoretical calculation are in good agreement. It is noted that by using least squares fitting, the pyroelectric coefficients of TGS for the two types of composites are found to be 206 μC/m^{2}K and 219 μC/m^{2}K, respectively, while the value measured using the large TGS single crystal sample is 251 μC/m^{2}K.

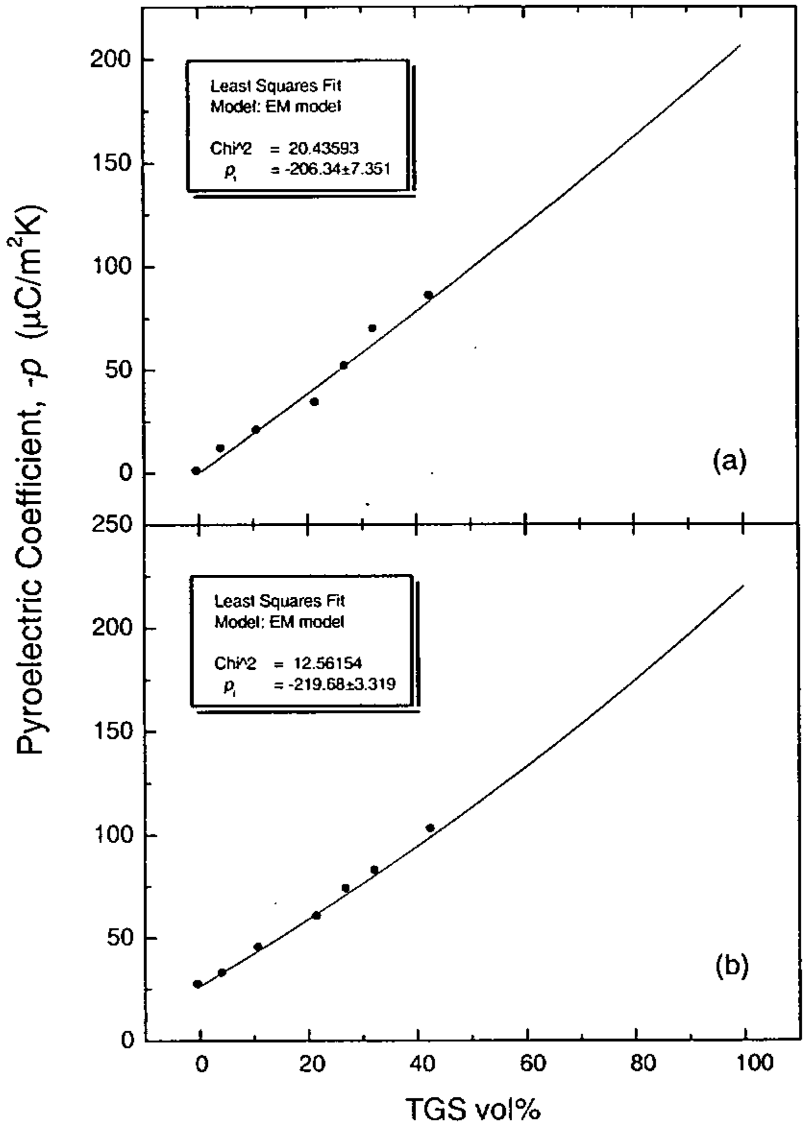

Figure 4.24 Pyroelectric coefficient as a function of ϕ for TGS/P(VDF-TrFE) 0-3 composites with (a) only the TGS phase poled and (b) two phases poled measured at room temperature. The solid circles and the lines represent the experimental data and EM model predictions, respectively.

4.5.3.3 Figures of Merit

Figures of merit (FOM) are used to describe the contribution of various physical properties of the material to the performance of a pyroelectric sensor. The current FOM F_i, voltage FOM F_V and detectivity FOM F_D are given by:

$$F_i = \frac{p}{C_p^{vol.}}; \quad F_V = \frac{p}{C_p^{vol.}\varepsilon_r^{'}\varepsilon_o}; \quad F_D = \frac{p}{C_p^{vol.}(\varepsilon_r^{'}\varepsilon_o \tan\delta)^{1/2}} \tag{4.19}$$

where $C_p^{vol.}$ is the heat capacity per unit volume (as described and measured in Chapter 3). F_i and F_V describe the influence of the pyroelectric material on the current and voltage responsivity of a pyroelectric sensor. F_D is related to the specific detectivity D^*.

The figures of merit for composites with TGS phase poled and composites with two phases poled are calculated using the measured p, C_p, $\varepsilon_r^{'}$ (at 1 kHz) and $\tan\delta$ (at 1 kHz) at room temperature. The results are tabulated in Tables 4.4 and 4.5. The FOM are also plotted in Figure 4.25 (with only the TGS phase poled) and Figure 4.26 (both two phases poled). Compared to the values for the copolymer all three FOM are improved in the composites, and the FOM values increase steadily with increasing ϕ. For the composite with 42.9 vol% TGS and with both phases poled, F_i and F_D have reached about 40% while F_V has reached about 60% of the values for TGS single crystal.

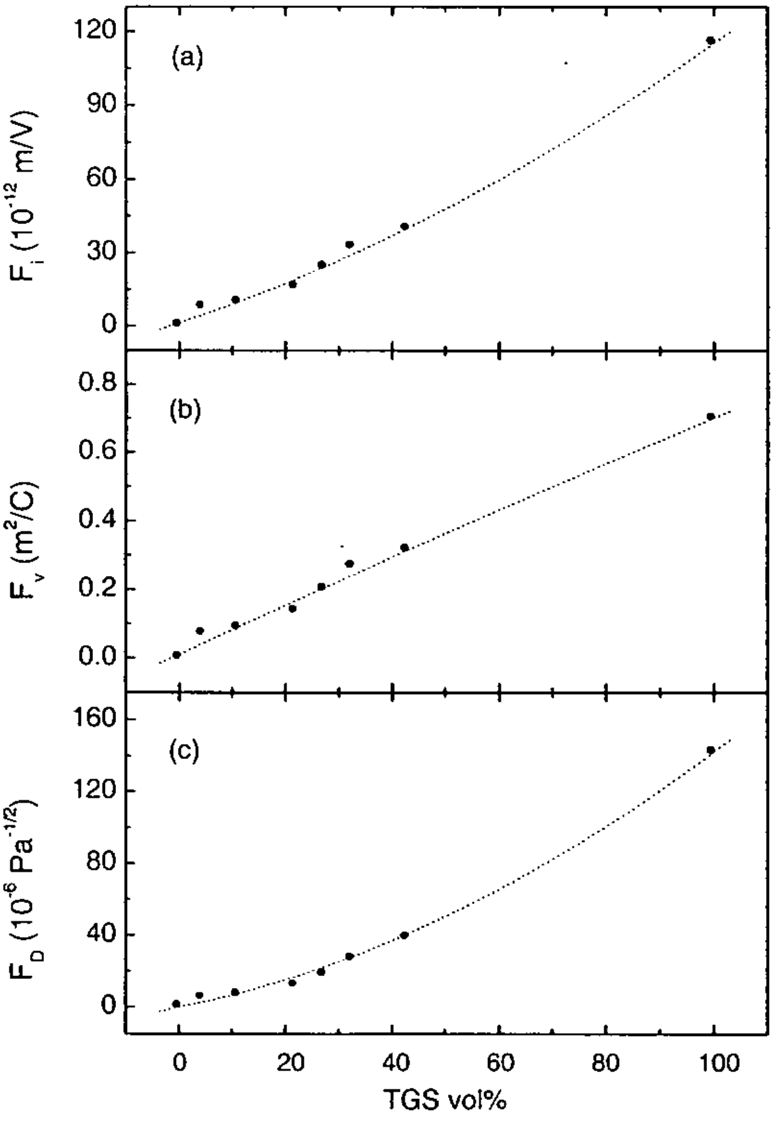

Figure 4.25 Figures of merit F_i, F_V and F_D for TGS/P(VDF-TrFE) 0-3 composites with only the TGS phase poled.

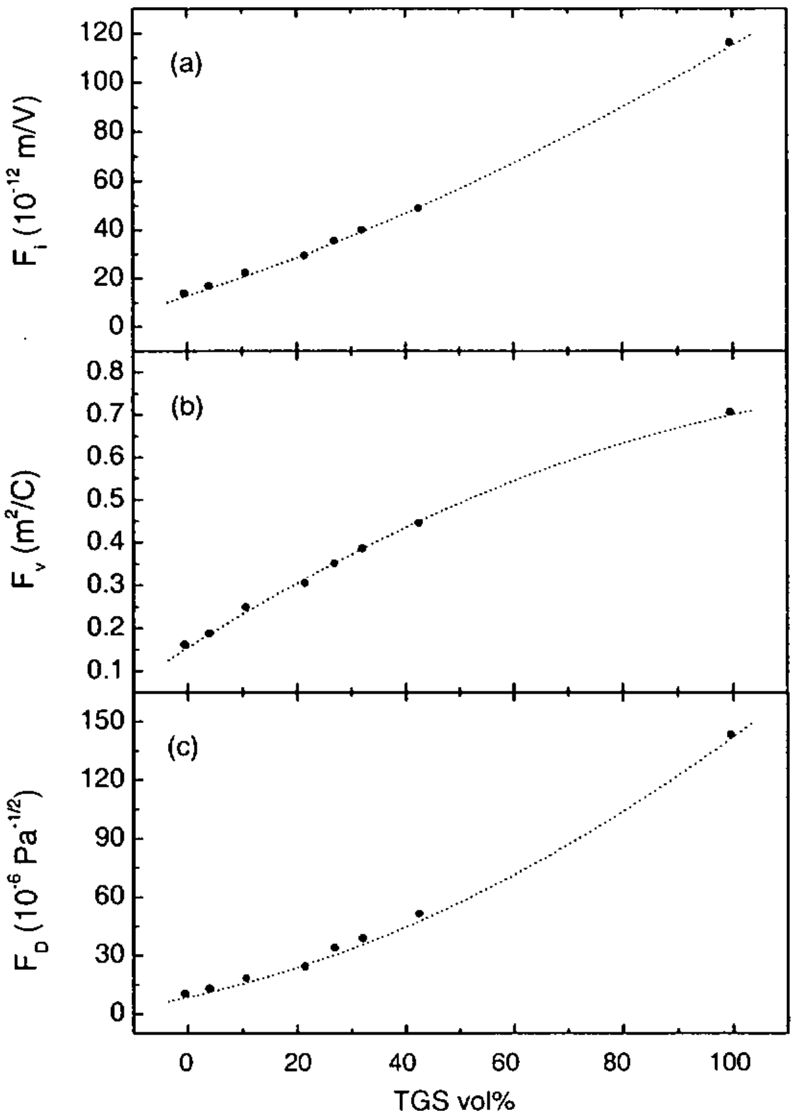

Figure 4.26 Figures of merit F_i, F_V and F_D for TGS/P(VDF-TrFE) 0-3 composites with two phases poled.

Table 4.4 Pyroelectric properties of TGS/P(VDF-TrFE) 0-3 composites with only the TGS phase poled.

Materials	$C_p^{vol.}$ $(MJ/m^3 \cdot K)$	ε_r' (1kHz)	tanδ (1kHZ)	-p $(\mu C/m^2K)$	F_i $(10^{-12}m/V)$	F_V (m^2/C)	F_D $(10^{-6}Pa^{-1/2})$
P(VDF-TrFE)	2.09	12.20	0.029	---	---	---	---
4.5 vol%	2.08	12.44	0.025	11.2	7.69	0.07	4.66
11.1 vol%	2.10	12.46	0.019	20.3	9.52	0.09	6.63
22.0 vol%	2.10	13.24	0.016	33.4	15.9	0.14	11.8
27.3 vol%	2.12	13.60	0.015	51.2	24.1	0.20	18.0
32.6 vol%	2.13	13.74	0.012	69.4	32.4	0.27	26.7
42.9 vol%	2.14	14.26	0.009	85.2	39.7	0.31	38.3
TGS	2.18	18.6	0.004	251	115.1	0.70	142

Table 4.5 Pyroelectric properties of TGS/P(VDF-TrFE) 0-3 composites with two phases poled.

Materials	$C_p^{vol.}$ ($MJ/m^3 \cdot K$)	ε_r' (1kHz)	$tan\delta$ (1kHZ)	$-p$ ($\mu C/m^2K$)	F_i ($10^{-12} m/V$)	F_V (m^2/C)	F_D ($10^{-6} Pa^{-1/2}$)
P(VDF-TrFE)	2.09	9.20	0.024	26.4	12.6	0.16	8.96
4.5 vol%	2.08	9.66	0.021	32.3	15.5	0.18	11.6
11.1 vol%	2.10	9.87	0.018	44.5	21.2	0.24	16.9
22.0 vol%	2.10	10.73	0.016	59.5	28.3	0.30	22.8
27.3 vol%	2.12	11.31	0.011	73.0	34.4	0.34	32.5
32.6 vol%	2.13	11.55	0.010	82.6	38.8	0.38	37.3
42.9 vol%	2.14	12.27	0.008	102	47.7	0.44	50.0
TGS	2.18	18.6	0.004	251	115	0.70	142

4.6 Summary

In this Chapter, the hysteresis behavior and the dielectric, piezoelectric and pyroelectric properties of TGS/P(VDF-TrFE) 0-3 composites with various volume percent of TGS were studied in detail. Firstly, the hysteresis loops of all the samples investigated (TGS single crystal, pure P(VDF-TrFE) and 0-3 composites) were measured using a modified Sawyer-Tower circuit. The procedures for poling the TGS and the copolymer phases were then determined. After the d.c. poling process, three series of samples were obtained: composites before poling (I), composites with only the TGS phase poled (II) and composites with both phases poled (III). The temperature dependence and frequency dependence of the relative permittivity and dielectric loss of all the samples were studied. The Bruggeman model was used to calculate the relative permittivity of the composites and good agreement between experimental results and theoretical curves was observed. The piezoelectric coefficients d_{33} and pyroelectric coefficients p of the poled composites (II, III) were studied. The experimental data showed that the pyroelectric contributions from the two phases reinforced while piezoelectric contributions partially canceled each other after the two phases were poled in the same direction. The observed pyroelectric coefficients were found to agree with the theoretical values calculated from the effective-medium model. Three figures of merit F_i, F_V and F_D were calculated using the experimental data and were found to increased as the volume percent of TGS increased. Therefore, TGS/P(VDF-TrFE) 0-3 composite is a good candidate to be used as the sensing element for pyroelectric devices.

Chapter 5

Studies of MMT/P(VDF-TrFE) 0-3 Nanocomposites

In this Chapter, montmorillonite (MMT)/P(VDF-TrFE) 0-3 nanocomposites with various weight percents of MMT embedded in a P(VDF-TrFE) matrix were fabricated. Na^+-MMT was first modified with cetyltrimethylammonium bromide (CTAB) before being incorporated into the P(VDF-TrFE) (80/20 mol%) copolymer. The nanocomposites were then fabricated using a polymer intercalation method. The composites were characterized by means of X-ray diffractometry and differential scanning calorimetry (DSC). The dielectric permittivity, polarization hysteresis, piezoelectric coefficient and pyroelectric coefficient were also measured.

5.1 Introduction to Layered Silicate/Polymer Nanocomposites

Nanocomposites based on organic polymer matrices and layered silicate mineral fillers have attracted considerable attention over the last decade. Layered silicate/polymer (LSP) nanocomposites possess several advantages including: (a) they are lighter in weight compared to conventional composites because high degrees of stiffness and strength can be realized with lower fraction of inorganic materials [Vaia et al., 1997]; (b) their mechanical properties are potentially superior to fiber-reinforced polymers because reinforcement from the inorganic layers will occur in two rather than in one dimension [Yano et al., 1993]; (c) they exhibit outstanding diffusional barriers without requiring a multilayered design [Messersmith et al., 1995]. The enhancement of material properties has been linked to the very high surface area of the layered silicate filler particles and the interfacial interaction between the polymer matrix and the filler. In addition to their potential applications, LSP nanocomposites are unique model systems to study the statics and dynamics of polymers in confined environments.

Montmorillonite, hectorite and saponite are the most commonly used layered silicates. As shown in Figure 5.1, MMT consists of an octahedral alumina sheet sandwiched between two tetrahedral silica sheets and exhibits a net negative charge on the lamellar surface which causes absorption of cations such as Na^+ or K^+. For a nanocomposite to be formed successfully, the mineral should disperse into separate layers and hence ion-exchange reactions with cationic surfactants (commonly alkyl ammonium or alkyl phosphonium cations) are necessary. The role of alkyl cations in the silicate is to lower

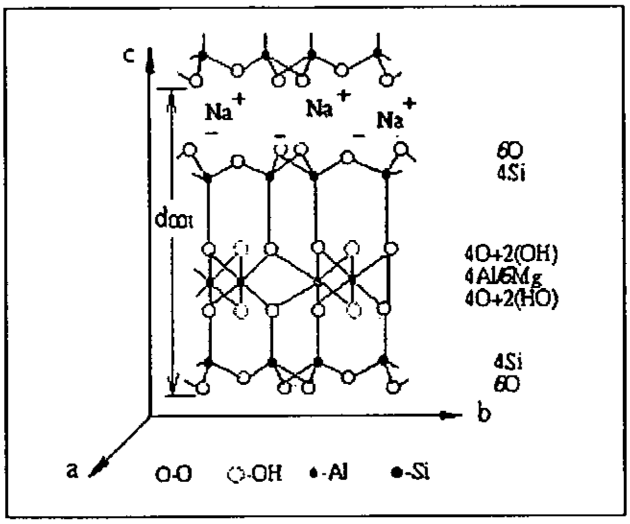

Figure 5.1 Schematic layered structure of montmorillonite. [Chen et al., 1999]

the surface energy of the inorganic host and improve the compatibility with the polymer. In addition, the alkyl cations could provide function groups that can react with the polymer or monomers to improve the interfacial strength [Krishnamoorti et al., 1996].

Layered silicate/polymer nanocomposites are prepared by a variety of routes. Traditional synthetic schemes involve intercalation of polymers either via intercalation of a suitable monomer followed by subsequent polymerization [Usuki et al., 1993] or via polymer intercalation from solution [Yano et al., 1993]. It have been recently demonstrated that LSP nanocomposites can be synthesized by direct melt intercalation even with high molecular weight polymers [Vaia et al., 1996]. This method avoids the use of organic solvents and permits the use of conventional processing techniques such as injection moulding and extrusion.

Polymer intercalation into layered inorganic solids is a versatile approach to synthesize organic-inorganic molecular hybrids or polymer nanocomposites. In general, two types of hybrids are possible: *intercalated*, in which a single extended polymer chain is intercalated between the host layers resulting in a well ordered multilayer with alternating polymer/inorganic layers and a repeat distance of a few nanometers, and *delaminated*, in which the silicate layers (~1 nm thick) are exfoliated and dispersed in a continuous polymer matrix [Giannelis, 1996]. The sketches of intercalated and delaminated PLS nanocomposites are shown in Figure 5.2.

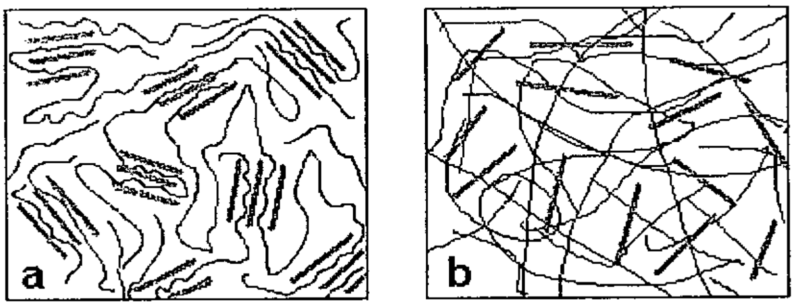

Figure 5.2 Sketches of (a) intercalated and (b) delaminated LSP nanocomposites.

Many studies have been carried out to characterize different nanocomposites. Techniques in use include wide-angle X-ray diffractometry (WAXD) and transmission electron microscopy (TEM). X-ray diffraction can be employed to monitor the position and intensity of the basal reflections from the silicate layers. TEM can provide information on morphology, spatial distribution and defect structures in real space, in a localized area. XRD and TEM are complementary techniques which can provide a complete study on LSP nanocomposites.

Until now, LSP nanocomposites have been formed with a wide variety of polymers including polypropylene [Li et al., 2003], polyamide [Davis et al., 2003], polystyrene [Vaia et al., 1996] and polymethylmethacrylate [Moussaif et al., 2003]. The mechanical and chemical properties of these LSP nanocomposites have been widely studied. The electrical conductivities of LSP nanocomposite with conductive polymer matrices such as polyaniline [Lu et al., 2002] and polypyrrole [Kim et al., 2003] have also attracted strong research interest. However, studies on LSP nanocomposites with ferroelectric polymer matrices have not been reported. In this project, MMT/P(VDF-TrFE) nanocomposites have been fabricated and their dielectric, ferroelectric, piezoelectric and pyroelectric properties are investigated.

5.2 Fabrication of MMT/P(VDF-TrFE) 0-3 Nanocomposites

The P(VDF-TrFE) 80/20 mol% copolymer used as the matrix was supplied by Piezotech, France. The Na^+-MMT clay (SWy-1) was supplied by University of Missouri Source Clay Repository, USA.

Organically modified MMT was prepared via a cation-exchange reaction which is a reaction between the sodium cations of MMT clay and alkyl ammonium ions of the intercalation agent. In our experiment, 5 g of Na^+-MMT clay was stirred in 200 ml deionized water at 60 °C for 2 h. A separate solution containing 3 g of intercalating agent cetyltrimethylammonium bromide (CTAB) in 100 ml of deionized water together with 1.0M hydrochloric acid aqueous solution (to adjust the pH value to 3-4) was stirred magnetically at the same time. The protonated amino acid solution was added to the MMT suspension and then the mixture was stirred overnight at 60 °C. The sample was washed and filtered repeatedly for at least three times to remove any excess ammonium ions. After drying, organic-MMT was obtained.

In our experiment, a polymer intercalation method was used to prepare the composites. Powder of P(VDF-TrFE) was dissolved in dimethylformamide (DMF) and then an amount of organic-MMT was dispersed into the solution with the aid of ultrasonic agitation. The suspension was well-stirred and then poured onto a glass sheet. After drying in a vacuum desiccator, the film was annealed at 120 °C for 12 h and then at 130 °C for 2 h to improve the crystallinity. Cr-Au electrodes were deposited on both sides of the 50 μm thick film for subsequent property measurements. MMT/P(VDF-TrFE) nanocomposites with 1 wt% and 4wt% of MMT were prepared. We have fabricated nanocomposites with higher wt% MMT but the conductivity of these samples was too high to be used as dielectrics.

5.3 Structural Analysis of MMT/P(VDF-TrFE) 0-3 Nanocomposites

The microstructure of the MMT/P(VDF-TrFE) nanocomposite was studied using a scanning electron microscope (JEOL JSM-6335F FE-SEM). Figure 5.3 shows the SEM

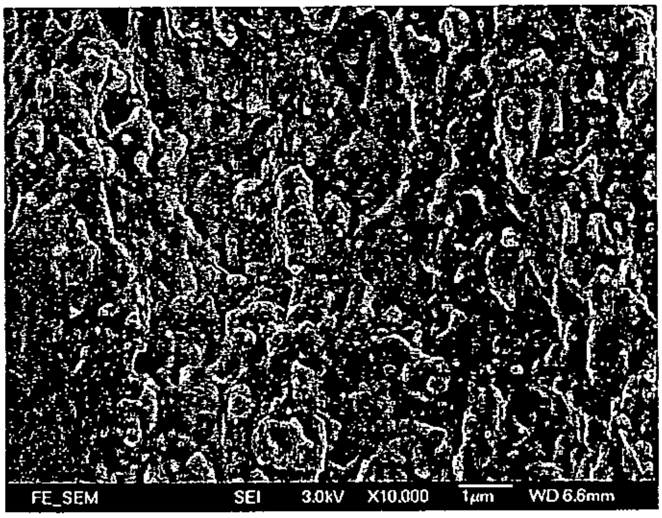

Figure 5.3 SEM cross-sectional micrograph of MMT/P(VDF-TrFE) 0-3 nanocomposite with 4 wt% of MMT.

cross-sectional micrograph of the 4 wt% MMT/P(VDF-TrFE) nanocomposite. It is seen that the MMT particles are dispersed quite uniformly in the copolymer matrix.

The interlayer distance of MMT was determined using an X-ray diffractometer equipped with Ni-filtered Cu-Kα radiation (D8 Advance Bruker analytical XRD). The scanning rate was $2\theta = 0.016°/s$. Figure 5.4 shows the XRD patterns for the P(VDF-TrFE) and MMT/P(VDF-TrFE) nanocomposites with 1 wt% and 4 wt% of MMT. Using Bragg's equation: $n\lambda=2d\sin\theta$ ($\lambda=1.54$ Å), the basal interlayer spacing, $d_{(001)}$ in the Na^+-MMT is found to be 1.22 nm (Figure 5.4 (a)). After the modification, the basal interlayer spacing in the organic MMT is increased to 1.89 nm (Figure 5.4 (b)) due to the presence of CTAB between the layers of MMT. As shown in Figure 5.4 (c and d),

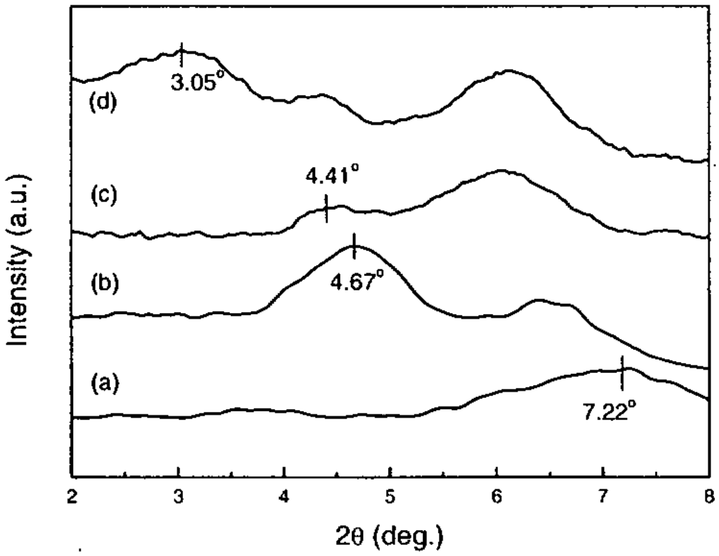

Figure 5.4 XRD patterns for (a) Na^+-MMT, (b) CTAB modified MMT and MMT/P(VDF-TrFE) 0-3 nanocomposites with (c) 1 wt% and (d) 4 wt% of MMT.

the (001) peak shifts to lower angles and the interlayer spacing in the nanocomposites with 1 wt% and 4 wt% of MMT are 2.00 nm and 2.89 nm, respectively. The XRD results indicate that the chains of P(VDF-TrFE) have been partially intercalated into the layered nanostructures of the CTAB modified MMT.

Thermal measurements were performed with a differential scanning calorimeter (Perkin-Elmer DSC7). The heating or cooling rate was 10 °C/min from 0 to 170 °C. Figure 5.5 shows the DSC thermograms for P(VDF-TrFE) and the MMT/P(VDF-TrFE) nanocomposites. The two peaks in Figure 5.5 (I) are associated with the ferroelectric to paraelectric (F–P) phase transition or Curie temperature T_c and the melting temperature T_m of P(VDF-TrFE). During the heating process (Figure 5.5 (I)), T_c of P(VDF-TrFE) is about 128.3 °C. T_c of the nanocomposites with 1 wt% and 4 wt% of MMT shift slightly to higher temperatures which are 131.5 °C and 132.4°C, respectively. During the cooling process (Figure 5.5 (II)), a thermal hysteresis is observed and the Curie point for P(VDF-TrFE) is 74.1 °C and the Curie points for the nanocomposites with 1 wt% and 4 wt% of MMT are 80.6 °C and 84.3 °C, respectively. The other peaks in Figure 5.5 (II) are associated with the crystallization process.

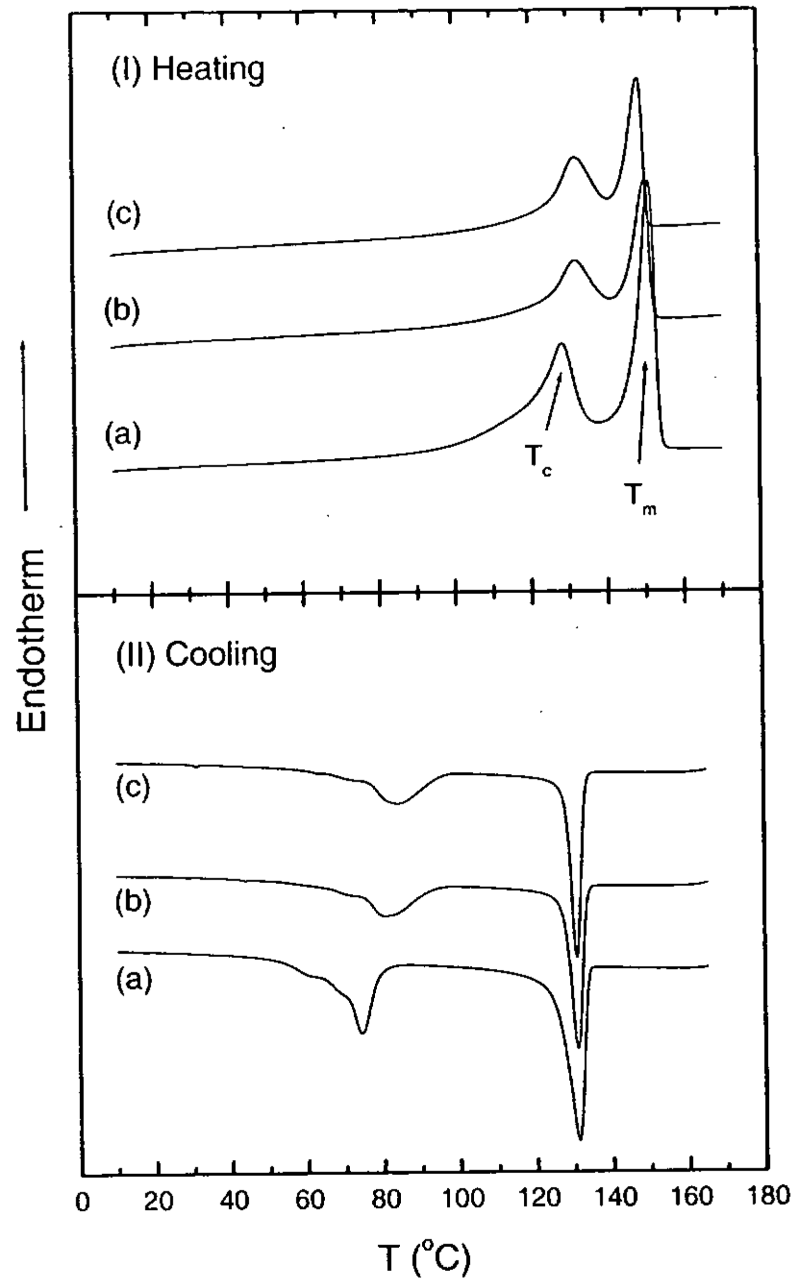

Figure 5.5 DSC thermograms for (a) P(VDF-TrFE) 80/20 mol% and MMT/P(VDF-TrFE) 0-3 nanocomposites with (b) 1 wt% and (c) 4 wt% of MMT during (I) heating and (II) cooling process.

5.4 Dielectric, Piezoelectric and Pyroelectric Properties of MMT/P(VDF-TrFE) 0-3 Nanocomposites

5.4.1 Experimental Techniques

The relative permittivity $\varepsilon_r^{'}$ and dielectric loss $tan\delta$ as a function of frequency from 1 kHz to 10 MHz were measured at room temperature (about 22°C) using an impedance analyzer (HP4294A). The relative permittivity $\varepsilon_r^{'}$ and dielectric loss $tan\delta$ as a function of temperature from 26 °C to 130 °C at 1 kHz were also determined using an impedance analyzer (HP4194A) equipped with a temperature chamber (Delta 9023). The a.c. conductivity and d.c. conductivity as a function of temperature were investigated using an impedance analyzer (HP4194A) and a modified thermal electric analyzer [Peng et al., 1998], respectively.

The polarization hysteresis loops were acquired via a computer-controlled automatic system based on a modified Sawyer–Tower circuit. A sinusoidal wave with a frequency of 10 Hz was used. After the a.c. poling, the piezoelectric coefficient d_{33} of the nanocomposites was measured using a piezo d_{33} meter (Model ZJ-3D, Institute of Acoustics Academia Sinica). The pyroelectric coefficient was also measured via a dynamic method (as described in Section 4.5.2).

5.4.2 Results and Discussion

Figure 5.6 shows the relative permittivity ε_r' and dielectric loss *tanδ* against frequency measured at room temperature for P(VDF-TrFE) and MMT/P(VDF-TrFE) nanocomposites with 1 wt% and 4 wt% of MMT. The relative permittivity ε_r' of the nanocomposites is higher than that of the copolymer at all frequencies. The dielectric loss *tanδ* of the nanocomposites is similar to that of the copolymer at high frequencies but is much higher than that of the copolymer near 1 kHz. The high loss at low frequency may arise from a conduction process.

Figure 5.7 shows the relative permittivity ε_r' and dielectric loss *tanδ* against temperature measured at 1 kHz for P(VDF-TrFE) and MMT/P(VDF-TrFE) nanocomposites with 1 wt% and 4 wt% of MMT. The relative permittivity ε_r' and dielectric loss *tanδ* of the nanocomposites are higher than those of the copolymer, particularly at high temperature.

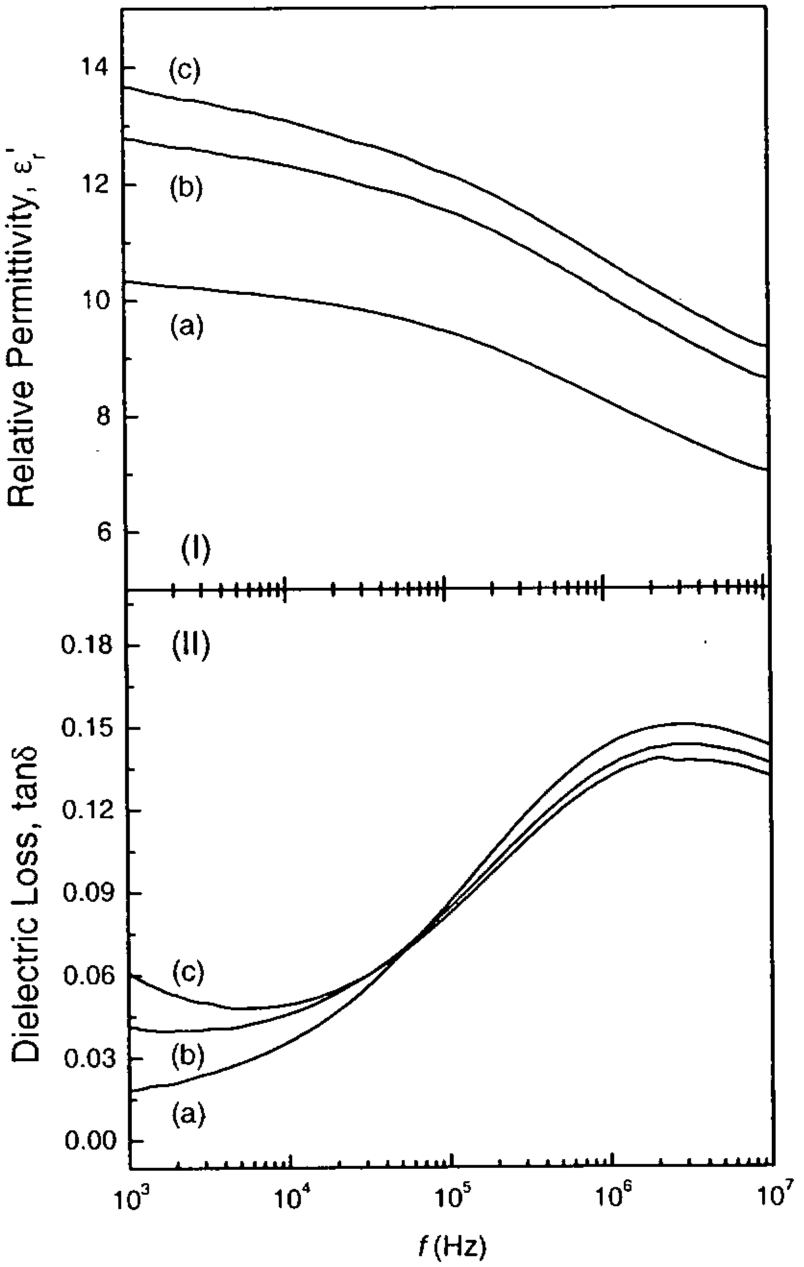

Figure 5.6 Relative permittivity (I) and dielectric loss factor (II) as a function of frequency for (a) P(VDF-TrFE) and MMT/P(VDF-TrFE) 0-3 nanocomposites with (b) 1 wt% and (c) 4 wt% of MMT measured at room temperature.

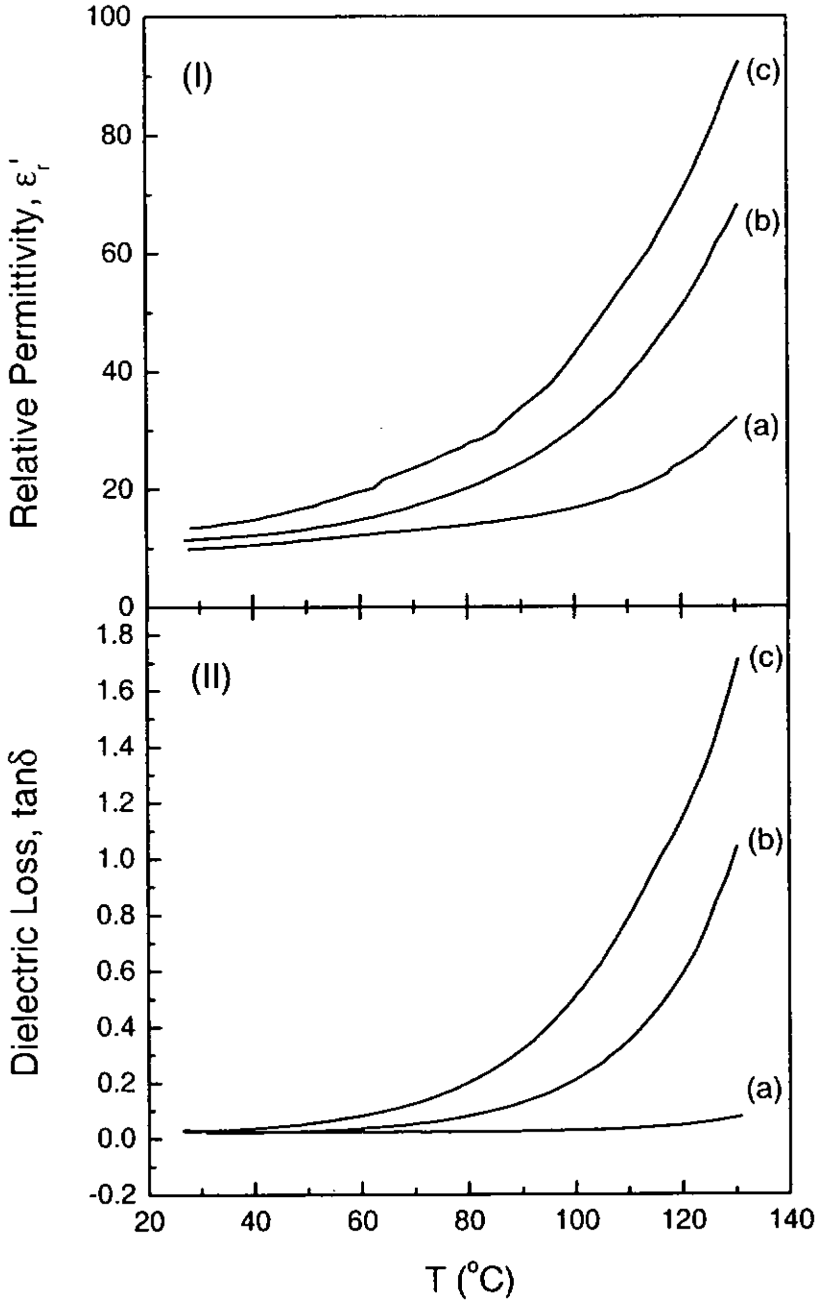

Figure 5.7 Relative permittivity (I) and dielectric loss factor (II) as a function of temperature for (a) P(VDF-TrFE) and MMT/P(VDF-TrFE) 0-3 nanocomposites with (b) 1 wt% and (c) 4 wt% of MMT measured at 1 kHz.

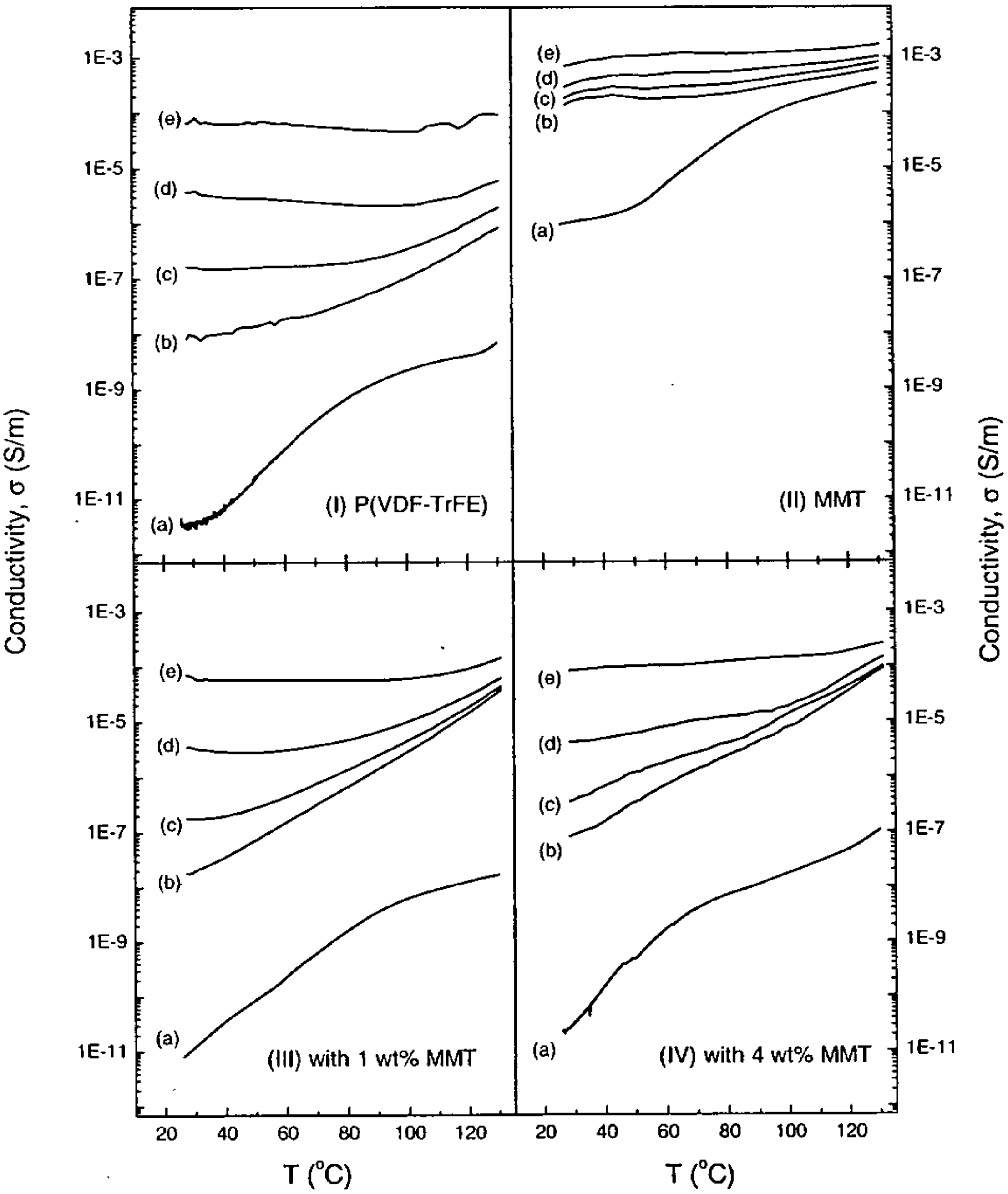

Figure 5.8 Temperature dependence of the conductivity for (I) P(VDF-TrFE), (II) MMT and MMT/P(VDF-TrFE) 0-3 nanocomposites with (III) 1 wt% and (IV) 4 wt% of MMT measured at different frequencies: (a) d.c., (b) 1 kHz, (c) 10 kHz, (d) 100 kHz and (e) 1 MHz.

The conductivities for P(VDF-TrFE), the nanocomposites and a MMT block sample (prepared by compression moulding) were also investigated. As shown in Figure 5.8, the conductivity for all the samples is strongly dependent on the measurement frequency and increases with frequency. The curves for the d.c. conductivity are shown in Figure 5.9. It is seen that the MMT block sample exhibits a very high conductivity compared to P(VDF-TrFE), therefore the conductivity is enhanced significantly with the incorporation of MMT in the nanocomposites.

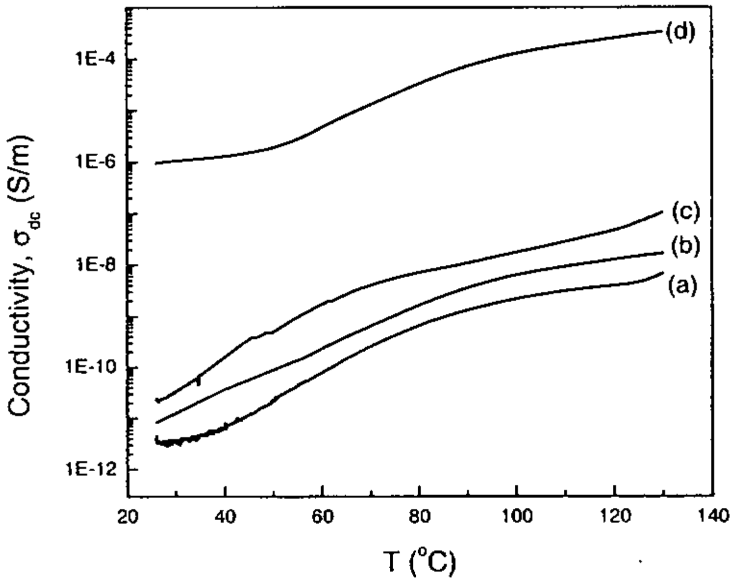

Figure 5.9 Temperature dependence of the d.c. conductivity for (a) P(VDF-TrFE), MMT/P(VDF-TrFE) 0-3 nanocomposites with (b) 1 wt% and (c) 4 wt% of MMT, and (d) MMT.

The polarization hysteresis loops for P(VDF-TrFE) and MMT/P(VDF-TrFE) nanocomposites with 1 wt% and 4 wt% of MMT are shown in Figure 5.10. For the pure copolymer, the values for the remnant polarization P_r and coercive field E_c are about 6.8 μC/cm^2 and 60 V/μm, respectively. The P_r values of the nanocomposites with 1 wt% and 4 wt% MMT are found to be 9.3 and 11.4 μC/cm^2, respectively. The copolymer and the composites have similar E_c values. The result indicates that there are more switchable dipoles in the nanocomposites leading to a higher P_r.

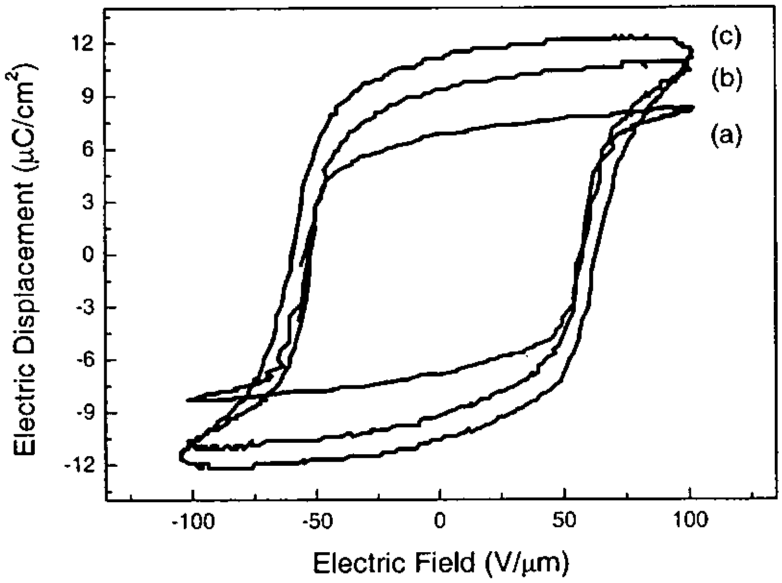

Figure 5.10 Hysteresis loops for (a) P(VDF-TrFE) and MMT/P(VDF-TrFE) 0-3 nanocomposites with (b) 1 wt% and (c) 4 wt% of MMT measured at room temperature.

After being poled by the same a.c. poling process as shown in Figure 5.10, the piezoelectric coefficients d_{33} of P(VDF-TrFE) and the nanocomposites with 1 wt% and 4 wt% of MMT are found to be about 18, 22 and 24 pC/N, respectively, which show that the piezoelectric properties of the nanocomposites are slightly better than that of P(VDF-TrFE).

Figure 5.11 shows the pyroelectric coefficient p against temperature for P(VDF-TrFE) and MMT/P(VDF-TrFE) nanocomposites with 1 wt% and 4 wt% of MMT. The pyroelectric coefficients for nanocomposites are significantly enhanced, especially for

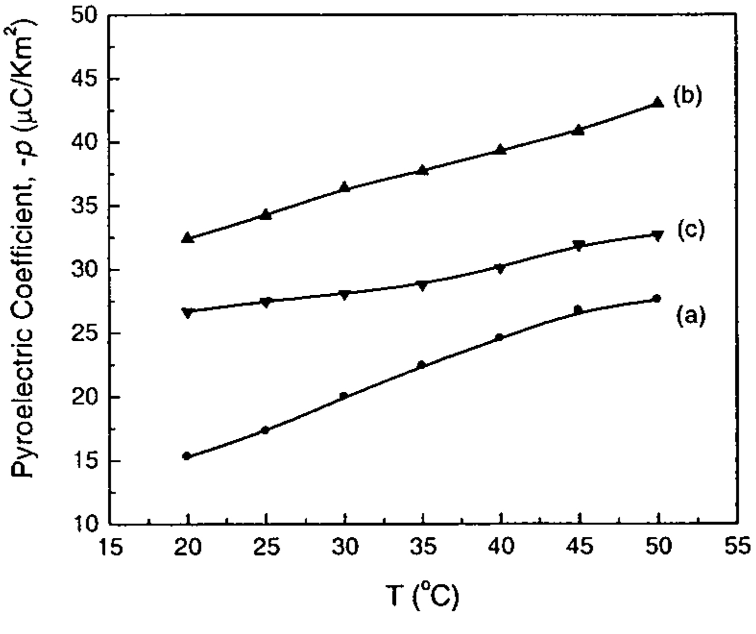

Figure 5.11 Pyroelectric coefficient as a function of temperature for (a) P(VDF-TrFE) and MMT/P(VDF-TrFE) 0-3 nanocomposites with (b) 1 wt% and (c) 4 wt% of MMT.

the nanocomposite with 1 wt% of MMT. However, the data for the nanocomposite with 4 wt% of MMT may not be reliable since a large leakage current is observed. The high pyroelectric coefficient in the nanocomposite with 1 wt% of MMT may be due to the significant amount of charges trapped at the interfaces between the copolymer and the silicate layers. Table 5.1 summarizes the properties of MMT/P(VDF-TrFE) nanocomposites.

Table 5.1 Properties of P(VDF-TrFE) and MMT/P(VDF-TrFE) 0-3 nanocomposites with 1 wt% and 4 wt% of MMT at room temperature.

Materials	*P(VDF-TrFE)*	*1wt% MMT/ P(VDF-TrFE)*	*4wt% MMT/ P(VDF-TrFE)*
ε_r' *(1 kHz)*	10.4	12.7	13.9
$\tan\delta$ *(1 kHz)*	0.02	0.04	0.06
σ_{dc} *(10^{-12}S/m)*	4.6	8.3	24.6
d_{33} *(pC/N)*	18	22	24
P_r *(μC/cm^2)*	6.8	9.3	11.4
-p (μC/m^{2}K)	15.3	32.4	26.7
p/ε (μC/m^{2}K)	1.47	2.55	1.92

5.5 Summary

In this chapter, MMT/P(VDF-TrFE) 0-3 nanocomposites were fabricated via a polymer intercalation approach. The nanocomposites were characterized by XRD and DSC. The dielectric, piezoelectric and pyroelectric properties of the nanocomposites were also investigated. The XRD patterns indicated that the chains of P(VDF-TrFE) had been intercalated into the layered nanostructures of MMT. The DSC thermograms showed that the Curie point of the nanocomposites shifted to higher temperature. The relative permittivity ε_r' increased in the nanocomposites when compared with the pure copolymer. The conductivity σ also increased significantly in the nanocomposites due to the high conductivity of MMT. The remnant polarization P_r of the nanocomposites also increased with increasing amount of MMT. The pyroelectric coefficients p of the nanocomposites was significantly higher than that of the copolymer.

Chapter 6

Conclusions and Suggestions for Future Work

6.1 TGS/P(VDF-TrFE) 0-3 Composites

In this thesis, TGS/P(VDF-TrFE) 70/30 mol% 0-3 composites with various volume percents of TGS ϕ have been fabricated by a hot compression moulding method. In the composite, the medium grain size of TGS is about 5.7 μm and the approximate thickness of the composite film is 70 μm. After the synthesis, the structural properties of the 0-3 composites have been investigated by SEM, XRD and DSC. SEM micrographs for the cross-sectional surface of the composites show a uniform dispersion of TGS particles in the copolymer matrix. The X-ray reflection peaks of both TGS and P(VDF-TrFE) appear in the XRD patterns for the composites. The intensity of the reflections associated with TGS increases while the intensity of the reflection associated with P(VDF-TrFE) decreases with increasing ϕ. In the DSC thermograms for the composites, the phase transition for TGS at 49°C and that for P(VDF-TrFE) at about 101°C (during heating) and 60°C (during cooling) appear and the intensity of the endothermic/exothermic peaks also changes with the change of ϕ.

After a two-step d.c. poling process which is designed to polarize the individual phases separately three series of samples are obtained: unpoled composites (I), composites with only the TGS phase poled (II) and composites with both two phases poled (III).

Dielectric, piezoelectric and pyroelectric properties of these samples have been investigated. The dielectric permittivity ($\varepsilon_r^{'}$ and *tanδ*) as a function of temperature for Series I shows that the phase transitions for the TGS and P(VDF-TrFE) phases also appear in the composites. The dependence of $\varepsilon_r^{'}$ on ϕ agrees quite well with the Bruggeman model. Piezoelectric and pyroelectric properties for Series II and III have been investigated. The experimental data show that the pyroelectric contributions from the two phases reinforce while the piezoelectric contributions partially cancel each other after they have been polarized in the same direction. The measured pyroelectric coefficients exhibit good agreement with the predictions of the effective-medium model.

Table 6.1 Comparisons of two different 0-3 composites.

0-3 Composites	*$PbTiO_3$/ P(VDF-TrFE)*	*TGS/ P(VDF-TrFE)*
ϕ	0.41	0.429
$\varepsilon_r^{'}$	31.1	12.27
tanδ	0.0149	0.008
$-p$ ($\mu C/m^2K$)	51.5	102
$C_p^{vol.}$ ($MJ/m^3 \cdot K$)	2.28	2.14
$F_p=p/\varepsilon$ ($\mu C/m^2K$)	1.66	8.31
F_i($10^{-12}m/V$)	22.6	47.7
F_V(m^2/C)	0.082	0.44
F_D($10^{-6}Pa^{-1/2}$)	11.2	50.0
d_{33}(pC/N)	10	-0.5
Reference	(Chen et al., 1998)	---

In Table 6.1, the previously reported properties of a 0-3 composite are compared with those of the TGS/P(VDF-TrFE) 0-3 composite with 42.9 vol% of TGS. It is seen that the TGS/P(VDF-TrFE) 0-3 composite has higher pyroelectric coefficient and figures of merit. The advantages of the TGS/P(VDF-TrFE) 0-3 composite as the sensing element of pyroelectric infrared detector are as follows:

(1) It is easier to orient the polarization of the inclusion phase since the relative permittivities of the two phases in the composite have similar values;

(2) The pyroelectric coefficient of a 0-3 composite is strongly dependent on the relative permittivity of the inclusion (as discussed in Section 1.4), thus the pyroelectric coefficient of the composite is enhanced because the inclusion phase has a low relative permittivity;

(3) The piezoelectric contributions from the two phases partially cancel each other while the pyroelectric contributions reinforce, thus the composite has high pyroelectric but low piezoelectric activities, thereby reducing the vibration induced electrical noise.

It can be concluded that TGS/P(VDF-TrFE) 0-3 composite with 42.9 vol% of TGS is a good candidate to be used as sensing element for pyroelectric devices. For integrated pyroelectric sensor applications, pyroelectric materials in thin film form are necessary. Thus it will be important to find ways to produce uniform composite thin films and to evaluate their potential use in pyroelectric sensors.

6.2 MMT/P(VDF-TrFE) 0-3 Nanocomposites

In this project, MMT/P(VDF-TrFE) 80/20 mol% 0-3 nanocomposites with 1 wt% and 4 wt% of MMT have also been fabricated via a polymer intercalation approach. The XRD patterns of the nanocomposites indicate that the chains of P(VDF-TrFE) have been intercalated into the layered nanostructures of MMT. The DSC thermograms show that the Curie point of the P(VDF-TrFE) phase in the nanocomposites shifts to higher temperature. The relative permittivity of the nanocomposites is higher than that of the copolymer. Because MMT possesses a high electrical conductivity, the conductivity of the nanocomposites increases significantly with increasing MMT content. The nanocomposite has a higher remanent polarization and higher pyroelectric coefficient than those of the copolymer. The nanocomposite with 1 wt% of MMT has potential to be used as the sensing element in pyroelectric devices. We have studied the structure of the nanocomposites only by XRD. Further studies by TEM will provide more information on the size and spatial distribution of the silicate layers in the nanocomposites.

References

Amin M., Balloonal L. S., Darwish K. A., Osman H. and Kamal B., "Pyroelectricity in rubber composites films", Ferroelectrics, Vol. 81, pp. 381 (1988).

Bhalla A. S., Newnham R. E., Cross L. E. and Schulze W. A., "Pyroelectric PZT-polymer composites", Ferroelectrics, Vol. 33, pp. 139 (1981).

Bruggeman D. A. G., "Berechnung verschiedener physikalischer konstanten von heterogenen substanzen", Ann. Phys. Lpz., Vol. 24, pp. 635 (1935).

Byer R. L. and Roundy C. B., "Pyroelectric coefficient direct measurement technique and application to a NSEC response time detector", Ferroelectrics, Vol. 3, pp. 333 (1972).

Chan H. L. W., Ng P. K. L. and Choy C. L., "Permittivity and electrical conductivity of PZT/P(VDF-TrFE) 0-3 composites", Ferroelectrics, Vol. 201, pp. 225 (1997).

Chan H. L. W., Chan W. K., Zhang Y. and Choy C. L., "Pyroelectric and piezoelectric properties of lead titanate/polyvinylidene fluoride-trifluoroethylene 0-3 composites", IEEE Transaction on Dielectric and Electrical Insulation, Vol. 5, pp. 505 (1998).

Chan H. L. W., Ng P. K. L. and Choy C. L., “Effect of poling procedure on the properties of lead zirconate titanate/vinylidene fluoride-trifluoroethylene composites”, Applied Physics Letters, Vol. 74, pp. 3029 (1999).

Chen G. M., Li Q., Qi Z. N. and Wang F. S., “Advanced in polymer layered silicate nanocomposites”, Polymer Bulletin, Vol. 4, pp. 1 (1999).

Chen Y., Chan H. L. W. and Choy C. L., “Nanocrystalline lead titanate and lead titanate/vinylidene fluoride-trifluoroethylene 0-3 nanocomposites”, Journal of American Ceramic Society, Vol. 81, pp. 1231 (1998).

Chew K. -H., Shin F. G., Ploss B., Chan H. L. W. and Choy C. L., “Primary and secondary pyroelectric effects of ferroelectric 0-3 composites”, Journal of Applied Physics, Vol. 94, pp. 1134 (2003).

Chynoweth A. G., “Pyroelectricity, internal domains, and interface charges in triglycine sulfate” Physical Review, Vol. 117, pp.1235 (1960).

Davis R. D., Gilman J. W. and Vanderhart D. L., “Processing degradation of polyamide 6/montmorillonite clay nanocomposites and clay organic modifier”, Polymer Degradation and Stability, Vol. 79, pp. 111 (2003).

Dias C., Simon M., Quad R. and Das-Gupta D. K., “Measurement of the pyroelectric coefficient in composites using a temperature-modulated excitation", Journal of Physics D: Applied Physics, Vol. 26, pp. 106 (1992).

Dias C. J., Das-Gupta D. K., Hinton Y. and Shuford R., "Polymer/ceramic composites for piezoelectric sensors", Sensors and Actuators A, Vol. 37-38, pp. 343 (1993).

Dias C. J. and Das-Gupta D. K., "Piezo- and pyroelectricity in ferroelectric ceramic-polymer composites", Key Engineering Materials, Vol. 92-93, pp. 217 (1994).

Dias C. and Das-Gupta D. K., "Inorganic ceramic/polymer ferroelectric composite electrets", IEEE Transactions on Dielectrics and Electrical Insulation, Vol. 3, pp. 706 (1996).

Dias C. J., Inacio P., Marat-Mendes J. N. and Das-Gupta D. K., "Polarization and hysteresis in low resistivity ferroelectric composites", Ferroelectrics, Vol. 198, pp. 121 (1997).

Domanski, S., Proc. Phys. Soc. (London) Vol. B72, pp. 306 (1958).

Fang C., Wang M. and Zhou H., "Pyroelectric properties of a new composite material PVDF-TGS film", 7th International Symposium on Electrets, Berlin, IEEE Dielectric and Electrical Insulation Society, pp. 507 (1991).

Furukawa T. and Johnson G. E., “Dielectric relaxations in a copolymer of vinylidene fluoride and trifluoroethylene”, Journal of Applied Physics, Vol. 52, pp. 940 (1981).

Furukawa T., Ohuchi M., Chiba A. and Date M., “Dielectric relaxation and molecular motion in homopolymers and copolymers of vinylidene fluoride and trifluoroethylene”, Macromolecules, Vol. 17, pp. 1384 (1984).

Furukawa T., “Ferroelectric properties of vinylidene fluoride copolymers”, Phase Transition, Vol. 18, pp. 143 (1989).

Garn L. E. and Sharp E. J., “Use of low-frequency sinusoidal temperature waves to separate pyroelectric currents from nonpyroelectric currents. Part I. Theory”, Journal of Applied Physics, Vol. 53, pp. 8974 (1982).

Giannelis E. P., “Polymer layered silicate nanocomposites”, Advanced Materials, Vol. 8, pp. 29 (1996).

Glass A. M., “Investigation of the electrical properties of $Sr_{1-x}Ba_xNb_2O_6$ with special reference to pyroelectric detection”, Journal of Applied Physics, Vol. 40, pp. 4699 (1969).

Hartley N. P., Squire P. T. and Putley E. H., “A new method of measuring pyroelectric coefficients", Journal of Physics E: Scientific Instruments, Vol. 5, pp. 787 (1972).

Higashihata Y., Sako J. and Yagi T., "Piezoelectricity of vinylidene fluoride-trifluoroethylene copolymers", Ferroelectrics, Vol. 32, pp. 85 (1981).

Hippel A. V., *Dielectrics and Waves*, Wiley, New York, (1959).

Hoshino S., Okaya Y. and Pepinsky R., "Crystal structure of the ferroelectric phase of (Glycine)$_3$·H_2SO_4", Physical Review, Vol. 115, pp.323 (1959).

Kawai H., "The piezoelectricity of polyvinylidene fluoride", Japanese Journal of Applied Physics, Vol. 8, pp. 975 (1969).

Kim J. W., Liu F., Choi H. J., Hong S. H. and Joo J., "Intercalated polypyrrole/Na^+-montmorillonite nanocomposite via an inverted emulsion pathway method", Polymer, Vol. 44, pp. 289 (2003).

Krishnamoorti R., Vaia R. A. and Giannelis E. P., "Structure and Dynamics of Polymer-Layered Silicate Nanocomposites", Chemistry of Materials, Vol. 8, pp. 1728 (1996).

Krug W. P., "Orientation on piezoelectric tartaric acid composites", Japanese Journal of Applied Physics Supplement, Vol. 24-2, pp. 871 (1985).

Lando J. B. and Doll W. W., "The polymorphism of polyvinylidene fluoride I. The effect of heat-to-heat structure", Journal of Macromolecular Science: Physics, Vol. B2, pp. 205 (1968).

Levin V. M. and Luchaninov A. G., "On the effective properties of thermo-piezoelectric matrix composites", Journal of Physics D: Applied Physics, Vol. 34, pp. 3058 (2001).

Li J., Zhou C. X. and Gang W., "Study on nonisothermal crystallization of maleic anhydride grafted polypropylene/montmorillonite nanocomposite", Polymer Tesing, Vol. 22, pp. 217 (2003).

Lines M. E. and Glass A. M., *Principles and Applications of Ferroelectrics and Related Phenomena*, Carendon Press, Oxford (1977).

Lovinger A. J., Davis G. T., Furukawa T. and Broadhurst M. G., "Crystalline forms in a copolymer if vinylidene fluoride and trifluoroethylene", Macromolecules, Vol. 15, pp. 323 (1982).

Lu J. and Zhao X. P., "Electrorheological properties of a polyaniline-montmorillonite clay nanocomposite suspension", Journal of Materials Communication Chemistry, Vol.12, pp. 2603 (2002).

Matthias B. T., Miller C. E. and Remeika J. P., "Ferroelectricity of glycine sulfate", Physical Review, Vol. 104, pp. 849 (1956).

Mazur K., "Dielectric, electret, piezo-, and pyroelectric properties of $BaTiO_3$/PMMA and PZT/PMMA composites (Part I and II)", Z. N. Nr 106, Zielona Gora, Poland, Fiz.-Chem., Vol. 6-7, pp.5 (1994).

Mazur K., "Polymer-ferroelectric ceramic composites", Nalwa H. S. eds, *Ferroelectric Polymers: Chemistry, Physics and Applications*, Marcell Dekker Publishers, New York, pp.539 (1995).

Messersmith P. B. and Giannelis E. P., "Synthesis and barrier properties of poly(epsilon-caprolactone)-layered silicate nanocomposites", Journal of Polymer Science Part A: Polymer Chemistry, Vol. 33, pp. 1047 (1995).

Moulson A. J. and Herbert J. M., "Pyroelectric Materials", Moulson A. J. and Herbert J. M. eds., *Electroceramics: Materials, Properties, Applications*, John Wiley & Sons press, Chichester and New York, pp. 420 (2003).

Moussaif N. and Groeninckx G., "Nanocomposites based on layered silicate and miscible PVDF/PMMA blends: melt preparation, nanophase morphology and rheological behaviour", Polymer, Vol. 44, pp. 7899 (2003).

Newnham R. E., Skinner D. P. and Cross L. E., "Connectivity and piezoelectric-pyroelectric composites", Materials Research Bulletin, Vol. 13, pp. 525 (1978).

Peng Z., Liu D, Hu S. H., Zhou Y. Q. and Zhang X. Y., "Development of a control system for TSC apparatus in polymer material study", Computer and Applied Chemistry (in Chinese), Vol. 15, pp. 248 (1998).

Petty M., Tsibouklis J., Holland J., Petty M. C., Feast W. J. and Richards R., "A novel TGS/70/30 VDF-TrFE copolymer composite-material for pyroelectric sensors", Ferroelectrics Letters Section, Vol. 15, pp. 45 (1993).

Ploss B., Ploss B., Shin F. G., Chan H. L. W. and Choy C. L., "Pyroelectric or piezoelectric compensated ferroelectric composites", Applied Physics Letters, Vol. 76, pp. 2776 (2000).

Savakus H. P., Klicker K.A. and Newnham R. E., "PZT-epoxy piezoelectric trasducers: a simplified fabrication process", Materials Research Bulletin, Vol. 16, pp. 677 (1980).

Sawyer C. B. and Tower C. H., "Rochelle salt as a dielectric", Physical Review, Vol. 35, pp. 269 (1930).

Sharp E. J. and Garn L. E., "Use of low-frequency sinusoidal temperature waves to separate pyroelectric currents from nonpyroelectric currents. Part II. Experiment", Journal of Applied Physics, Vol. 53, pp. 8980 (1982).

Skinner D. P., Newnham R. E. and Cross L. E., "Flexible composites transducers", Materials Research Bulletin, Vol. 13, pp. 599 (1978).

Tajitsu Y., Ogura H., Chiba A. and Furukawa T., "Investigation of switching characteristics of vinylidene fluoride/trifluoroethylene copolymers in relation to their structures", Japanese Journal of Applied Physics, Vol. 26, pp. 554 (1987).

Tashiro K., Tadokoro H. and Kobayashi M., "Structure and piezoelectricity of poly(vinylidene fluoride)", Ferroelectrics, Vol. 32, pp. 167 (1981).

Tashiro K., Takano K., Chatani M. and Todokoro H., "Structure study on ferroelectric phase transition of vinylidene fluoride-trifluoroethylene copolymers (III) dependence of transition behavior on VDF molar content", Ferroelectrics, Vol. 57, pp. 297 (1984).

Usuki A., Kojima Y., Kawasumi M., Okada A., Fukushima Y., Kurauchi T. and Kamigaito O., "Synthesis of Nylon 6-Clay Hybrid", Journal of Materials Research, Vol. 8, pp. 1179 (1993).

Vaia R. A., Jandt K. D., Kramer E. J. and Giannelis E. P., "Microstructural Evolution of Merit Intercalated Polymer-Organically Modified Layered Silicates Nanocomposites", Chemistry of Materials, Vol. 8, pp. 2628 (1996).

Vaia R. A. and Giannelis E. P., "Polymer Melt Intercalation in Organically-Modified Layered Silicates: Model Prediction and Experiment", Macromolecules, Vol. 30, pp. 8000 (1997).

Varaprasad A. M. and Uchino K., "Dielectric relaxation studies in some polymer-PZT composites", Ferroelectrics Letters Section, Vol. 7, pp.55 (1987).

Wagner K., "Erklarung der dielektrischen nachwirkungsvorgange auf ground maxwellscher vorstelungen", Archiv. Elektrotech., Vol. 2, pp. 371 (1914).

Wang Y. G., Zhong W. L. and Zhang P. L., "Pyroelectric Properties of Ferroelectric-Polymer Composites", Journal of Applied Physics, Vol. 74, pp.521 (1993).

Xu Y. and MacKenzie J. D., "Ferroelectric and dielectric properties of synthetic rubber and PbTiO3 or PZT", Integrated Ferroelectrics, Vol. 1, pp. 17 (1992).

Xu Y. H., *Ferroelectric Materials and Their Applications*, Elsevier Science Publishers B. V., Amsterdam (1991).

Yagi T., Tatemoto M. and Sako J., "Transition behavior and dielectric-properties in trifluoroethylene and vinylidene fluoride co-polymers", Polymer Journal, Vol. 12, pp. 209 (1980).

Yamada T., Ueda T. and Kitayama T., "Piezoelectricity of a high content lead zirconate titanate/polymer composite", Journal of Applied Physics, Vol. 53, pp. 4328 (1982).

Yamazaki H. and Kitayama T., "Pyroelectric properties of Polymer-Ferroelectric Composites", Ferroelectrics, Vol. 33, pp. 147 (1981).

Yano K., Usuki A., Okada A., Kurauchi T. and Kamigaito O., "Synthesis and properties of polyimide clay hybrid", Journal of Polymer Science Part A: Polymer Chemistry, Vol. 31, pp. 2493 (1993).

Zhang Q. Q., Chan H. L. W. and Choy C. L., "PCLT/P(VDF-TrFE) 0-3 nanocomposite thin films for pyroelectric applications", Materials Research Innovations, Vol. 2, pp. 283 (1999).